



Fermi National Accelerator Laboratory

FERMILAB-TM-2018

**Conceptual Design for the
Technical Components of the Neutrino Beam for the Main Injector
(NuMI)**

J. Hylan, W. Smart, A. Wehmann, S. Menary, A.J. Malensek,
D. Johnson, J. Morfín, G. Koizumi and P. Lucas

*Fermi National Accelerator Laboratory
P.O. Box 500, Batavia, Illinois 60510*

September 1997

FNAL-TM-2018
NuMI-B-285
September 1, 1997

**Conceptual Design
for the
Technical Components
of the
Neutrino Beam for the Main Injector
(NuMI)**

J. Hylan, W. Smart, A. Wehmann, S. Menary, A.J. Malensek,
D. Johnson, J. Morfín, G. Koizumi, P. Lucas

abstract

The design is presented of a beamline which uses 120 GeV protons from the Fermilab Main Injector to produce a neutrino beam which will be used for experiments located on the Fermilab site and 730 km away at the Soudan Mine in Minnesota. Section 1 of this document presents a relatively non-technical overview of the entire project. Section 2 describes the experimental constraints and goals which guide the beamline design. Section 3 presents the technical details of the design.

Contents

1	The Neutrino Program	5
1.1	Introduction	5
1.2	Overview of the Neutrino Beamline	6
1.2.1	Extraction	7
1.2.2	Transport of the Primary Protons	7
1.2.3	Production Target	8
1.2.4	Gathering and Focusing of Secondary π 's and K's from the Target	8
1.2.5	Decay Pipe	9
1.2.6	Hadron Absorber	9
1.2.7	Muon Shield	10
1.2.8	Monitoring and Calibrating the NuMI Beam	10
2	Physics of the Neutrino Beam	13
2.1	Matching the Main Injector	13
2.2	Matching Experimental Goals	18
3	Technical Requirements	23
3.1	Extraction and Primary Beam Transport	23
3.2	Target	35
3.3	Focusing System - Wide Band Beam	41
3.3.1	Horn Focusing	41
3.3.2	Neutrino Rates	48
3.3.3	Alignment Requirements	56
3.3.4	Hadron Production Model Uncertainty	63
3.3.5	Hadronic Hose Option	64
3.3.6	Horn Mechanical Design	70

3.3.7	Horn Electrical Design	73
3.4	Decay Pipe	76
3.5	Hadron Absorber	81
3.6	Beam Monitoring using Muons	82
3.7	Muon Absorber	88
3.8	Radiation Concerns	89
3.8.1	Prompt radiation, neutrons and muons	89
3.8.2	Activation of Components	90
3.8.3	Air Activation	90
3.8.4	Groundwater Activation	90
A	Coordinates of Beamline Elements for the Wide-Band Beam Primary Transport.	100
B	Neutrino Beam Design Monte Carlo Programs	102

Chapter 1

The Neutrino Program

This document describes plans for building a beamline which uses 120 GeV protons from the Fermilab Main Injector (MI) to produce a neutrino beam which will be directed towards detectors located on the Fermilab site and 730 km away in a mine in Soudan, Minnesota. A brief history of events leading up to this document can be found in Fermilab-TM-1946[1], which also contains a compendium of previous documents.

1.1 Introduction

Neutrinos are uncharged particles which interact relatively seldom. For instance, for each person on Earth there are several hundred billion neutrinos from the sun coarsing through every square inch of their bodies every second. Neutrinos come in three “flavors” (types) labeled ν_e , ν_μ , and ν_τ . There is also a corresponding set of three anti-neutrinos. The physics program for which this beam is designed is a systematic search for a phenomenon that is only subtly suggested by other experiments. If this phenomenon does exist, then a certain fraction of the neutrinos that start off as one flavor (for example ν_μ) change - oscillate - into another flavor (such as ν_τ or ν_e) before interacting in a detector. If we combine the fact, mentioned above, that neutrinos in general interact very rarely, with the possibility that only a very small fraction of these neutrinos will display this oscillation phenomenon, then to accumulate a significant data sample experimenters need both very massive detectors and a carefully designed and implemented beamline yielding an intense flux of neutrinos.

The probability that a neutrino interacts is directly proportional to the energy of the neutrino, so experimenters would normally want the highest possible energy beam for their experiments. In the case of neutrinos which oscillate from

one flavor to another, the pursued effect is a function of the neutrino energy, the neutrino flavor, and the distance between neutrino production and detection points. It is therefore necessary to understand to an unprecedented degree both the energy distribution of the neutrinos in the beam as well as the initial mixture of neutrino flavors. It is also desirable to have a mode of neutrino running where the energy of the beam can be selected.

The physics program as now envisioned initially calls for a beam of neutrinos with a broad range of energies, known as a Wide Band Beam (WBB). This WBB would serve two experiments, each of which would examine an aspect of neutrino oscillations suggested by other experiments. The first experiment, the so-called “short baseline” experiment COSMOS, would have a detector located about 1 km from the start of the neutrino beam and would search for neutrino oscillations hinted at by cosmological observations. The second, the “long baseline” experiment MINOS, utilizes two detectors; a “near” detector about 1.3 km away from the target and a “far” detector located 730 km away in the Soudan mine in Minnesota. This long baseline would allow MINOS to study more complicated oscillation scenarios. If neutrino oscillations are found, then it may be desirable after a few years running to modify the beamline to produce a beam with a narrow range of neutrino energies (a Narrow Band Beam or NBB). Design work on the NBB is continuing, but is not described in this document. The beamline can also be used to produce an antineutrino beam which could be used to study \mathcal{CP} Violation in the lepton sector (complementary to the quark sector \mathcal{CP} Violation studies being performed at the so-called “ B Factories”) as well as more conventional neutrino physics topics such as non-perturbative QCD effects, neutrino induced nuclear effects, and the extraction of parton distribution functions.

1.2 Overview of the Neutrino Beamline

The neutrinos transported to the experiments result from the decay of secondary pions and kaons as well as (tertiary) muons. The chain of events which eventually results in a neutrino beam is (see Figure 1.1):

- extraction of protons from the accelerator,
- transport of these protons to a target where kaons and pions are produced,
- gathering and focusing of secondary pions and kaons from the target, and
- the decay of these secondaries to produce neutrinos.

Figure 1.1: Sketch of the NuMI beam line.

1.2.1 Extraction

The protons are extracted from the Main Injector accelerator using standard resonant extraction techniques. A perturbation is induced in the orbit of the protons using a specially designed extraction pulse to the focusing magnets. At a predetermined point of maximum excursion from the nominal orbit, the perturbed protons encounter an electric field which kicks them toward an extraction channel. A specialized magnet which gives a kick to the extracted beam while allowing the unextracted beam to pass through unaffected completes the extraction. In this manner, the entire set of circulating protons is extracted in roughly 100 turns taking of order 1 millisecond (ms).

1.2.2 Transport of the Primary Protons

The extracted protons are focused and bent strongly downward by a string of quadrupoles and bending magnets so that they enter, for construction concerns, the denser dolomite rock formation as soon as possible. Another set of bend magnets brings the protons to the correct pitch for a zero targeting angle (maximum intensity) beam directed toward the experiments. The size and angular dispersion of the proton beam is controlled by a final set of quadrupoles and is matched to the diameter of the production target.

1.2.3 Production Target

Most of the 120 GeV protons interact with nuclei in the target, producing pions and kaons with a broad momentum spectrum. With several 10^{13} protons striking the target every 2 seconds, the target becomes highly radioactive soon after beam start-up. Replacement of a failed target is then an arduous, dangerous, and time-consuming process. The design of the target is therefore a compromise between obtaining maximum yield and ensuring the integrity of the target against mechanical failure due to shock and heat build-up. If the diameter of the target is too large, secondary pions and kaons interact within the target before they can escape out the sides and decay to neutrinos. If the diameter is too small with a consequent small beam image, the shock wave and heat build-up quickly bring on mechanical failure of the target. Similar arguments control the length of the target. If the target is too short, only a small fraction of the protons will interact within the target. If it is too long, many of the forward traveling pions and kaons will interact within the target before having opportunity to decay to neutrinos. A solution is a small diameter, segmented carbon target with space between the segments to allow normal angular dispersion to bring the secondaries out of the radius of the target.

1.2.4 Gathering and Focusing of Secondary π 's and K's from the Target

Secondary particles resulting from proton-nucleus interactions typically are produced with a transverse momentum of ~ 300 MeV/c which translates into a spectrum of production angles. A perfect gathering and focusing system would collect all secondary particles of the required charge and focus them into a precisely parallel, microscopically thin pencil beam. This ideal gathering system is unfortunately not realistically attainable.

The most efficient focusing system which matches NuMI requirements consists of a set of magnetic horns. Each horn consists of two cylindrically symmetric current sheets; a thin walled, cone-shaped, aluminum inner conductor and a thin-walled cylindrical outer conductor with a strong current (roughly 200,000 A) flowing out along the inner element and back along the outer wall. The magnetic field is contained between the inner and outer conductors. The shape of the inner conductor has been studied at various laboratories around the world and is normally either a simple or modified parabola. These magnetic horns are able to focus efficiently even if the particles do not all start from the same point and have been shown to be efficient at gathering particles that originate over about a 1.5 m longitudinal distance upstream of the horn. This allows a

longer production target with a correspondingly increased percentage of interacting protons. In our studies, the maximum yield is obtained when three of these horns, with varying radii and lengths of inner and outer conductors, are incorporated in the beamline. A special electrical system able to deliver 200 kA over a 1 ms pulse has been designed to energize the horns.

1.2.5 Decay Pipe

The decay pipe provides an evacuated space for the secondary π 's and K's to decay.

The decay pipe length is chosen to optimize the neutrino flux in the detectors. The neutrino flux is predominantly from the pions with momentum between 20 GeV/c and 60 GeV/c. The mean decay length of a π with this momentum is 1 to 3 km. The number of neutrinos for the long baseline experiment thus continues to increase significantly with any reasonable decay pipe length. For the short baseline experiment, the detector has to be moved further from the target as the decay pipe is lengthened. Thus flux in the detector from decays from the early part of the pipe goes down as the pipe is lengthened, and the optimum decay pipe length is some hundreds of meters. The current baseline design is a compromise, calling for a decay pipe length of 750 m. Combining this with the 50 m distance from target to start of the decay pipe culminates in a 800 m long decay region for the beamline.

The decision on the width of the decay pipe must balance the loss of secondaries which interact with the walls of the pipe against the cost increases associated with larger radius pipes. In general, for the nominal beam pipe length of 750 m, the gains in neutrino flux are rather dramatic as the radius of the pipe increases to 1 m or so with comparatively modest gains over the next meter increase in radius.

It is important not to isolate the optimization of beam pipe parameters from the rest of the project, which includes the massive experimental detectors. It is reasonable to compare tradeoffs in cost and event rates when the size of both systems, i.e., the beamline and the neutrino detector, is varied.

1.2.6 Hadron Absorber

The experimental detectors are designed to detect the interactions of neutrinos. All other types of particles must be eliminated since their much higher event rate would dominate data taking. All hadrons, including the primary protons which did not interact in the target, are eliminated by a hadron absorber at the end of the decay pipe. This absorber consists of a water-cooled aluminum

and copper central core to dissipate the heat of the hadronic interactions plus a surrounding steel jacket to keep radiation from escaping out of the absorber.

1.2.7 Muon Shield

The hadron absorber cannot eliminate the muon component of the beam which interacts only electromagnetically. Since the short baseline neutrino oscillation experiment uses an emulsion-based detection technique, it is imperative that the muon component of the beam be minimized so as not to darken the emulsion. Muons can be eliminated by active shielding based on large and expensive magnetic devices or by providing sufficient medium to slow them down via multiple electromagnetic interactions. The beamline is being built in dolomite, a dense rock layer. It has been calculated that 240 meters of dolomite between the end of the hadron absorber and the short baseline experiment is sufficient to eliminate muons coming from the decay pipe.

1.2.8 Monitoring and Calibrating the NuMI Beam

The main objective of the NuMI beamline is to provide neutrinos for neutrino oscillation experiments. As mentioned earlier, these experiments demand knowledge of the flavor composition and energy spectrum of the beam considerably beyond what has been required of previous neutrino beams. To accomplish this, the monitoring and calibration of the beamline will have to be a major effort. Monitoring/calibrating can be divided into three main categories of increasing complexity.

1. On a pulse-to-pulse basis we want to be sure that:
 - The proton beam size, angular divergence, targeting angle, and intensity are correct. (Are extraction and pre-target elements functioning correctly?)
 - The ratio of the total number of charged secondaries to protons-on-target is correct at selected distances along the beamline. (Are horns functioning correctly? Is there a problem with the target?)
 - The intensity vs. position of the charged secondaries is correct. (Are horns functioning symmetrically, have they moved?)

The proton beam is monitored with standard devices which sense the electromagnetic wake of the protons. Our main tool monitoring the secondary particles will be the intensity, position, and momentum of the muons originating (mainly) in the decays that produce the neutrinos. The intensity

vs. position of the muons will be measured just after the hadron absorber and at selected longitudinal positions along the dolomite muon shield. The momentum distribution of the muons will be (roughly) determined by their range in the dolomite shielding.

2. On a somewhat more infrequent time scale we must determine:
 - The flavor and relative energy distribution (shape) of the neutrino spectrum entering the near detector(s)

A detector located in the Short Baseline experimental hall will record approximately 10 events/ton/min. The detector must be designed to be able to discriminate between neutrino flavors, to measure the neutrino energy with minimal error, and to provide fully reconstructed events on a time-scale which will allow frequent comparison of the spectra.

3. Once during the course of the experiment we must predict:
 - The expected flavor-dependent, neutrino energy distribution at the far detector under the supposition that neutrinos do not oscillate.

This will be the most important monitoring/calibration task and the most difficult to accomplish. It may well involve an auxillary experiment to determine the mass and momentum of the particles emerging from the target and/or two “beam-spectrometers” located in the COSMOS and MINOS-near halls.

Chapter 2

Physics of the Neutrino Beam

2.1 Matching the Main Injector

The dominant source of ν_μ in the NuMI beam is the decay $\pi^+ \rightarrow \mu^+ \nu_\mu$. Figure 2.1 shows the spectrum of pions produced in the NuMI target by the primary 120 GeV proton beam. One might imagine that the natural neutrino physics scale for NuMI would be a few GeV, since that is where the pion spectrum peaks. However, several factors work to boost that scale significantly higher.

The pion decay kinematics for neutrinos can be approximated by

$$E_\nu = \frac{0.427 E_\pi}{(1 + \gamma^2 \theta^2)}$$
$$Flux = \left(\frac{2\gamma}{1 + \gamma^2 \theta^2} \right)^2 \frac{A}{4\pi r^2}$$

where γ is the Lorentz boost of the pion, θ is the angle between the pion flight direction and the detector, A is the cross-sectional area of the detector, and r is the distance to the detector. The energy and flux of the neutrinos peak along the pion flight direction. Note that for well focused pions and a detector near the axis of the pion beam, θ is approximately 0, resulting in the neutrino energy being approximately 43% of the pion energy, and a Lorentz boost favoring high energy neutrinos in the flux by a factor of γ^2 .

What one actually counts in the detector are interactions, and the neutrino cross-section rises approximately linearly with energy. As an initial yardstick, we will use the ν_μ charged current (CC) interaction cross section.

In an ideal system (“perfect focus”), the pions would be focused directly towards the detector. Applying the above energy, flux, and cross-section relations

to the pion spectrum, one obtains a neutrino event spectrum in the MINOS far detector¹ that is shown in Figure 2.2. The mean energy is 24 GeV.

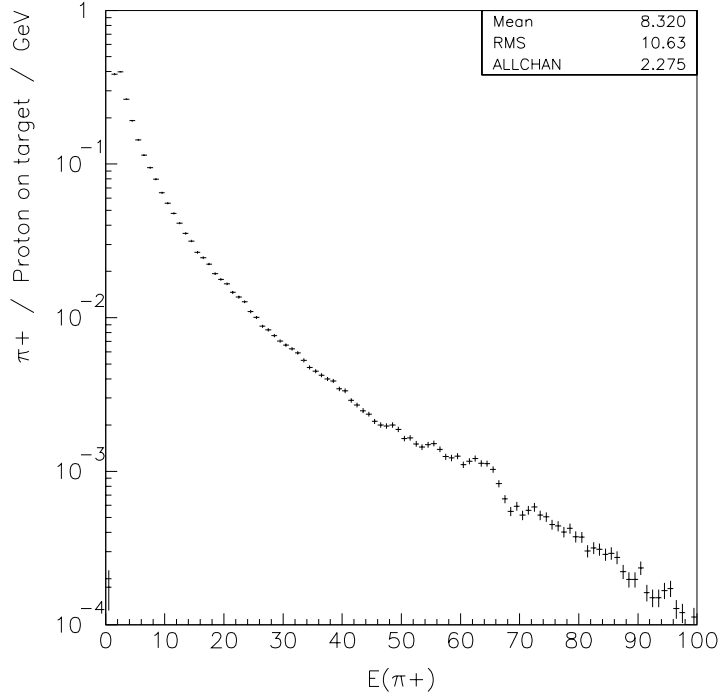


Figure 2.1: The energy spectrum of π^+ from a 2 mm radius 2 interaction length Carbon graphite target according to the **GEANT/FLUKA** Monte Carlo. (The structure around 62 GeV is an artifact of the **GEANT/FLUKA** Monte Carlo generator.)

Several effects then reduce the actual number of events. The finite length of the decay pipe means that a large fraction of the pions do not have time to decay. This is illustrated in Figures 2.3 and 2.2, and the effect is a decrease in the mean energy of available events. Another major effect is absorption of the pions in the elements of the focusing system, which ranges from 20% to 40%. Finally, you can focus some of the pions at all momenta, or all of the pions at some momenta, but not all pions, at all momenta, for all angles from the target. As shown in Figure 2.2, for E_ν between 8 GeV and 25 GeV, the baseline NuMI focusing system manages to deliver 50% to 60% of the events that would be available with perfect focusing and no focusing element absorption in an 800 m long decay region. The choice to set the focusing between 8 GeV and 25 GeV

¹The situation is somewhat more complicated for the near COSMOS detector than outlined in this section, because the beamline does not then look like a point source.

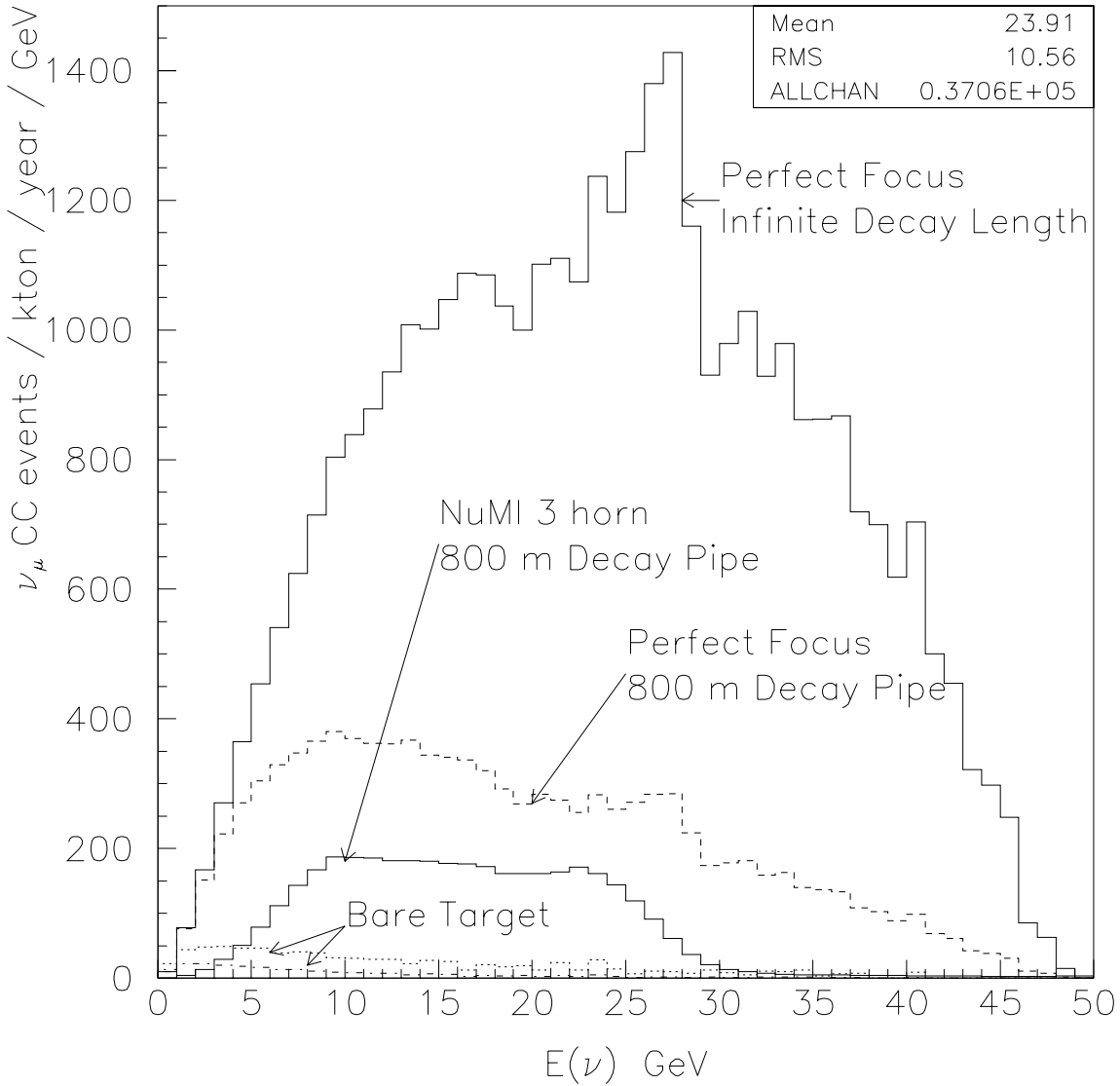


Figure 2.2: The ν_μ charge current interaction rate spectrum at the MINOS far detector using the baseline focusing system, compared to perfect focusing and to no focusing. The upper histogram labeled Bare Target is for an infinite decay pipe, the lower for an 800 m long (but infinite radius) decay region. The bump at 26 GeV is again a reflection of the Monte Carlo pion generator.

is seen as a natural match to the Main Injector proton beam (i.e., maximizing the event rate), although one could adjust the focusing to a somewhat lower or higher energy range.

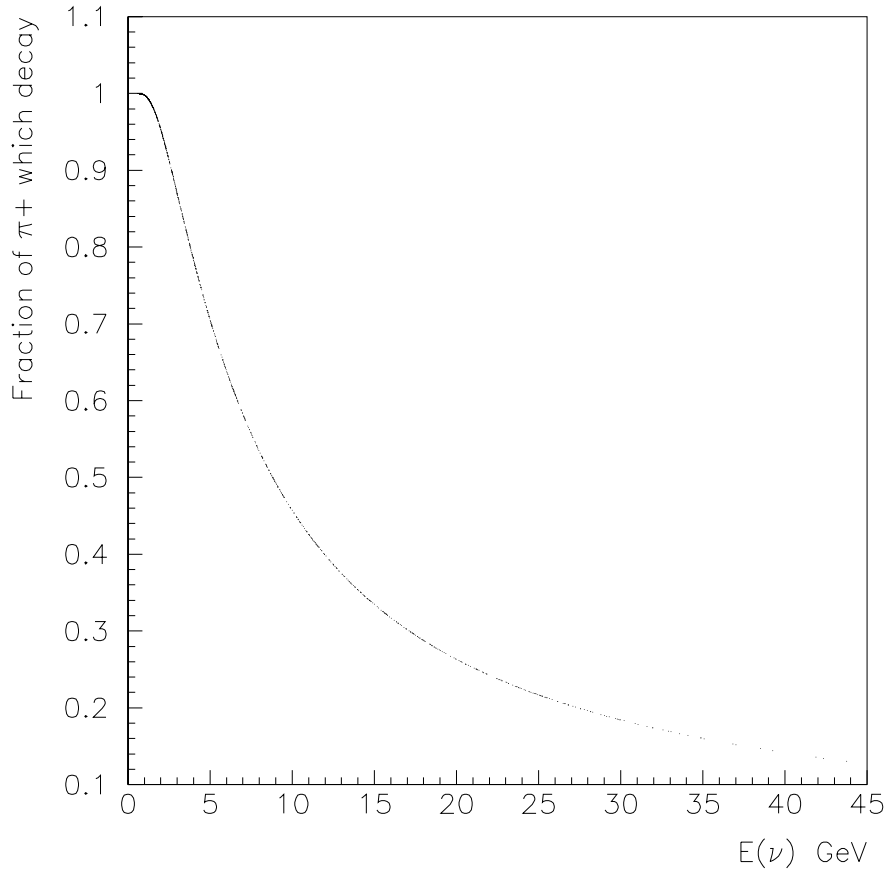


Figure 2.3: The fraction of π^+ which decay in 800 m as a function of the energy of the neutrino produced. (The energy scale is based on the approximation that the neutrino is produced at a negligible angle to the pion direction.)

The rate that could be obtained without a focusing system (so called “bare target”) is also plotted in Figure 2.2, illustrating the substantial gain that is achieved by the focusing system.

The beamline design gives the flexibility to modify the neutrino beam by changing the focusing elements in the target hall after the initial running period. Three examples of achievable and possibly desirable beam modifications are:

- A beam which transmits only a (tunable) narrow part of the energy spec-

trum (a “narrow band beam”).

- A beam of $\bar{\nu}_\mu$ instead of ν_μ .
- A wide band beam which is optimized for lower energy ν_μ . A large factor could be gained in the few GeV range, at the expense of the high energy part of the spectrum.

2.2 Matching Experimental Goals

The beamline design must match the physics goals of the experiments that will use it. This section presents an overview of the input to beam design from the various experimental tests which look for neutrino oscillations. The parameters which characterize neutrino oscillations are δm^2 (the difference in the squares of the masses of two neutrino flavors) and $\sin 2\theta$, where θ is a mixing angle. The frequency of oscillations is related to δm^2 while the amplitude goes like $\sin^2 2\theta$.

MINOS (NC/CC) (Far/Near) For the long baseline experiment, the most robust test is the measurement of the double ratio of neutral current (NC) to charged current (CC) ν_μ events in the far and near detectors. Oscillations cause a deficit of $\nu_\mu \rightarrow \mu$ events in the far detector, as well as an enhancement of events which are neutral-current-like (i.e., don't contain a muon). This experimental test is rate limited even for several years of running, so higher event rate (efficiency of the focusing system) is a high priority.

MINOS CC Total Energy Spectrum Although the (NC/CC)(Far/Near) test is more sensitive to small amounts of oscillation, a fit to the ν_μ CC Total Energy Spectrum has the advantage that it actually measures the values of δm^2 and $\sin^2(2\theta)$. It has the added beauty that one can see the oscillation structure directly in the spectrum. Figure 2.4 shows the change in the far detector spectrum expected for δm^2 in the region of 10^{-2} eV². In order to use the spectral difference to its full statistical power for smaller oscillations, one needs to predict the spectrum at the far detector with a precision of 2–3%. This is the most challenging aspect of the NuMI beam design. The concepts that address this are:

- Moving the MINOS near detector further away from the end of the decay pipe,
- Making precise measurements of the NuMI beam element positions and focusing strengths, in combination with a separate hadron production experiment using the NuMI target to actually measure the π and K flux produced by 120 GeV protons,
- Adding continuous focusing in the decay pipe (the “hadronic hose”) to make the spectra in the near and far detectors more nearly the same.

MINOS CC Far/Near If δm^2 is in the 10^{-3} eV² range, then the Far/Near ratio of charged current events is a more sensitive test than the NC/CC ratio

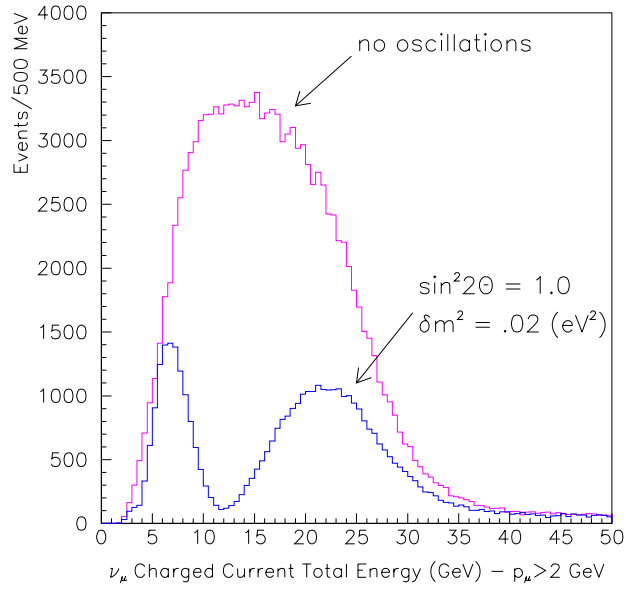
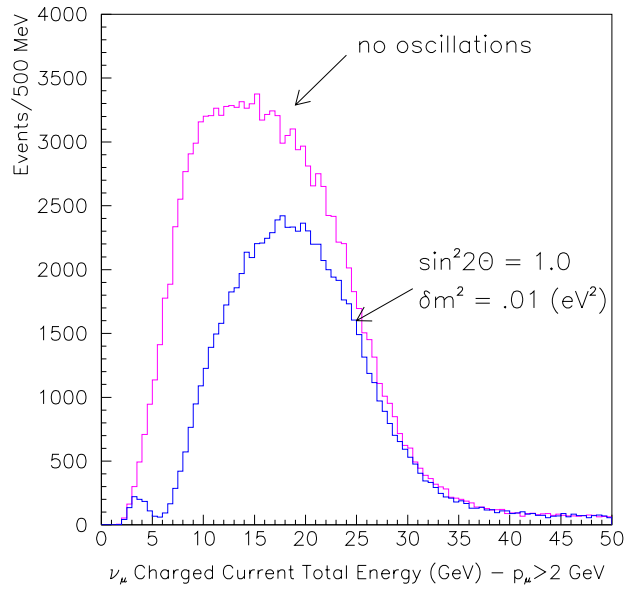


Figure 2.4: Energy spectrum of reconstructed ν_{μ}^{CC} events in the MINOS far detector in the case of no oscillations, and for two possible points in the range indicated by the “atmospheric neutrino anomaly” as observed in underground experiments. The spectra have been smeared by expected detector resolution.

test. The requirements on knowledge of the beam spectrum are similar to the CC Total Energy Spectrum test.

MINOS electron ID Both the $\nu_\mu \rightarrow \nu_e$ and $\nu_\mu \rightarrow \nu_\tau$ oscillation channels give electrons in the detector, and in both cases the inherent ν_e content of the beam is then a background. The NuMI beam naturally has a fairly low ν_e content; ν_e^{CC} interactions happen at about 0.5% of the rate of ν_μ^{CC} interactions. Little can be done to reduce the ν_e 's without a consequent substantial reduction in the ν_μ rate. Statistical fluctuations in the beam ν_e events limit experimental sensitivity to $\nu_\mu \rightarrow \nu_e$ oscillations to around 2×10^{-3} in $\sin^2(2\theta)$.

MINOS τ ID A large fraction of the neutrino spectrum is high enough energy that ν_τ 's from oscillations can produce τ 's in the detector (see Figure 2.5). This

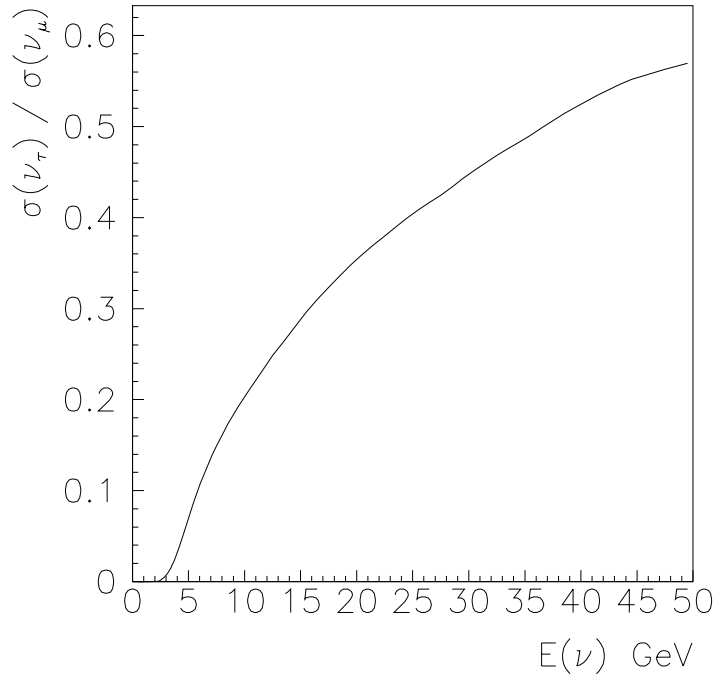


Figure 2.5: The ratio of the ν_τ cross section to the ν_μ cross section as a function of energy.

test has little additional impact on the wide band beam design. There will, however, be a very strong connection between τ identification and the narrow band beam design, because a goal is a beam which contains practically no low energy neutrinos. This requirement arises from the fact that the $\tau \rightarrow \mu$ decays

could be identified by a measurement of the total visible energy in the event which would be lower than the nominal beam energy, due to missing energy carried off by the two neutrinos in the decay chain. An alternative, and more direct way, to detect τ leptons is by the observation of “decay kinks” in an emulsion detector at Soudan. This possibility is under active consideration and, if adopted, would decrease the need for such a clean energy definition.

COSMOS CC τ ID The short baseline experiment will search for explicit τ decay channels to look for $\nu_\mu \rightarrow \nu_\tau$ oscillation. The event rate depends on the ν_τ cross section which is suppressed at the lower neutrino energies, see Figure 2.5. This puts a premium on producing the higher energy part of the spectrum.

Another crucial aspect for the short baseline experiment is keeping beam-related backgrounds low. There are ν_τ from charm decay produced at the target and at the hadron absorber, although at a very low rate. The other beam related background comes from $\bar{\nu}_\mu$. The $\bar{\nu}_\mu$ can produce anti-charm in the detector and, if the muon is missed in the event reconstruction, the event looks like a τ candidate. The system which focuses the π^+ acts naturally to defocus the π^- (which are the major source of $\bar{\nu}_\mu$).

Finally, to avoid pileup of ν events in the detector, the beam spill has to be spread out over approximately 1 ms.

Chapter 3

Technical Requirements

3.1 Extraction and Primary Beam Transport

A description of the NuMI extraction and primary beamline design has previously been presented[2, 1]. The new design presented here reflects the following changes and features:

- The last quadrupole magnet before the target, Q110, has been moved upstream by about 10 meters to make room for added instrumentation and for beam baffles for the protection of the horns from errant beam;
- This lattice has reverted to the use of “recycled” 3Q120 quads;
- Instrumentation and trim magnets have been added to the lattice file;
- The number of vertical bend magnets in the pretarget hall has been increased from four to six to reduce magnet current;

The beamline as outlined is explicitly designed for the production of the Wide Band neutrino beam. However, it has been shown to be compatible with a number of possible implementations of a later Narrow Band Beam.

Resonant Extraction The beam goals for NuMI based on the Main Injector 120 GeV resonant extraction have been stated[1] to be 4×10^{13} protons on target during a 1 ms spill. The assumed cycle time for this 120 GeV ramp is 1.9 sec.

Preliminary modeling for the “fast” resonant extraction from MI-60 utilized the opposite 53^{rd} harmonic quadrupole family from that used in MI-52 resonant extraction to Switchyard. The quad circuits are pulsed in a half-sine wave to produce a spill with a duration of roughly 1 ms (100 turns)[5].

A simulation has been performed[6] assuming an initial normalized emittance at 120 GeV prior to extraction of 30 π -mm-mr in both planes. An ensemble of 1000 particles was tracked through the Main Injector during extraction. The momentum spread ($\Delta p/p$) is expected to be on the order of $\pm 0.04\%$ (assuming an RF voltage of 400 kV and a longitudinal emittance of .25 eV-sec), but for this exercise was assumed to be zero.

The septa wires were assumed to be 16 mm to the inside of the Main Injector centerline. The closed orbit offset of the extracted phase space at the entrance to the extraction channel was removed and the resultant taken as the initial phase space distribution for the beamline. This phase space was tracked to the target and dump with the program MAD[7] to determine the resultant distributions at those locations. The horizontal and vertical phase space of the primary beam at the face of the Lambertson and at the center of a 2 mm radius production target are shown in Figure 3.1. The target spot size has previously been shown to have a wide range of horizontal and vertical tunability[2].

The resonantly extracted horizontal beam distribution is smaller in both x and x' than that of the nominal Main Injector optics, as expected since resonant extraction produces a distribution with a hard edge in the horizontal dimension due the septa wires and finite step size. The vertical distribution of the extracted beam, however, remains a Gaussian matched to the nominal Main Injector optics.

Beamline Description The selection of MI-60 as the extraction point from the Main Injector was based on the orientation of that straight section with respect to the bearing to Soudan. The difference between those bearings is 3.4233 degrees, thus requiring only minimal bending to aim the beam toward Soudan. Table 3.1 summarizes the bearings and elevations for MI-60 and the Soudan mine based upon a Global Positioning Satellite tie to the outside of the Soudan mine[3].

MI60 heading	148.7685	degrees
Soudan heading	152.1918	degrees
MI60 elevation	715.724	feet
Soudan elevation	-683.8090	feet
Soudan pitch	-3.34016	degrees

Table 3.1: The bearings and elevations for MI-60 and the Soudan mine.

Three bend centers are required to place the beam on the proper trajectory to Soudan. They are, in the order they come in the beamline:

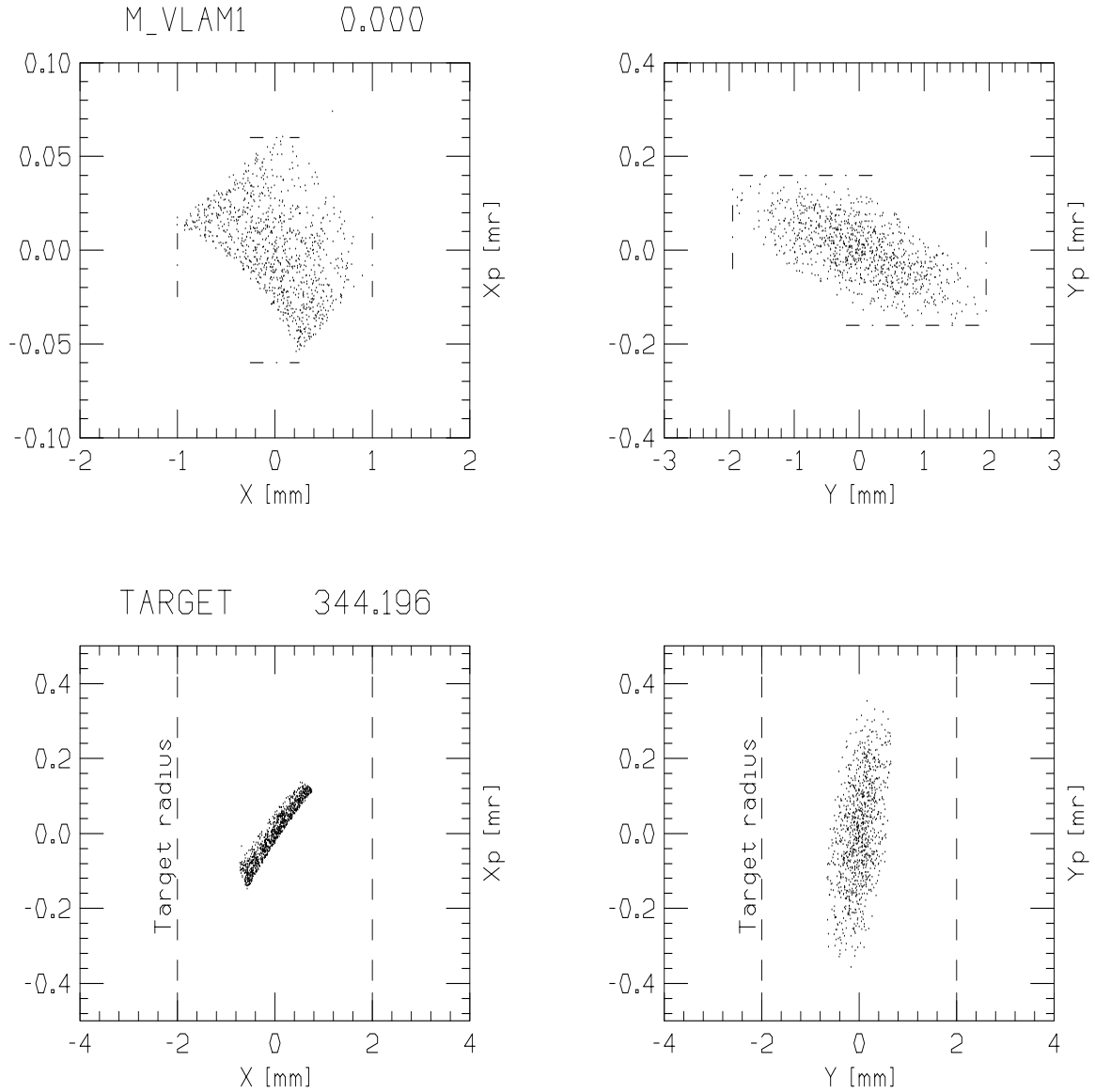


Figure 3.1: The horizontal and vertical phase space of the extracted beam (simulation) at the face of the extraction Lambertson and at the longitudinal center of the target. The dot-dashed marks on the top figures represent the maximum values of x , x' , y and y' used as input parameters to Transport. The dashed lines on the lower figure represent the extent of the 2 mm radius target.

- a horizontal bend center in the Main Injector tunnel to establish the proper bearing,
- a vertical bend center, in the extraction stub, to bend the beam down toward the pretarget enclosure,
- a second vertical bend center, in the pretarget enclosure, to establish the proper pitch to Soudan.

In addition to these bend centers, 10 quadrupoles are required for transport and final focus. Besides these elements, the normal complement of beam diagnostics, trim magnets, and support equipment are required. Site coordinates at the entrance of all the physical beamline elements for the Wide Band Beam are given in Appendix A.

Main Injector Extraction Geometry Two twelve foot Main Injector extraction septum modules are located upstream of MI quad Q602, which is 270 degrees in betatron phase upstream of the extraction Lambertson located at MI Q608. These modules produce approximately 400 μ r of kick, providing \sim 12 mm separation between the circulating and extracted beams at the Lambertson face.

The extraction channel, which is similar in design to others from the Main Injector[4], is located at quad Q608 at the downstream end of the RF straight section. It is composed of three Main Injector Lambertsons, each producing a bend of 6.25 mr, and a Main Injector C-magnet producing a vertical bend of 8.4 mr. These elements provide the vertical pitch required to clear the downstream Main Injector quad Q609 and the subsequent dipoles.

To minimize the impact on the Main Injector enclosure, the extraction and transport line follows the footprint of the Main Injector ring, rising to a final elevation of 718.929 feet or about 3.2 feet above the Main Injector centerline. Figure 3.2 shows the geometry of the extraction and beamline elements as well as the Main Injector magnets for the region inside the Main Injector tunnel. The final elevation of this transport section was selected to avoid interference with the Recycler Ring (which is at an elevation of 720.169 feet) and the A150 beamline at the entrance to the extraction stub. The A150 beamline elevation at the downstream end of dipole 904, where this transport line crosses, is 717.97 feet, giving a clearance of 4 inches between the magnet and transport line.

Transport in the Main Injector Tunnel The first magnetic element in the transport line following the extraction C-magnet is a defocusing quad, Q101, just upstream of MI Q609. This quad is followed by a 4.1 m drift allowing the trajectory to rise to 46.25 cm above the Main Injector centerline before the next

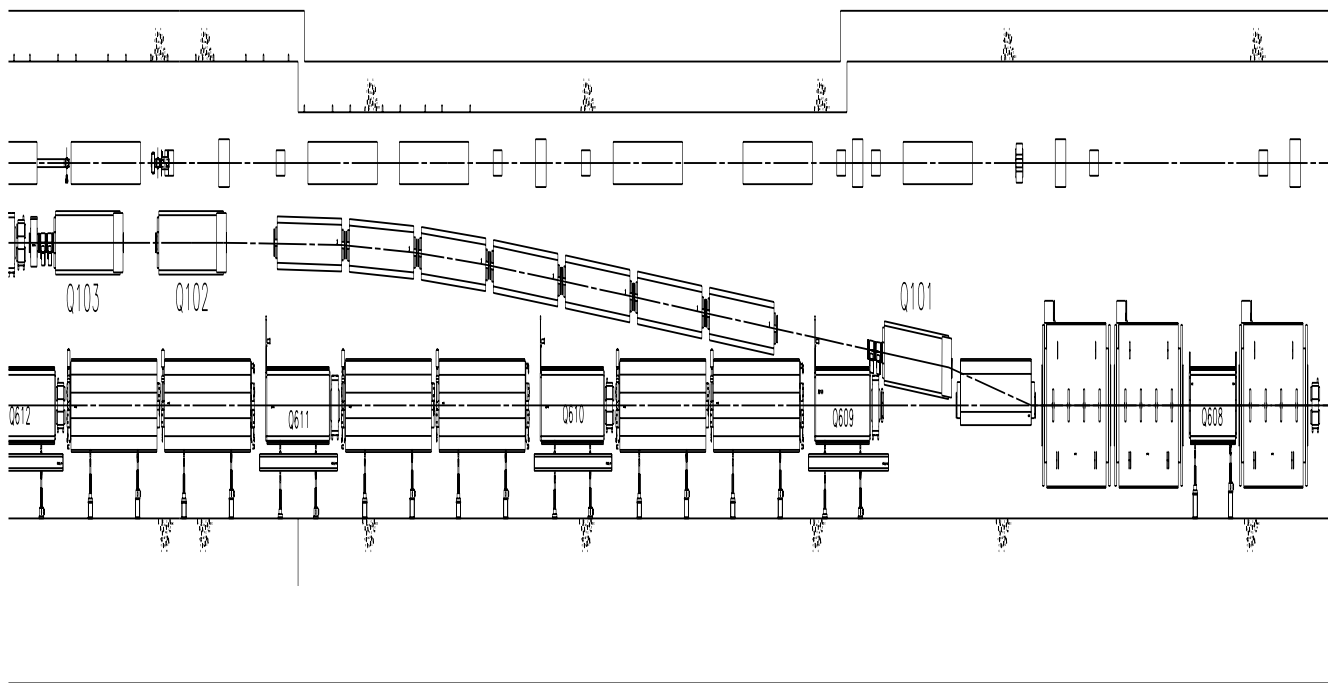


Figure 3.2: Elevation view of the Recycler Ring (top), NuMI extraction beamline (center), and the MI ring (bottom). The beam direction is from right to left. The MI quad 608 is located between the first two (of three) 10' extraction Lambertsons. The instrumentation package and trim package is shown downstream of the last quad in the MI tunnel, Q103. Note: The vertical scale is exaggerated.

magnetic element. The first dipole string is made up of seven EPB dipoles, denoted as HV101(1-7), and runs at approximately 1,470 Amps. EPB dipoles were chosen over MR B2 magnets due to their small cross-section and weight, and lower operating current. Utilizing several sets of dipole roll angles, this dipole string maintains its footprint over the Main Injector, places the beamline on the proper horizontal trajectory to Soudan, and levels the vertical trajectory to clear the A150 beamline 54 meters downstream. Table 3.2 summarizes the required dipoles, power supply circuits, bend angles, strengths, approximate operating currents, and roll angles with respect to a nominal horizontal bend for the entire Wide Band beamline.

Circuit	Magnet(s)	Type	Roll [degrees]	Angle [mr]	Strength [kG]	Current [kA]
1	L608(1-3)	MI lam	90	6.25	8.58	1.68
2	V100	MI cmg	90	8.4	10.03	2.73
3	HV101(1-2)	EPB	0.0	-10.7	-14.05	-1.47
	HV101(3-4)	EPB	4.24	-10.7	-14.05	-1.47
	HV101(5-7)	EPB	56.1	-10.7	-14.05	-1.47
4	V105(1-4)	B2	90.0	-26.1	-17.24	-4.37
5	V109(1-6)	EPB	90.0	7.7	10.1	.97

Table 3.2: Nominal Dipole Strengths for the Wide Band Beam.

The last magnetic elements in the Main Injector tunnel are a pair of quads, Q102 and Q103, located in the middle of the Main Injector half cell 611 and centered over the Main Injector centerline. A 54 m drift transports the beam from this point to the entrance of the extraction stub.

Extraction Stub After the beam crosses the A150 beamline it enters the extraction stub. This section of the beamline is seen in elevation in Figure 3.3. A doublet, Q104 -105 at the entrance to the stub, produces a nearly parallel beam while maintaining reasonable beam sizes through the following dipole string. This string is comprised of four recycled B2 dipoles from the Main Ring, denoted as V105(1-4), which are rolled 90 degrees to produce the -104.59 mr vertical pitch to the pretarget enclosure. These B2s are utilized on the basis of a higher design field than the EPBs (1.788T vs 1.5T) and larger aperture (2" H \times 4" V in the rolled orientation). A second doublet, Q106-107, following the dipole string, maintains reasonable beam sizes for transport through the 110 meter drift to the pretarget enclosure.

The extraction stub extends approximately 160 feet beyond the Main Injector enclosure, with an 8.5 foot step in the elevation of the floor, from the

713.5 foot Main Injector floor elevation to 705 feet in the stub. A 4 foot diameter steel plug centered at an elevation of 708.417 feet is embedded in the downstream end wall for connection with a carrier pipe to the pretarget enclosure. The elevation of the beamline as it exits the extraction stub is 708.3 feet, which is about 1.4 inches below the carrier pipe centerline and about 7.4 feet below the Main Injector centerline.

To provide the flexibility for a Narrow Band Beam, the vertical angle of V105 can be reduced by 2mr, raising the beamline elevation by about 2.4 inches, or 1.1 inches above the centerline of the carrier pipe in the stub, and by about 11 inches at the entrance to the pretarget hall.

Pretarget Hall The pretarget hall is located 366 feet downstream of the MI-60 extraction stub and the elevation of the beamline at its entrance 670.1 feet. The configuration of its beamline elements is shown in Figure 3.4.

The beam enters the pretarget hall at a vertical pitch of -104.59 mr (or -5.99 degrees). This pitch is reduced to -58.297 mr, that required to reach Soudan, by a string of six vertically bending EPB dipoles, denoted as V109(1-6) and operated at ~ 1000 Amps (Table 3.1). There are no other bending elements in the Wide Band beamline besides the trim dipoles. The target is at an elevation of 652.13 feet and installed at the same -58.297 mr pitch. All subsequent optics and the decay tunnel are at this same angle. This places the primary beam absorber (800 meters downstream of the target) at a depth of roughly 241 feet.

Beamline Optics The calculation of the beam optics for the transport line utilizes a beam description based upon the above extraction simulations. The maximum extent $\sqrt{\sigma_{11}}$, $\sqrt{\sigma_{33}}$ and divergence $\sqrt{\sigma_{22}}$, $\sqrt{\sigma_{44}}$ at the entrance face of the first extraction Lambertson, as shown by the dot-dashed lines in Figure 3.1, were taken as the input beam description. The envelope throughout the beamline and across the target are shown in Figure 3.5, with the half-size before the target everywhere less than 15 mm. The minimum aperture of this line is that of the EPB dipoles, 1.5 inches (± 19 mm) in the non-bend plane.

The final target optics consist of three 3Q120 quads to focus the beam both horizontally and vertically. The distance between the last quad, Q210, and the target is ~ 20 meters. The spot size on the target is a function not only of the gradients in these quads but also of the phase space distribution at their entrance. Therefore, in addition to the triplet, the last two quads in the extraction stub enclosure, Q106-107, are adjusted in this simulation. Table 3.3 summarizes the required gradients for the nominal ± 1 mm spot size on the target based upon the current description of the extracted beam. Assuming that a ± 0.5 meter spot size on the the face of the dump is acceptable, the maximum

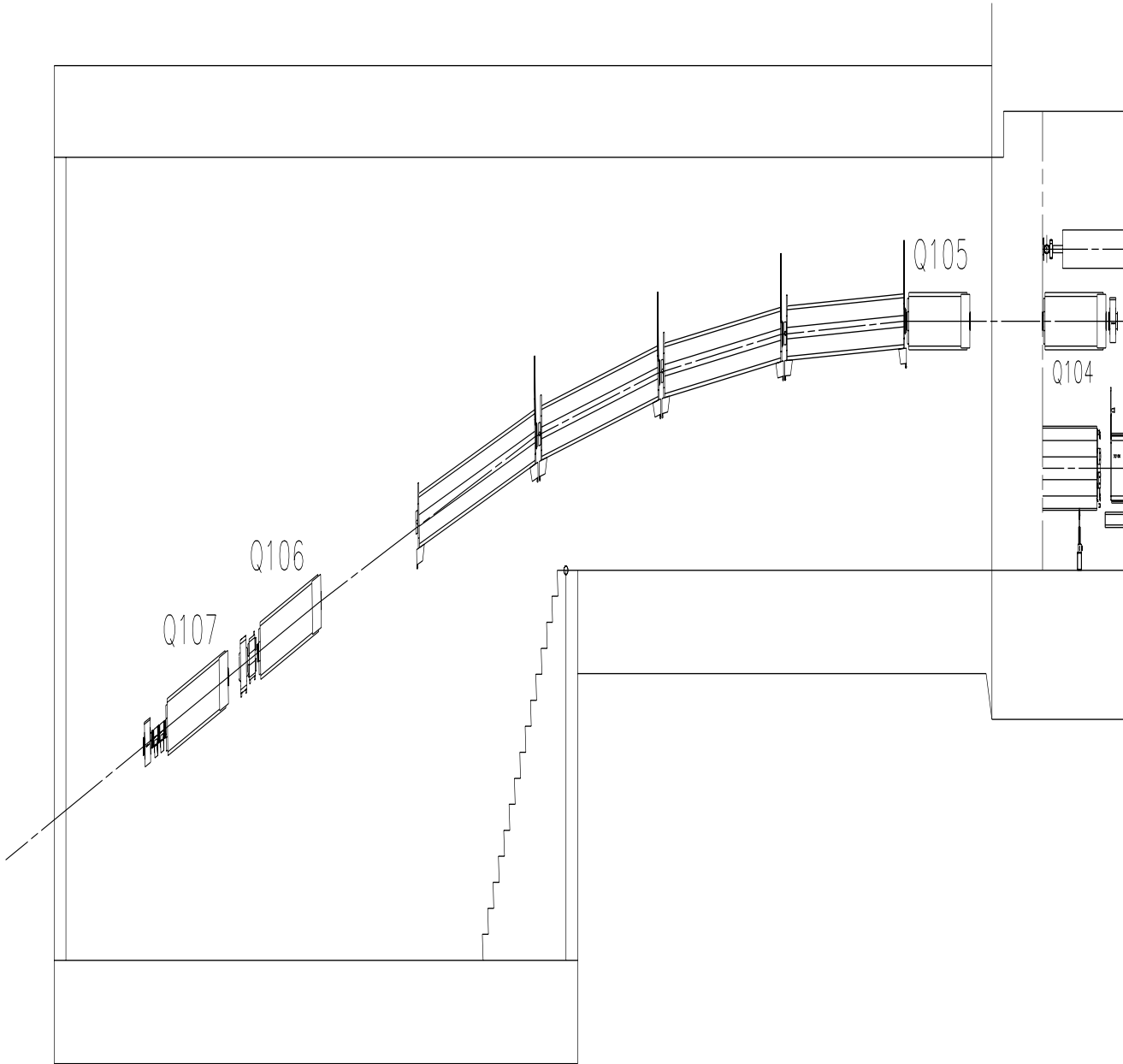


Figure 3.3: Elevation view of the NuMI beamline in the extraction stub starting with the BPM and SWIC just upstream of Q104. The beam direction is from right to left. Shown are the quad doublet (Q104/Q105), four vertical dipoles (V105), and the quad doublet (Q106/Q107) with horizontal and vertical trim magnets between Q106 and Q107. The last elements shown are the horizontal and vertical BPMs and SWIC profile monitor. The loss monitors are not shown. Note: The vertical scale is exaggerated.

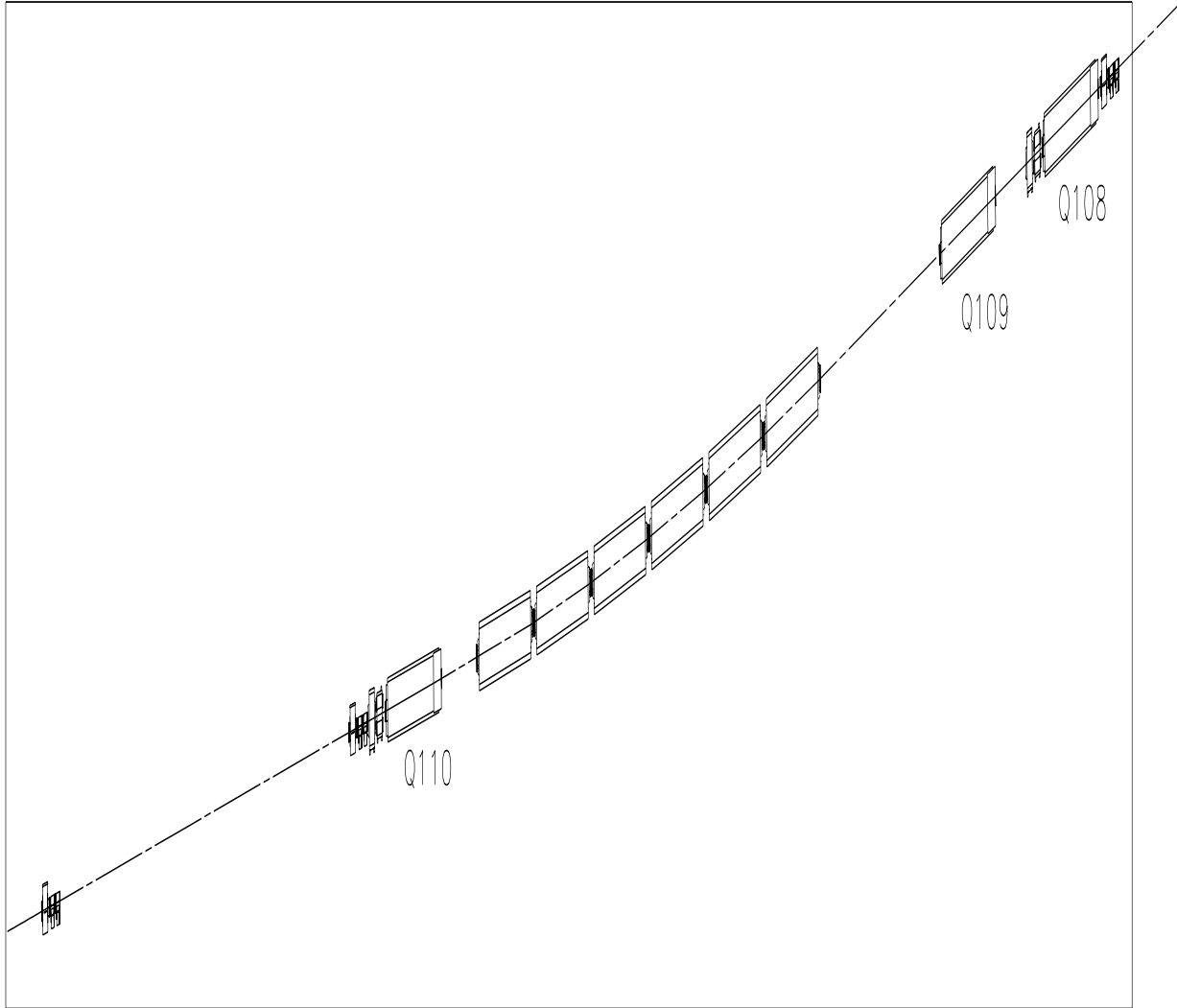


Figure 3.4: Elevation view of the pretarget area showing the Wide Band primary beamline. The beam direction is from right to left. The first elements at the entrance to the pretarget area are quads Q108 and Q109, with the BPMs and SWIC just upstream of Q108 and the correctors between quads. The vertical bend, V109, is shown next. Quad Q110 and the associated horizontal and vertical trims are the last magnetic elements. The target BPMs and SEEDs follow separated by approximately 20 meters and are the last elements in the beamline before the target vault. Note: The vertical scale is exaggerated.

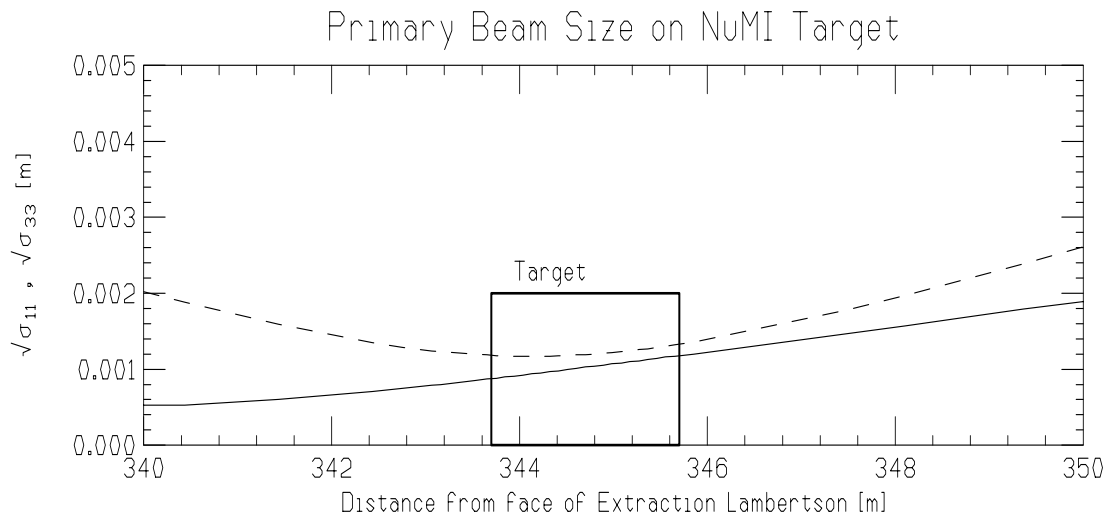
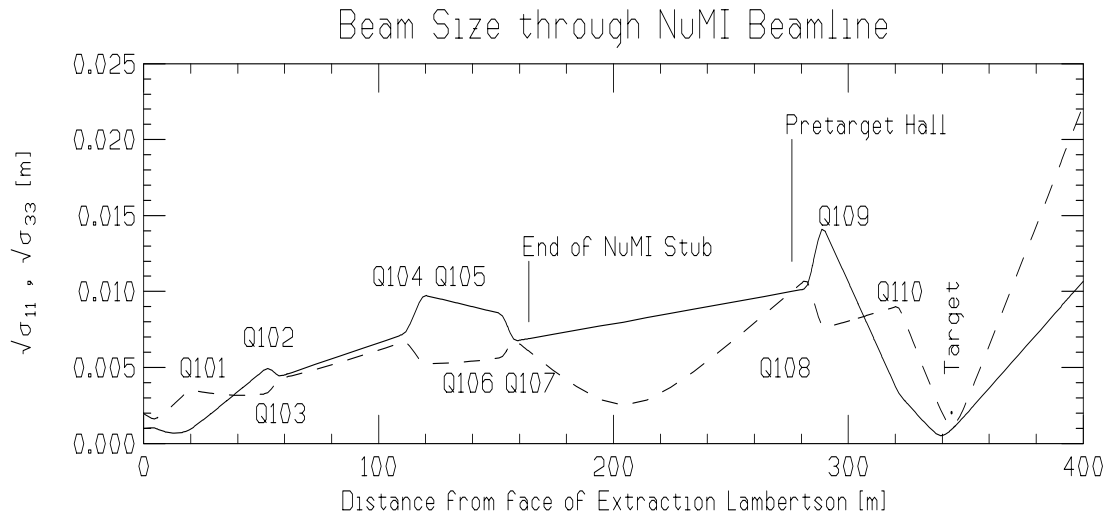


Figure 3.5: Half size of the primary beam through the NuMI beamline and target, with horizontal beam size the solid line. The initial values for x , x' , y , y' were derived from the extracted phase space shown in Figure 3.1.

divergence allowed for the primary beam is $625 \mu\text{r}$.

Magnet	Strength kG/m
Q101	-72.37
Q102	69.93
Q103	-53.72
Q104	-53.72
Q105	53.72
Q106	53.79
Q107	-73.66
Q108	-86.62
Q109	101.44
Q110	-70.08

Table 3.3: Nominal Quad Strengths.

Instrumentation The instrumentation for the primary beamline will consist of 30 cm Switchyard-type horizontal and vertical resonant BPMs, with resolution of $\sim 100 \mu\text{m}$, Segmented Wire Ion Chamber (SWIC) profile monitors of various wire spacing, high resolution SEED profile monitors just upstream of the target, loss monitors, an RF spill monitor, and a beam current toroid. The location of the instrumentation is chosen to aid in tuning for loss-free transmission and for the setting of the targeting position and angle. With the exception of the horizontal and vertical BPMs at Q101 to monitor the extraction position, it is envisioned that there will be an instrumentation package consisting of a horizontal BPM, a vertical BPM, and a SWIC at each of several locations. Specifically they will be located at either end of three drift sections - between Q103 and Q104, between Q107 and Q108, and between Q110 and the target. The SWICs consist of 48 wires in each plane with a typical spacing of 1 mm. The target SEEDs, which function via secondary emission rather than ionization, have a $250 \mu\text{m}$ wire spacing. With a five meter separation and a $125 \mu\text{m}$ resolution on the centroid, a targeting angle precision of $25 \mu\text{r}$ should be achievable. A set of 26 loss monitors will be placed near the extraction elements (8), the EPBs in the Main Injector tunnel (5), the quads and vertical bends in the NuMI stub (6) and the quads and bends in the pretarget hall (7). Details of additional loss monitors which may be installed in front of the target shield for component protection have not yet been determined.

Correctors The Main-Injector-type horizontal and vertical dipole correctors produce .06 T-m and .03 T-m, respectively, at 10 Amps. At 120 GeV these correspond to angles of Θ_h of $150\mu r$ and Θ_v of $75\mu r$, sufficient for orbit control through the line and targeting position, and angle adjustment. Two sets of horizontal and vertical correctors are installed in the Main Injector tunnel and extraction stub, and are used for position control through the beamline and carrier pipe. An additional two sets of horizontal and vertical correctors are installed in the pretarget hall to be used for targeting.

The first set of horizontal and vertical correctors is located after the Q102-Q103 doublet. These will be used as independent H/V trims for steering into the HV101 magnet string. The second set is located between Q106 and Q107 and will allow independent control of the horizontal and vertical trajectory through the the rolled dipoles in the pretarget hall. The last two sets, located at Q108 and downstream of Q110, will be used to fine-tune the position and angle on the target. Combinations will be constructed to allow independent control in each plane.

Power and utilities There are 5 high-current bend circuits including the Lambertson magnet and the C-magnet circuits, 8 different quadrupole circuits (Q1 through Q8), and 8 different low-current trim magnet circuits. The bend and quadrupole power supplies will come from unused fixed target beamline locations while the trim power supplies will come from the old main ring dipole correction element system.

The Lambertson, C-magnet, and first 2 bend circuits are all located within the Main Injector enclosure and the power supplies for these circuits will be located in the MI-60 service building. This location minimizes the length of cables needed to connect the supplies to the magnets. The present plan is to use an existing spare transformer pad at MI-60 for locating the substation. It will be necessary to connect the substation to the 13.8kV beamline feeder and install a 480VAC power panel in the MI-60 building. The power supplies for the quadrupoles in the Main Injector enclosure will be located in the MI-62 service building. The cable runs to the magnets are somewhat longer, but there is plenty of space and AC power in this service building for these components. The trim magnets installed in the MI enclosure will also have power supplies located in MI-60. The power supplies for the last string of bend magnets, 3 of the quadrupole circuits, and the remaining 4 trim circuits (located in the pretarget enclosure) will be located in the service building above the target hall.

Initial estimates of the LCW requirements reflect dissipating about 300 kW of power. This can be accomplished using a single 60 hp LCW pump flowing 300 GPM[8].

3.2 Target

Target Geometry Ideally the target and horn focusing system are designed as a unit to maximize the ν_μ charged current event rate at the MINOS far detector and minimize the backgrounds at the COSMOS location. Since a system of horns has a large depth of field, the maximum event rate is accomplished through use of a long target with a small cross-sectional area. The optimal choice of target radius is driven by two opposing trends: the flux of pions and kaons out of the target decreases with increasing target radius (for a cylindrical target) due to particle reabsorption, but target stability under the enormous heat load from the high intensity proton beam increases with target radius. There is the further constraint that the target cross-sectional area should be large enough to contain most of the beam since protons which miss the target and interact in the hadron absorber at the end of the decay tunnel produce unacceptable backgrounds for COSMOS. This also argues towards making a target as long as possible in order that most of the protons on target interact.

Various target designs have been studied in the past using the CASIM[9] Monte Carlo program and secondary particle production of FN-341[17], and the MARS Monte Carlo program[10]. Gaussian proton beams of either circular or ellipsoidal profile were assumed. Beryllium, graphite, and nickel were taken as possible target materials while cylindrical geometry of the target, either a single rod or a series of rods with gaps, was assumed.

The yield of positive pions from the target was studied as function of target length, L_t , and density[11]. In this study the target was modeled as a solid rod with a tuneable density. The maximum relative π^+ yield (relative to that from a 1m long graphite target) and optimal target density for several angular regions¹ are shown as function of target length L_t in Figure 3.6. From these studies it was found that the optimal target length and density are ~ 160 cm and 1.2 g/cm³, respectively. Graphite has a density of 1.81 g/cm³ and so to reach an “effective” density of 1.2 g/cm³ it is necessary to break the target up into segments separated by gaps filled with much lower density material like air or helium.

Target Heating and Stresses The target temperature profile is characterized by an average steady-state temperature and a jump in temperature during the beam spill. The size of the temperature jump depends on the proton beam characteristics and on the target material heat properties. The steady-state temperature is set by the cooling system efficiency. The target is to be cooled

¹Where θ_z is the angle of the π^+ trajectory with respect to the incident proton direction, i.e., the z axis.

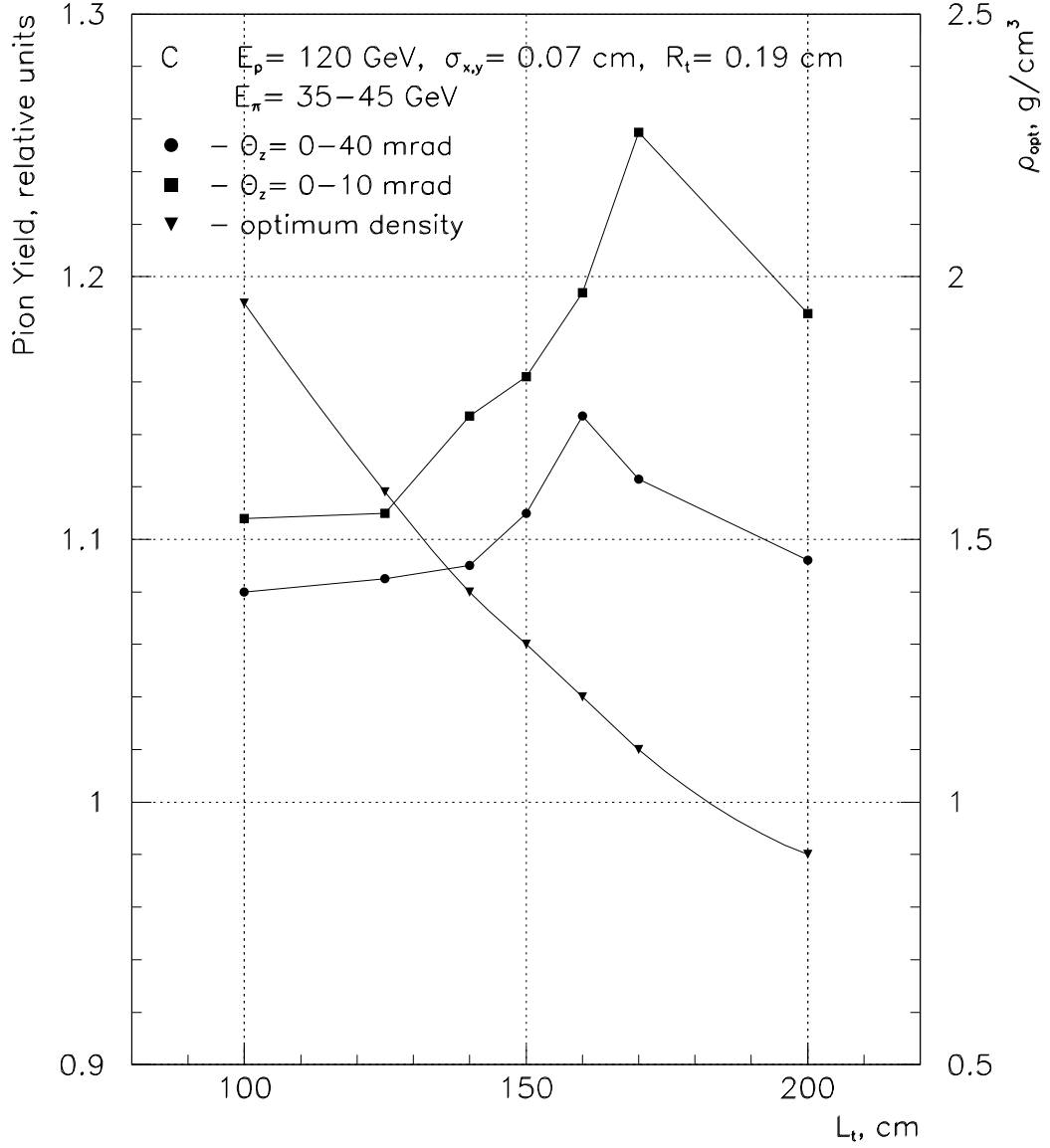


Figure 3.6: The relative pion yield and optimal target density (right hand axis) as a function of target length[11]. E_p is the proton beam energy, $\sigma_{x,y}$ are the transverse Gaussian beam dimensions, R_t is the target radius, E_π is the pion energy, and Θ_Z is the angle between the pion trajectory and the beam axis.

by forced helium gas convection since the thermal load on a target with natural cooling (i.e., by non-forced convection and radiation) would be high enough to compromise the target's useful lifetime. Figure 3.7 shows the temperature

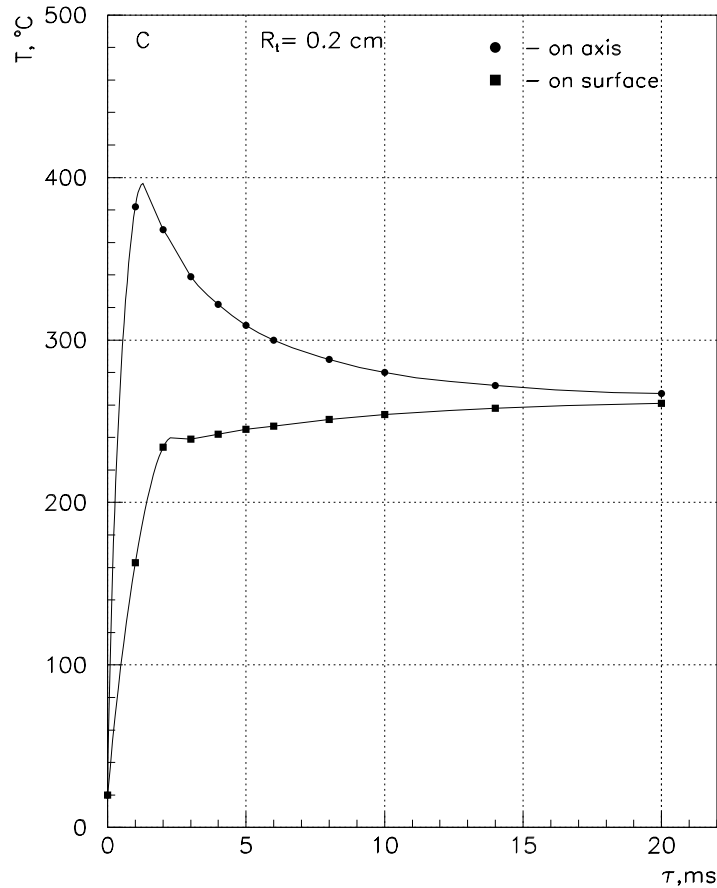


Figure 3.7: Temperature change on the axis and on the surface of a target after a single proton spill[11].

on the surface and on the axis of a 2 mm radius graphite target after a single proton spill. The calculation takes into account the variation of the specific heat of graphite with temperature. In general, for various helium flow rates, the steady-state temperature is reached within 10-20 spills. For relatively modest helium flow rates (flow speed of 4 m/s) the steady-state temperature of such a target is calculated to be around 800 °C.

Figure 3.8 shows the relationship between the quasi-static temperature stress in a cylindrical graphite target and the proton beam size σ_p (where a symmetric Gaussian beam is assumed). The dashed line is the structural limit

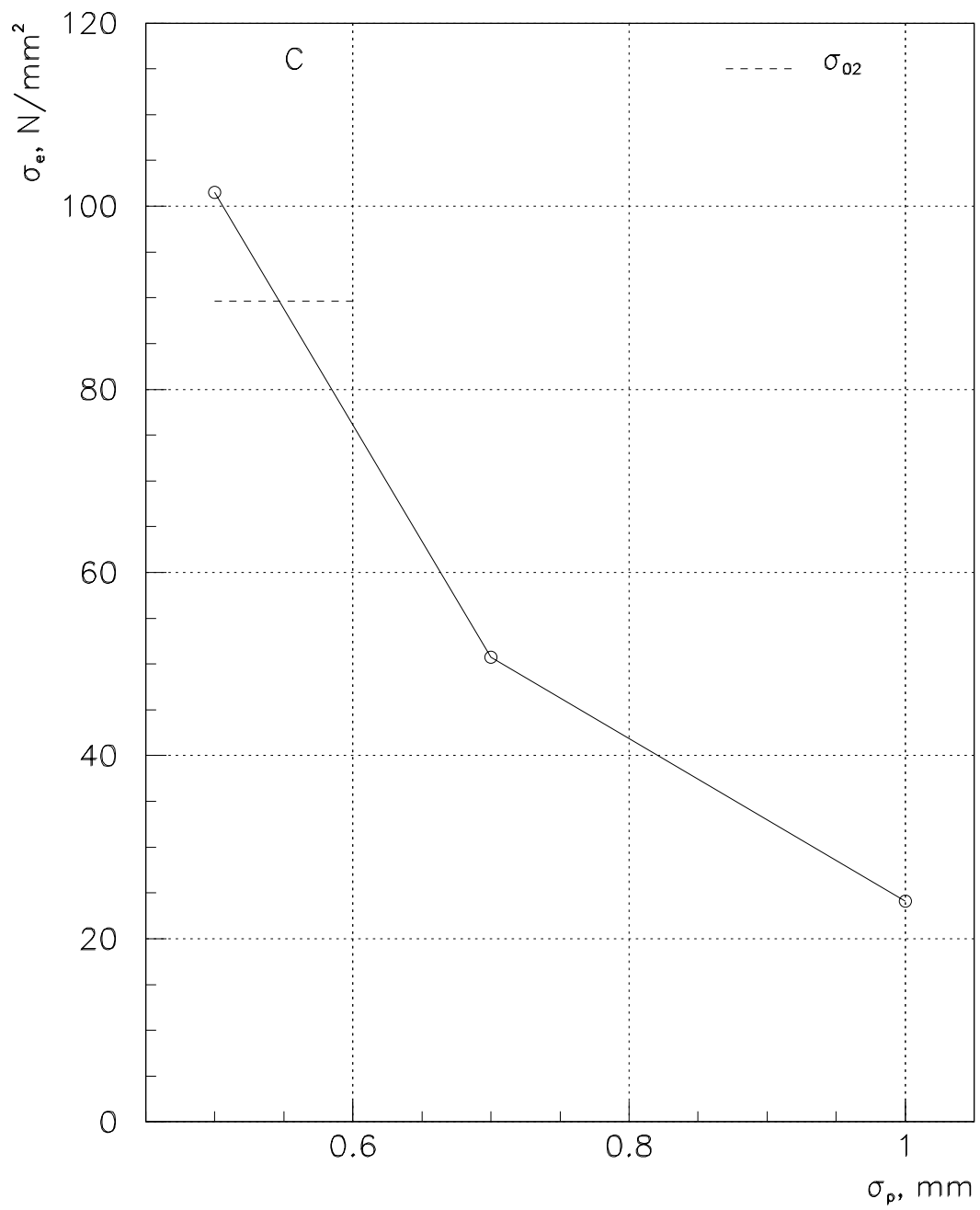


Figure 3.8: Stress on target as a function of beam spot size[11].

of the material. Hence, for graphite, σ_p must be greater than 0.55 mm although a safety factor of at least 3 is probably necessary to take into account fatigue effects from thermocyclic loading and radiation damage of the target material. Graphite is found to be a better material than beryllium at withstanding the stresses induced by the Main Injector proton beam.

Alternative target head designs, e.g., as shown in Figure 3.10, are being investigated. More realistic yield estimates will have to wait for a detailed design which includes target mounting and cooling.

The Target in GNuMI The target in the GEANT based GNuMI Monte Carlo program (see Appendix B) consists of eight 12.5 cm long graphite rods, each 2 mm in radius, separated by 8 cm long gaps. The beam profile in GNuMI, illustrated in Figure 3.9 which shows the transverse position of the proton interactions in the first target segment, is a much better representation of the shape of the beam than the simple Gaussian beam shapes.

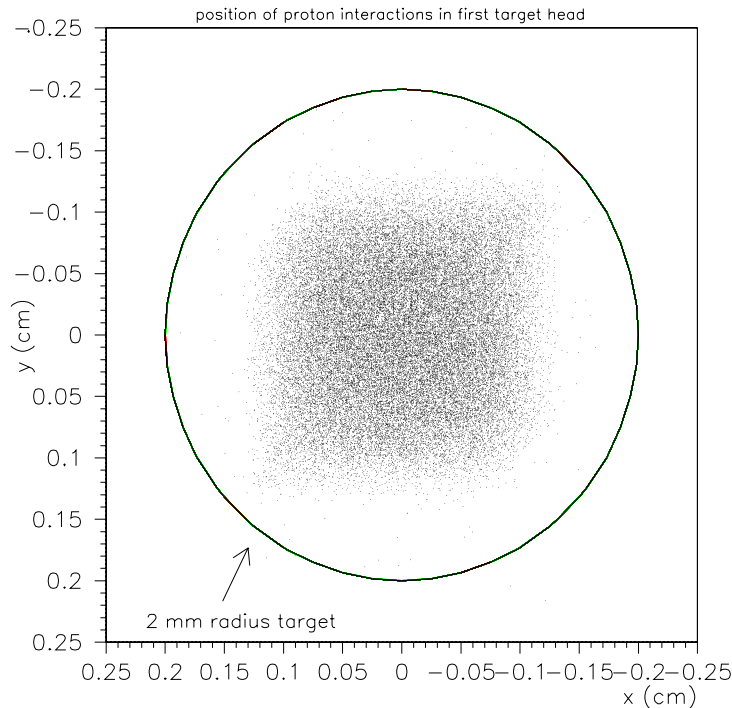


Figure 3.9: The transverse position of the proton interactions in the first target rod, as simulated in GNuMI.

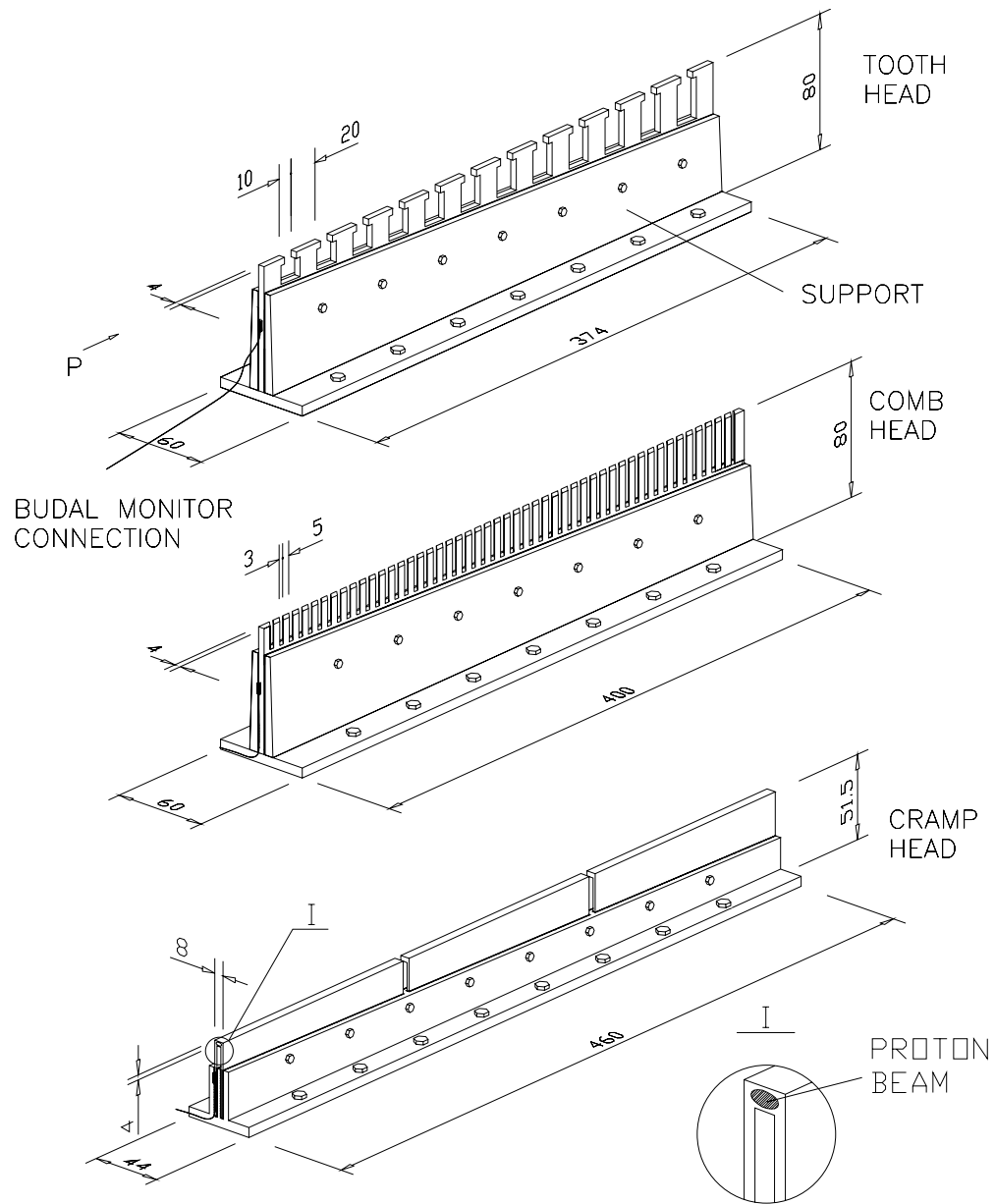


Figure 3.10: Several target designs[11].

3.3 Focusing System - Wide Band Beam

3.3.1 Horn Focusing

Focusing Scheme Figure 3.11 illustrates the working of the multi-horn focusing system. In this event, a π^+ enters the first horn through the sloping inner conductor, is initially overfocused, goes through the hole in the center of the second horn, and is focused parallel to the decay pipe by the third horn. The actual shapes of the horns are better seen in Figure 3.12, and the parameters are listed in Table 3.4.

	Horn 1	Horn 2	Horn 3
Location (Z)	0 m	7.9 m	41.1 m
Length	163 cm	253 cm	253 cm
Outer radius	10 cm	25 cm	25 cm
End wall thickness	5 mm	5 mm	5 mm
Inner Conductor:			
Neck radius	1 cm	2 cm	4 cm
Neck length	3 cm	3 cm	3 cm
Conical length	160 cm	250 cm	250 cm
Cone radius	2.9 cm	16.0 cm	23.5 cm
Thickness neck end	3 mm	2 mm	2 mm
Thickness other end	2 mm	2 mm	2 mm
Current	170 kA	170 kA	170 kA
“Flat top”	1 ms	1 ms	1 ms

Table 3.4: Horn parameters, 3 horn design. They are as originally proposed in Reference [13], except the neck region is thickened to 3 mm, and the conical section then tapers down to a thickness of 2 mm .

Many types of horn shapes have been used in the past. One type approximated a lens, so that a single horn would focus secondaries from all production angles for a particular momentum. Another type was designed to focus a particular p_t for all momenta. The system described in this document is a compromise design, in which there is some correlation between focusing power and radius for the first horn, although not as much as for a “lens”. The focusing power as a function of radius is illustrated in Figure 3.13b. The general concept of the multi-horn system is a series of horns in which particles which are well focused go through the hole in the center of the following horns, particles whose trajectories are not bent enough go to a larger radius in the next horn, where they

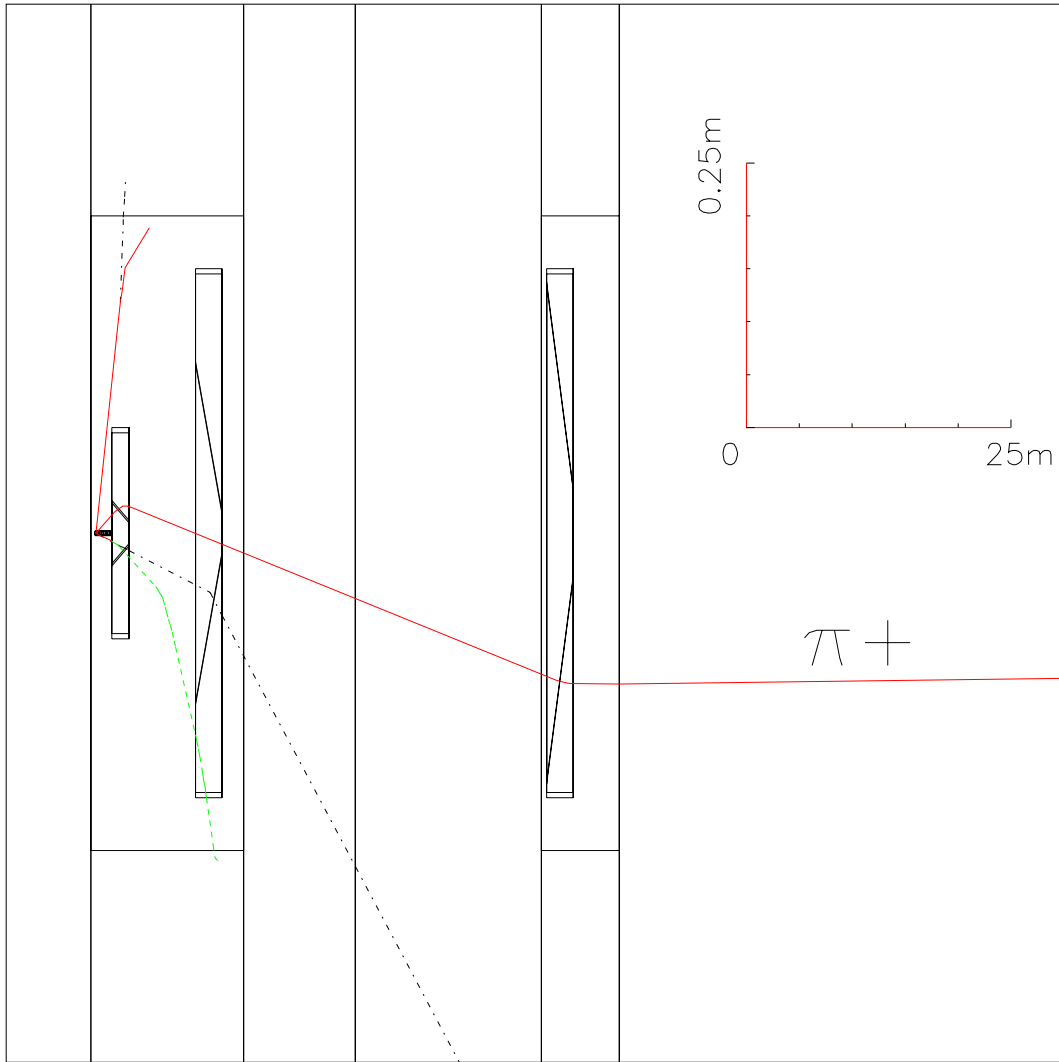


Figure 3.11: An event display from the **GEANT** Monte Carlo, showing a proton interacting in the target and a resulting π^+ being focused by the three-horn system. Note the distance scales on the two axes differ by a factor of one hundred. (The rectangular shapes are shielding blocks.)

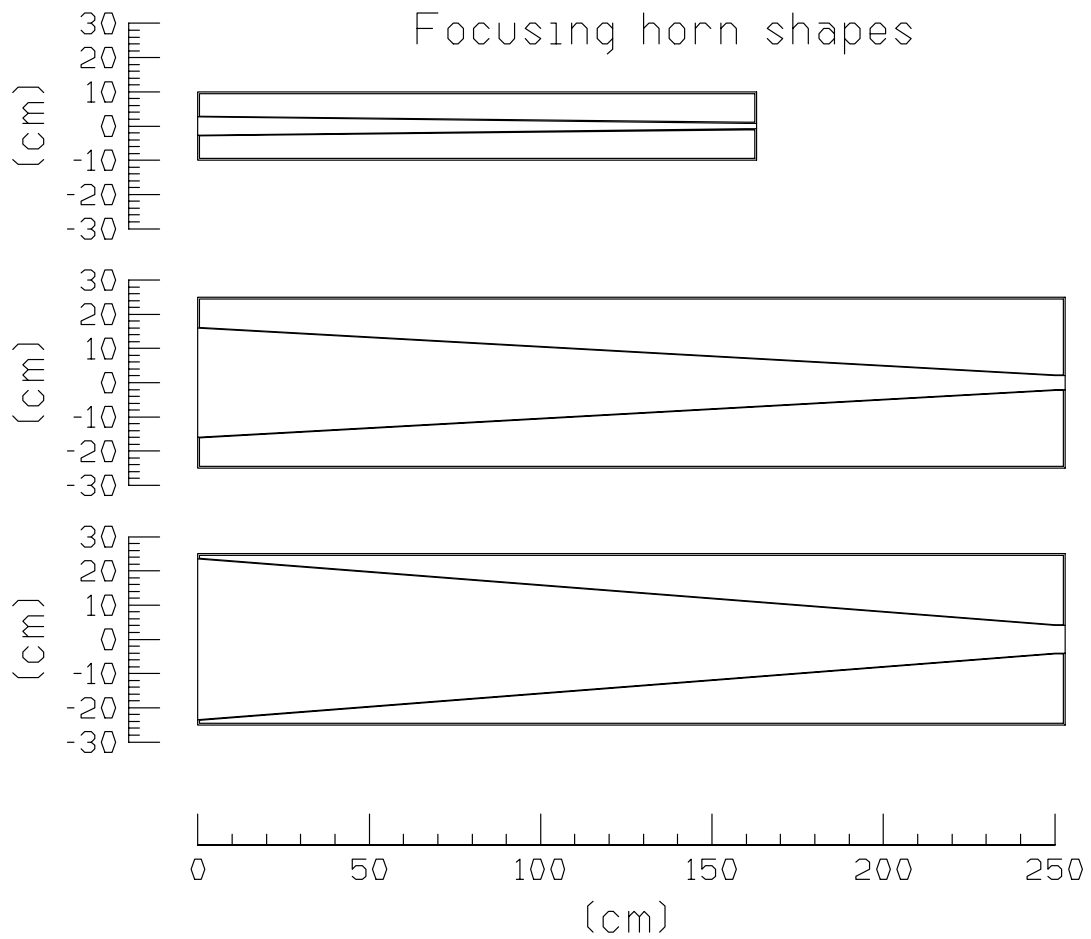


Figure 3.12: Dimensions of the three focusing horns. The inner conductors are conical; the outer conductors are cylindrical.

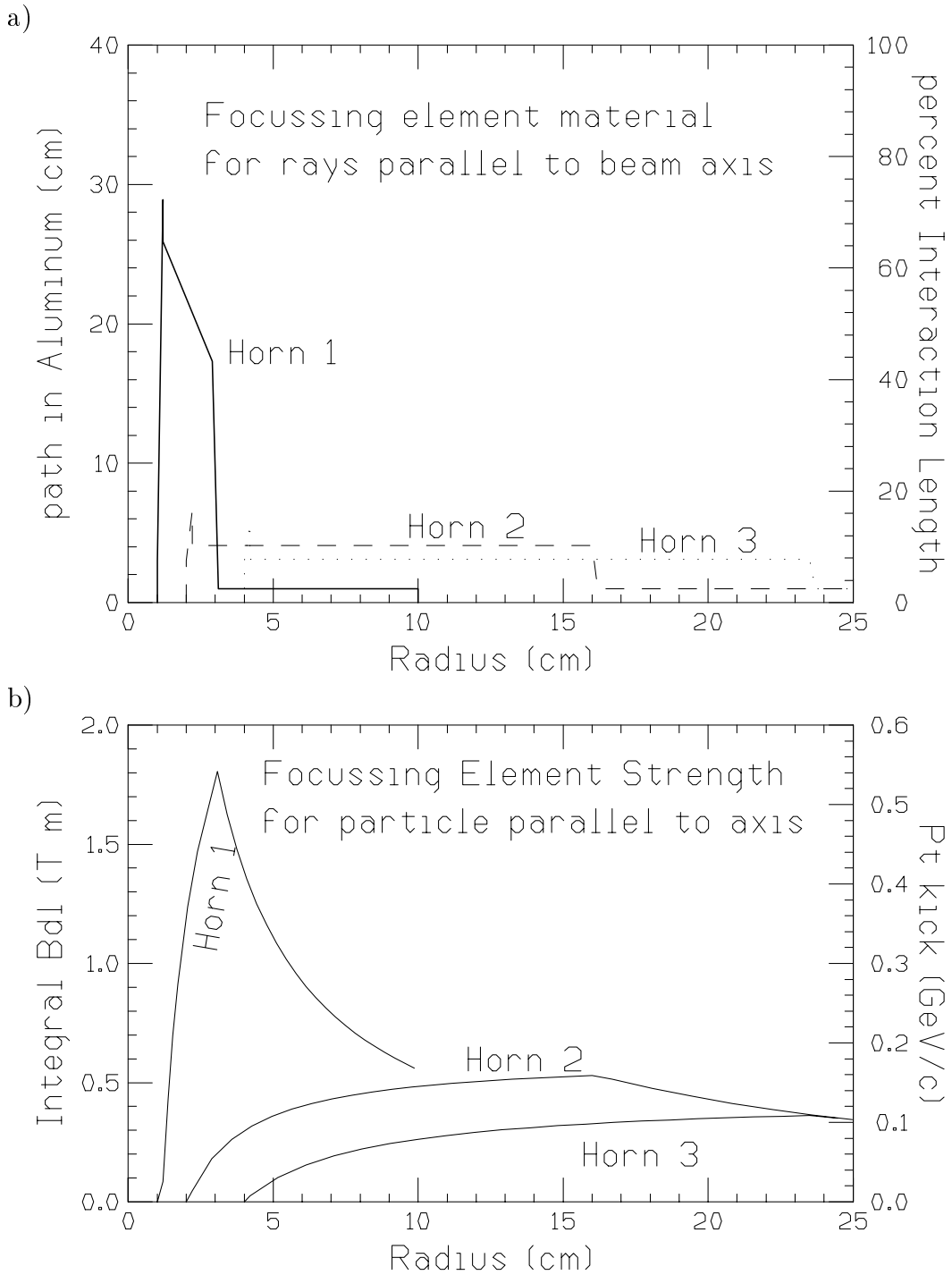


Figure 3.13: The amount of material, and the magnetic field integral, that would be seen by a particle passing through the horns parallel to the beam axis, as a function of radius.

Figure 3.14: Hadron p_t distributions from data taken by Brenner *etal*[12].

The inner conductor of the horns presents a significant amount of material traversed by the pion beam, as can be seen in Figure 3.13a. In the first horn, the angle with which particles enter is about equal to the slope of the inner conductor, which reduces the material seen to about 25% of an interaction length. Figure 3.15 shows that the majority of pions in the 20 - 60 GeV region, where this system is optimized, enter the first horn through the sloping inner conductor.

The conical horn design started with inner radii comparable to other horn systems that have been built and operated, and which allowed a reasonable clearance for staying out of the primary beam spray (Figure 3.5) when some allowance for beam wandering is made. A maximum current of 170 kA was

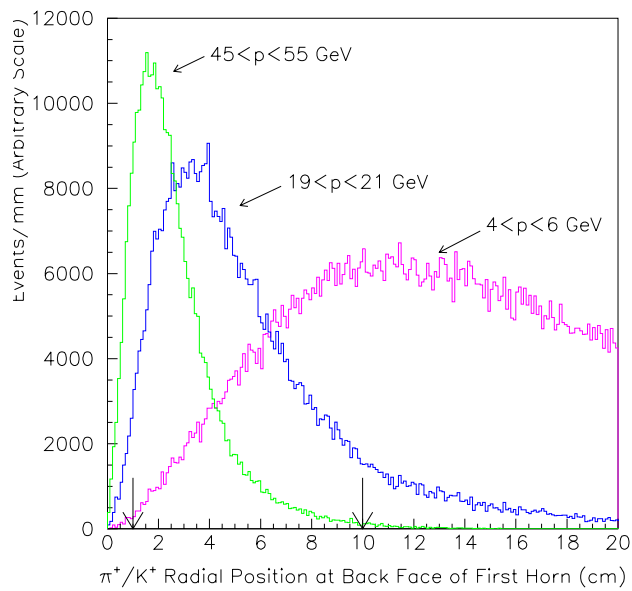
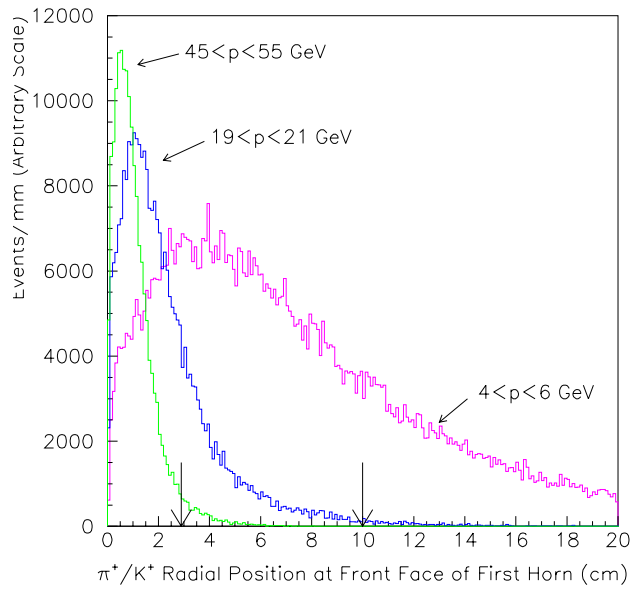


Figure 3.15: The radial distribution of π^+ from the target projected onto the front face and rear faces of the first horn. The arrows indicate the location of the inner and outer horn conductors at each face.

chosen, also to be consistent with previous operation of horn systems. Horn angles, lengths, and positions were then varied to obtain maximum neutrino event rates in the detectors [13].

Three Horns versus Two Table 3.5 shows a comparison of the current three horn system to the two horn system which was presented in the previous design report[1]. The main advantage of the third horn is an increased event rate of 20% to 25% for the two experiments. As an option to increase neutrino event rate, it is a factor of five to ten cheaper than the incremental cost of, e.g., increasing the length of the decay pipe or the mass of the detector. The improved focusing of the three horn system also leads to a modest decrease in radiation hitting the decay pipe walls of about 15%.

Aside from expense, the main possible disadvantages of a third horn are its reliability and associated maintenance questions. However, as discussed in section 3.3.6, the third horn is under much less stress than horn 1, and should be correspondingly more reliable. Further, the third horn takes advantage of the space in the target hall which is required in any case for the narrow band beam option.

From the above considerations, the three horn design has been adopted as the baseline. (A more extensive comparison is presented in Reference [14]).

Alternative Horn Shapes Parabolic horns are also under study [11]. Event rates comparable to the conical horns can be achieved, although the electric current required tends to be higher. The main advantage is that the parabolic horns, with the addition of some dipoles and a beam dump in the target hall, could also be used to produce a narrow band beam. Here, the characteristic of a parabolic horn that it focuses particles of all p_t for a given narrow range of p is used to advantage. However, this characteristic is somewhat of a detriment in a wide band beam. The neutrino energy spectrum from the conical horns tends to be smoother than that for parabolic horns, and may thus be more suited for looking for oscillatory effects in the spectrum. (When the “Hadronic Hose”, described in section 3.3.5, is used both spectra are reasonably smooth.)

Lithium Lens Option Lithium lens designs were also considered. The main drawback is that an extensive R&D program would be required to develop lenses that could match the 1 ms spill time required for wide band beam running. Lithium lenses are also more sensitive to misalignments, and mapping the magnetic field in them appears more challenging than in a horn. On the other hand, a lithium lens design appears to offer superior performance in terms of increased

	<i>Three Horn Design</i>			<i>Two Horn Option</i>	
	Horn 1	Horn 2	Horn 3	Horn 1	Horn 2
Location (Z)	0 m	7.9 m	41.1 m	0 m	22 m
Length	163 cm	253 cm	253 cm	203 cm	203 cm
Outer radius	10 cm	25 cm	25 cm	25 cm	25 cm
End wall thickness	5 mm	5 mm	5 mm	5 mm	5 mm
Inner Conductor:					
Neck radius	1 cm	2 cm	4 cm	1 cm	2.5 cm
Neck length	3 cm	3 cm	3 cm	3 cm	3 cm
Conical length	160 cm	250 cm	250 cm	200 cm	200 cm
Cone radius	2.9 cm	16.0 cm	23.5 cm	3.6 cm	14.5 cm
Thickness neck end*	2 mm	2 mm	2 mm	2 mm	2 mm
Thickness other end	2 mm	2 mm	2 mm	2 mm	2 mm
Current	170 kA	170 kA	170 kA	170 kA	170 kA
“Flat top”	1 ms	1 ms	1 ms	1 ms	1 ms
$\nu_{\mu}^{CC} < E_{\nu} >$ for MINOS	17.6 GeV			17.6 GeV	
ν_{μ}^{CC} (events/kton/yr):					
MINOS	3000			2540	
COSMOS	2.69×10^6			2.16×10^6	

Table 3.5: Horn parameters and neutrino rates in a comparison of the 3 horn design to the 2 horn option. Neutrino rates are calculated using NUADA for a year of 3.7×10^{20} protons on target. (*This comparison was done before engineering studies showed that the neck thickness for horn 1 in either case needed to be increased to 3 mm.)

event rate, and a suppressed low energy neutrino tail for narrow band beam running.

3.3.2 Neutrino Rates

Event rates Figures 3.16 and 3.17 show the flux of neutrinos and the ν_{μ} charged current event rate at the COSMOS detector as a function of energy. Figures 3.18 and 3.19 show the fluxes and rates for the MINOS near and far detectors. The total event rates are listed in Table 3.6. A “year” is defined as 3.7×10^{20} protons on target (POT). This estimate comes from assuming 4×10^{13} protons per spill, a nine month running cycle, and downtimes similar to the

antiproton accumulator experience during collider Run I. Details of the GNUMI Monte Carlo used to generate the rates are given in Appendix B. Absorption by horn cooling water and by helium and air in the target hall have not been taken into account in the rate calculations, and are expected to reduce the neutrino rates by a few percent. High reliability is a premium, and increasing the thickness of the horn inner conductor at the expense of perhaps 10% of the neutrino rate may also be wise.

	<i>Flux</i>		<i>Events</i>	
COSMOS	$\nu/m^2/\text{POT}$		$N^{CC}/\text{ton}/\text{year}$	
ν_μ	1.90×10^{-3}	(97.6%)	3.73×10^6	(98.6%)
$\bar{\nu}_\mu$	3.7×10^{-5}	(1.9%)	2.9×10^4	(0.77%)
ν_e	1.0×10^{-5}	(0.53%)	2.3×10^4	(0.61%)
$\bar{\nu}_e$	4.9×10^{-7}	(0.03%)	5.4×10^2	(0.01%)
MINOS Near	$\nu/m^2/\text{POT}$		$N^{CC}/\text{kton}/\text{year}$	
ν_μ	1.04×10^{-3}	(97.8%)	2.26×10^9	(98.7%)
$\bar{\nu}_\mu$	1.9×10^{-5}	(1.8%)	1.7×10^7	(0.75%)
ν_e	4.9×10^{-6}	(0.46%)	1.1×10^7	(0.49%)
$\bar{\nu}_e$	2.3×10^{-7}	(0.02%)	2.7×10^5	(0.01%)
MINOS Far	$\nu/m^2/\text{POT}$		$N^{CC}/\text{kton}/\text{year}$	
ν_μ	1.72×10^{-9}	(97.6%)	3846	(98.7%)
$\bar{\nu}_\mu$	3.4×10^{-11}	(1.9%)	33	(0.85%)
ν_e	7.6×10^{-12}	(0.43%)	19	(0.48%)
$\bar{\nu}_e$	5.4×10^{-13}	(0.03%)	0.6	(0.02%)

Table 3.6: Neutrino fluxes and charged current event rates at the detector locations according to the GNUMI Monte Carlo. The MINOS near detector rate is at the beamline center, 500 m beyond the end of the decay pipe. The COSMOS rate is averaged over a 1.4 m by 1.8 m square centered on the beam line, 250 m beyond the end of the decay pipe.

Rate Uncertainties The calculation of the neutrino flux has a significant uncertainty, of order 20% at this time, because of lack of precise knowledge of the hadron production spectrum from the target. (Sections 3.3.4 and 3.3.5 will explain how to reduce this uncertainty.)

Figure 3.20 shows the source of neutrino charged current events broken down by where the decaying particle was produced, and by decay channel for

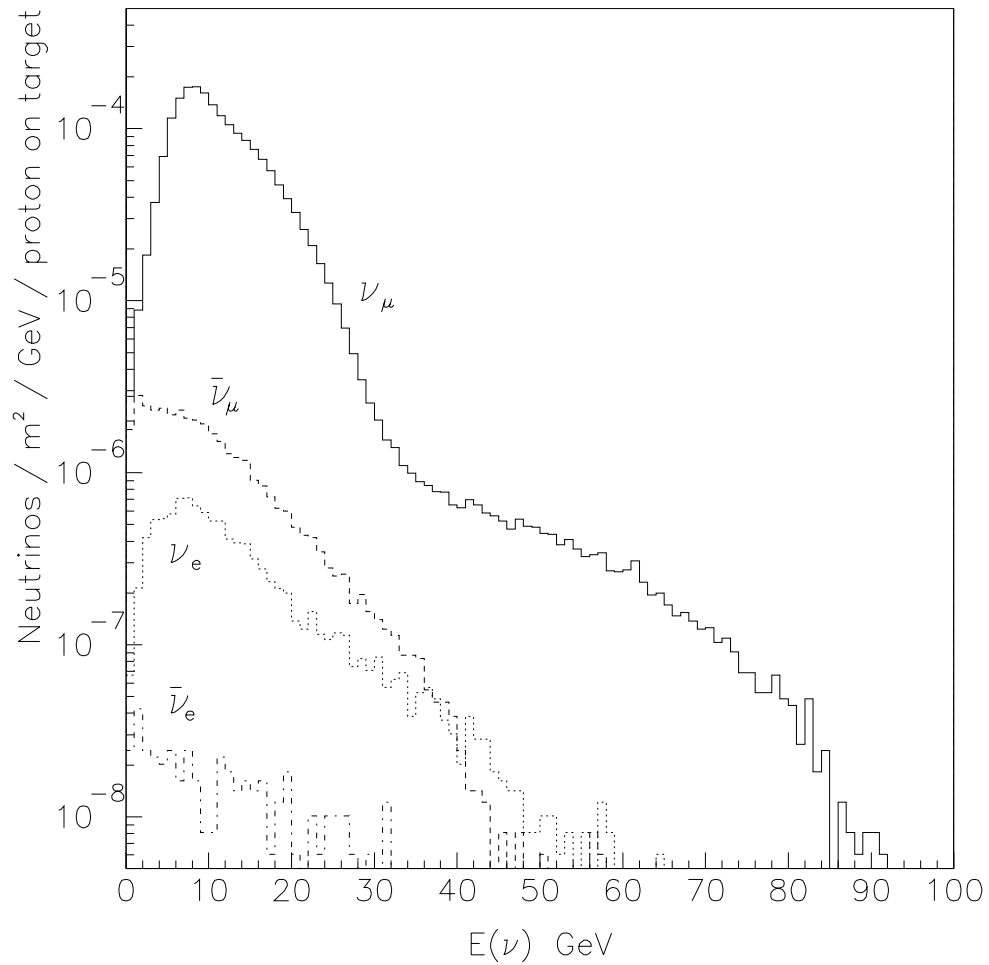


Figure 3.16: Energy spectrum of the flux for each neutrino type, averaged over the 1.4m by 1.8m face of the COSMOS detector, (250 m after the end of the decay pipe).

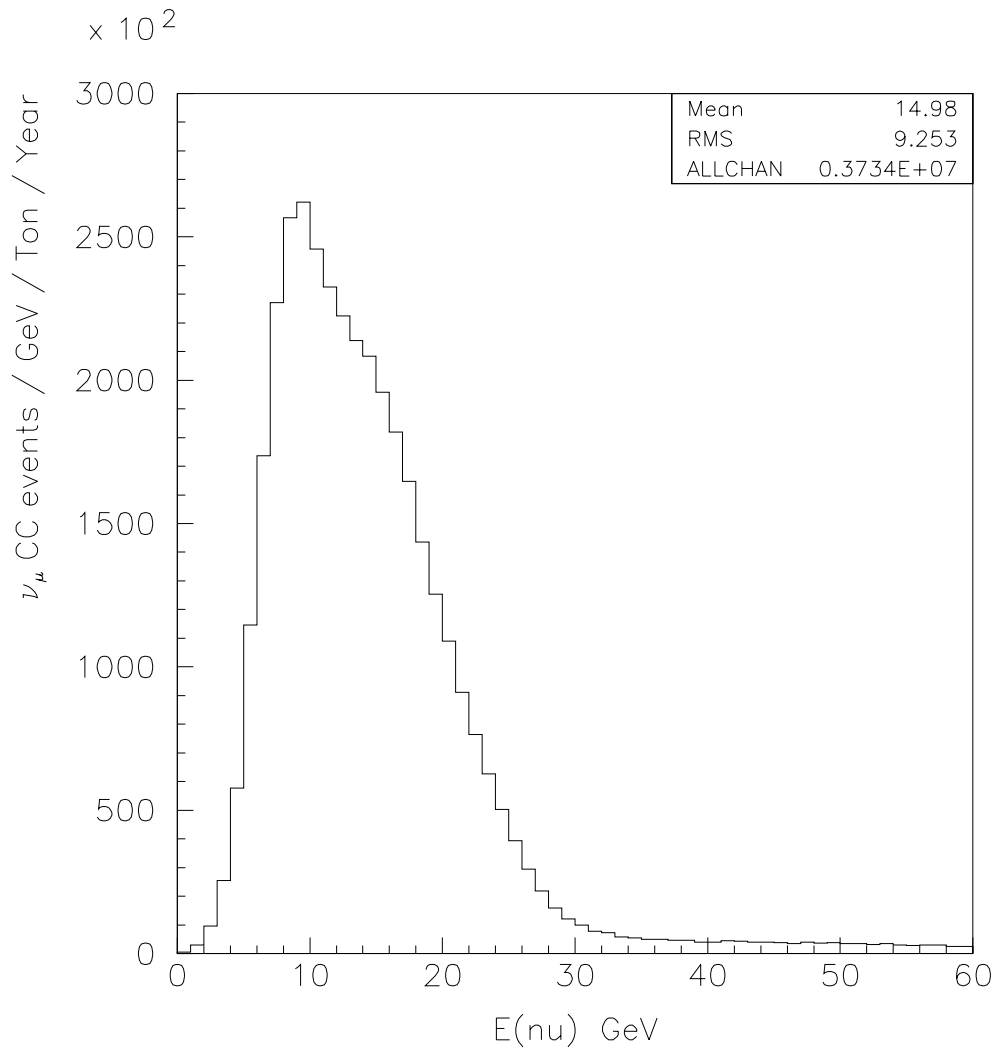


Figure 3.17: Energy spectrum of ν_μ charged current interactions averaged over the 1.4m by 1.8m face of the COSMOS detector, (250 m after the end of the decay pipe).

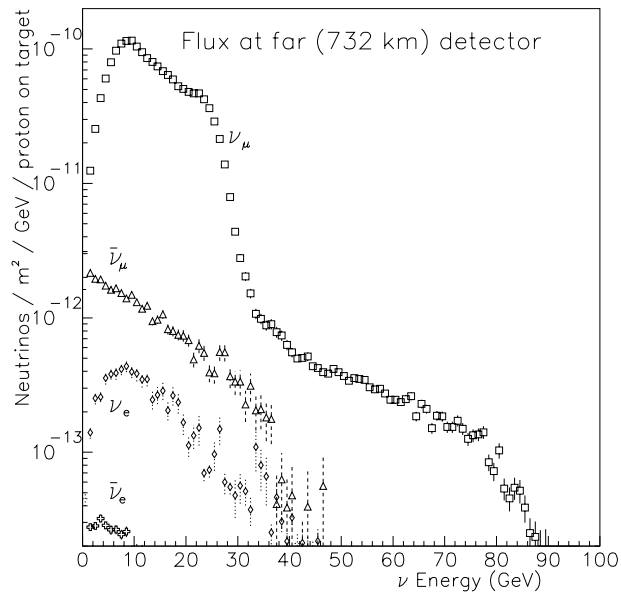
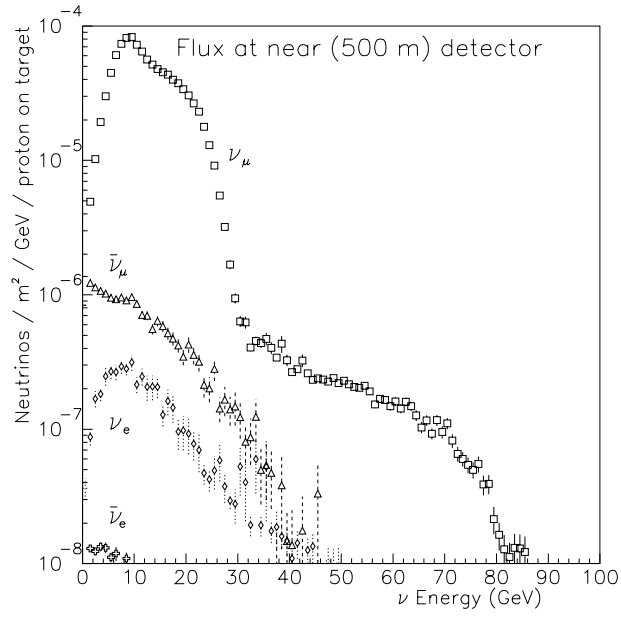


Figure 3.18: ν flux at the center of the MINOS near detector (500 m after the end of the decay pipe), and at the MINOS far detector.

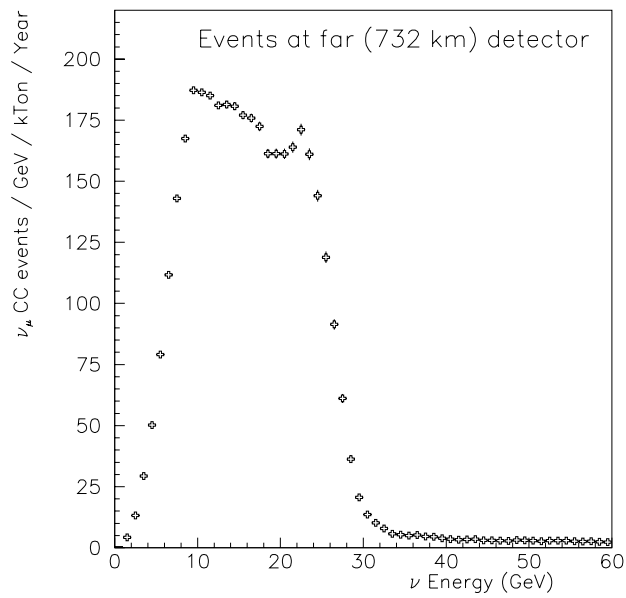
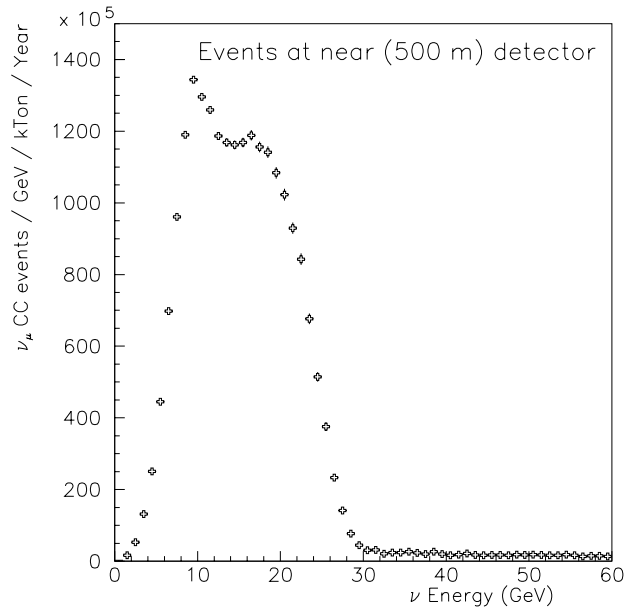


Figure 3.19: Energy spectrum of ν_μ charged current interactions at the center of the MINOS near detector (500 m after the end of the decay pipe), and at the MINOS far detector.

those hadrons produced in the target. Scraping effects (particles from interactions elsewhere than the target) are seen to be small. This is partly because of strong collimation before the decay pipe, and partly because particles from, e.g., interactions in the decay pipe walls, are lower in energy and are not focused toward the detectors. Because the rate from scraping is so small, uncertainty in this rate will not be a significant source of systematic error.

The experimental systematic errors can be studied by varying the following over reasonable limits to determine how the oscillation test results are affected:

- Hadron production spectrum,
- Beam line alignment, including magnetic field variations,
- Secondary interactions in horns, tunnel walls,
- Neutrino cross section,
- Neutrino event generation,
- Detector response, acceptance,
- Reconstruction and identification cuts.

Other effects, such as hadron decay kinematics, also contribute to, e.g., near/far differences but are exactly calculable. The uncertainties in hadron production, beam alignment, and secondary interactions are the province of the beam simulations, and are discussed in the following sections.

Source of Events in Far Detector (compared to target pion $\text{Nu}(\mu)$)

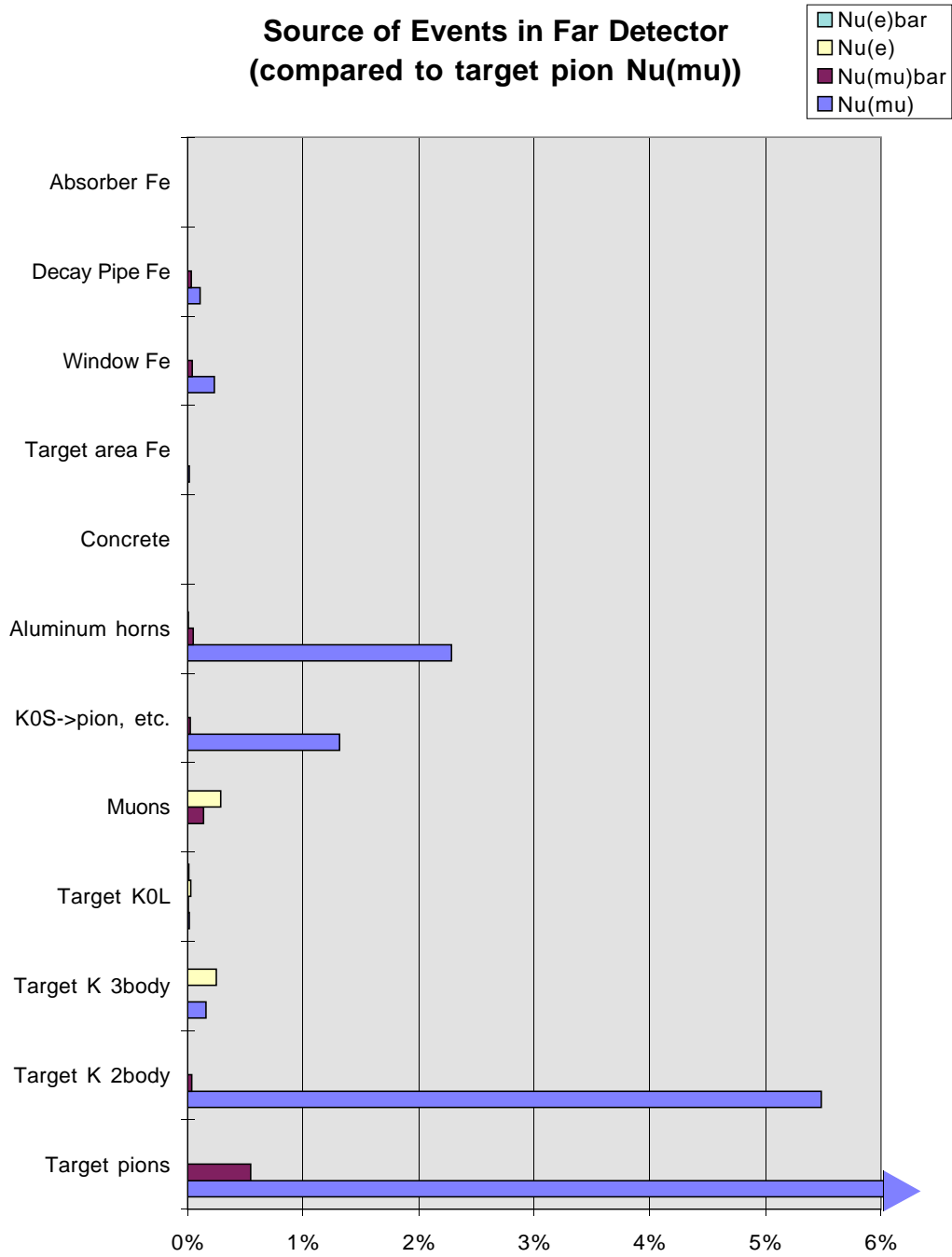


Figure 3.20: The sources of each neutrino type, weighted by the charged current event rate in the MINOS far detector. The rates are normalized by setting the event rate for ν_{μ}^{CC} from π^{\pm} produced in the target to 100%.

3.3.3 Alignment Requirements

Misalignments and operating parameter variations of the elements of the NuMI wide band neutrino beam affect the neutrino energy spectra at the near (on Fermilab site) and far (at the Soudan mine in Minnesota) detectors. The accuracy of the MINOS neutrino energy spectrum oscillation test is expected to be degraded unless the muon neutrino flux energy spectrum in the far detector, assuming no oscillations, is known to 2% for each one GeV bin in the range 1 to 30 GeV.

The Monte Carlo program PBEAM[15] (see Appendix B), written to calculate the neutrino beam spectrum for the COSMOS experiment, was used after making modifications to obtain adequate statistical accuracy for the MINOS far detector and to increase efficiency[16]. This program generates individual mesons in the target, then propagates them through the focussing horns and the decay pipe until they are lost or decay yielding a neutrino. The probabilities of a neutrino from this decay going through the MINOS near and far detectors are calculated separately and added to the corresponding neutrino energy spectra as weights. For a two hour run on a DEC Alpha (3000 Model 400), the statistical error on each 1 GeV neutrino energy bin between 4 and 80 GeV is about 0.5%.

A PBEAM run was executed varying a single parameter each time. As an example, the charged current ν_μ energy spectra were calculated for the case where both the upstream and downstream ends of the first focussing horn were offset 4 mm in the same direction transverse to the beam axis. Since it is difficult to make quantitative assessments directly from the flux spectra, the offset flux is divided by the reference flux (i.e., that for the standard parameter set) for each one GeV neutrino energy interval. The fractional change (quotient) is given in Figure 3.21a for the far detector. A dashed line has been drawn for a flux ratio of 1.0. Shifting horn 1 by 4 mm in the x direction has made a -13.0% change in the neutrino flux at 30 GeV at the far detector. Figure 3.21b shows the effect in the flux at the center of the near detector, some 1300 m from the target. Here, the change is -27.0% at 30 GeV.

It was hoped that the spectra at both the far and near detectors would be equally affected by beam element perturbations, and the ratio of far/near flux would be less sensitive than either spectrum. Therefore, the ratio of these flux ratios, RR , defined by:

$$RR \equiv \frac{Flux_{FAR}(perturbed)/Flux_{FAR}(unperturbed)}{Flux_{NEAR}(perturbed)/Flux_{NEAR}(unperturbed)}$$

is calculated. The RR distribution for the horn 1 shift of 4 mm is shown in figure 3.21c. The peak deviation of +19.6% occurs at 30 GeV. While some

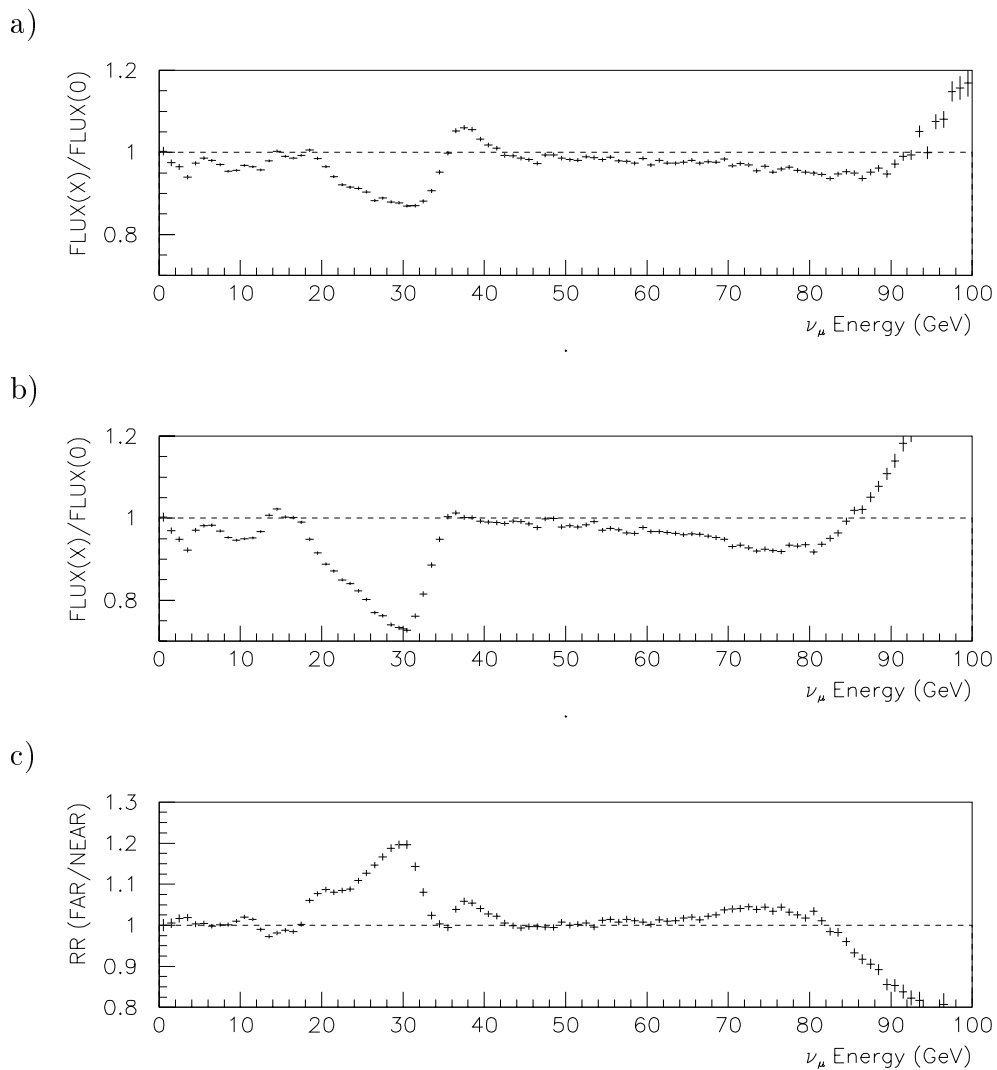
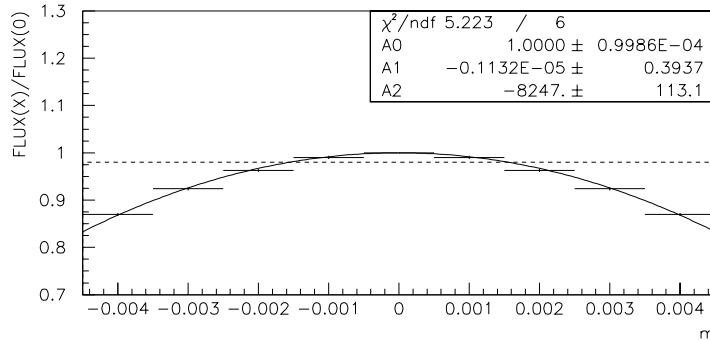


Figure 3.21: The change in neutrino flux at (a) the MINOS far detector, (b) the MINOS near detector, and (c) the far/near ratio, as a function of neutrino energy, induced by a 4 mm transverse shift in the location of horn 1.

energy ranges (e.g., 1–13, 42–69 GeV) do indeed show smaller deviations in RR than in those seen in the FAR spectrum alone (top section figure 3.21a), RR is clearly worse in the sensitive 18–32 GeV range for an x shift of horn 1. These ranges do not change as the size of the x shift is reduced.

a)



b)

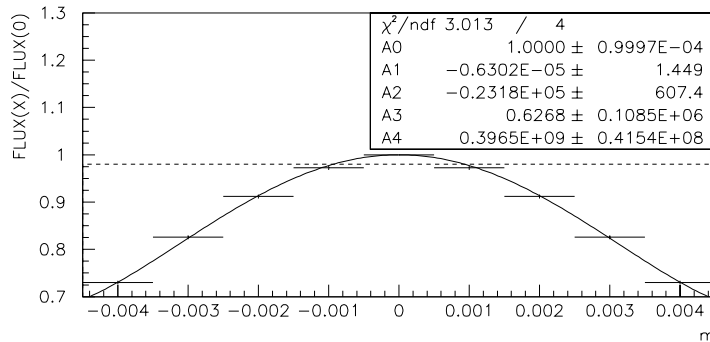


Figure 3.22: Change in far (top) and near (bottom) flux at 30 GeV, as a function of transverse shift of the first horn.

PBEAM results were also obtained for horn 1 x shifts of 1, 2, and 3 mm. The value of the flux ratio at the far detector at 30 GeV is shown in figure 3.22a plotted against the horn 1 x shift in meters. The dashed line is the desired maximum deviation of 2% in the flux ratio. The fit to these data shows the flux ratio deviation is proportional to the square of the horn x shift, and a horn shift of 1.6 mm gives a 2% deviation in the flux ratio. Figure 3.22b shows the analogous fit to the near detector results where an addition term, an x shift to the fourth power, is needed for a good fit. It is found that a horn shift of 0.9 mm gives a 2% deviation in the flux ratio.

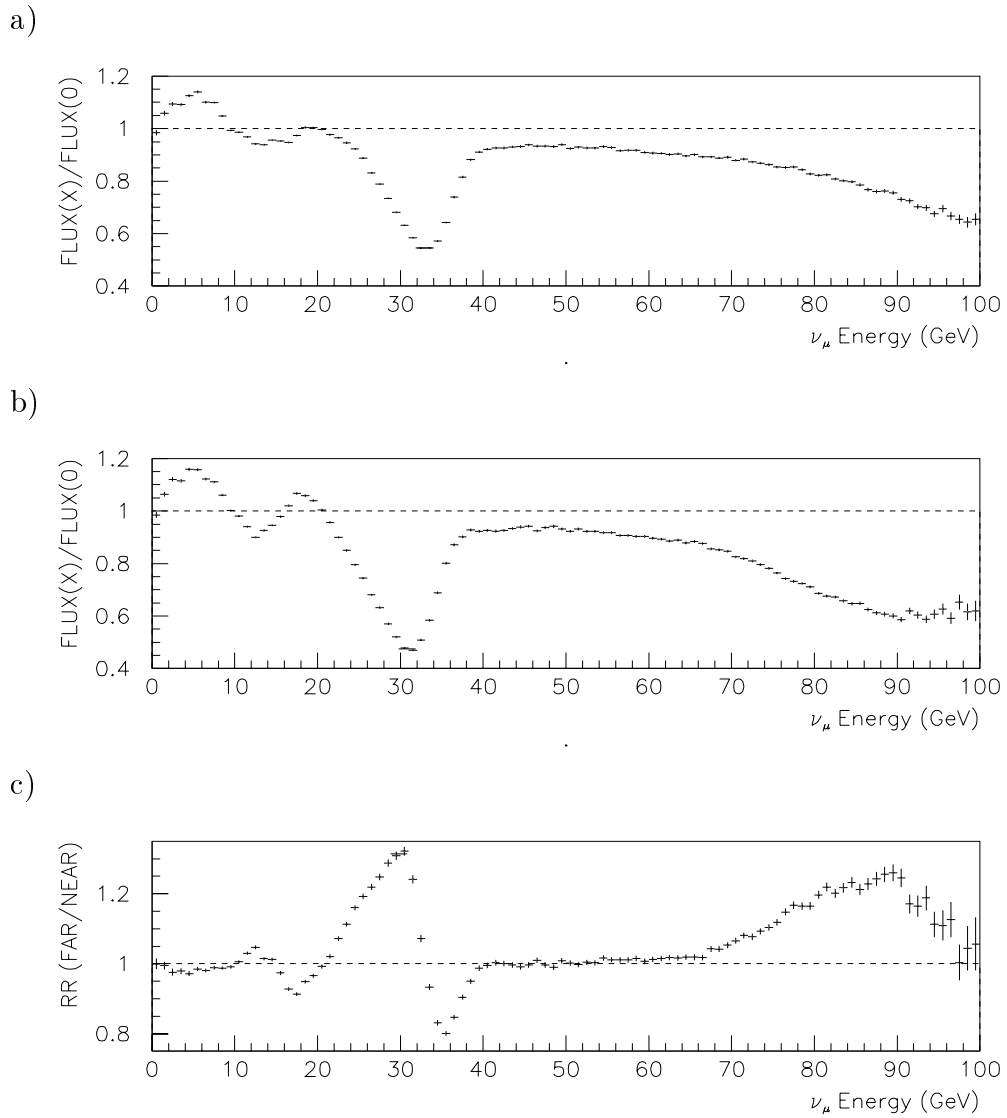


Figure 3.23: Effect of horn magnetic field variations on the flux at (a) the MINOS far detector, (b) the MINOS near detector, and (c) the far/near ratio, as a function of neutrino energy.

The analysis was also performed for a 10% reduction in the magnetic field in all three focussing horns and the results are shown in figure 3.23. The main features in the flux ratios at the far and near detectors are dips just above 30 and 90 GeV. Most neutrinos at the first dip come from the decay of high energy π^+ whereas neutrinos at the second dip come from the decay of high energy K^+ . If the field in all three horns is increased 10%, increases appear at these two energies, indicating the nominal field in the horns is not strong enough to completely bend these highest energy mesons parallel to the beam axis. The results of shifting all horn fields -5%, +5%, and +10% from nominal were also investigated. The effects were fit as described above and the dependence on the field shifts was found to be approximately linear.

In figure 3.23c, RR is shown for a -10% shift of the field in all horns. Except for a small range around 18 GeV, RR is less sensitive to this shift than the flux ratios at the far and near detectors.

Table 3.7 gives the calculated offset that would result in a 2% flux change in the worst 1 GeV neutrino energy bin (in the range 1 to 80 GeV) for a variety of shifts in beamline element parameters. The first line gives the results for a horn 1 x offset. The results of a horn 1 x offset, a 10% reduction in the magnetic field in all three focussing horns, and a shift in the transverse position of the near detector come from fits as described above. Other results were interpolated from a single PBEAM run with a guessed offset, assuming a linear dependence for the shifts in horn field or beam sigma, and a quadratic dependence for translations and rotations. These dependences were found to be rather good approximations in the fits described above.

All but 3 entries in Table 3.7 (horn 1 x , Horn 1,2 Angle) have larger allowed shifts under RR , the FAR/NEAR ratio of ratios, than under the flux ratio at the far detector alone. In particular, over twice as large a shift in the magnetic field in all 3 horns can be tolerated if neutrino oscillations are search for in the FAR/NEAR ratio (ie, in RR) rather than the FAR detector alone.

See [16] for more details of the program and analysis.

Alignment Study Conclusions

- PBEAM, with the addition of weighting events, provides a powerful tool to study the effects of shifts in the elements of the NuMI wide band neutrino beamline.
- Beam+target and horn 1 alignment transverse to the beam direction will need to be done very carefully, although it should be practical unless their positions vary with time or because of beam heating in the target or the 170 kA current through the horn.

- Horn 1 angle, and horn 2 and 3 alignment should be readily achievable
- The horn current will either need to be kept constant to a fraction of a percent during the pulse or the horn currents and number of protons on target will need to be monitored throughout the pulse, for every pulse, and this information used to calculate the muon neutrino energy spectra in the near and far detectors.
- This study indicates that neutrino oscillation searches performed using the FAR/NEAR ratio (RR defined above), rather than the far detector energy spectrum alone, are less sensitive to variations in beamline element parameters.

Element	parameter	FAR	NEAR	RR=FAR/NEAR
Horn 1	Translation	1.6 mm	0.9 mm	1.1 mm
Horn 2	Translation	3.5 mm	3.5 mm	3.9 mm
Horn 3	Translation	5.8 mm	5.0 mm	6.0 mm
Horn 1	Rotation	2.4 mm	1.6 mm	1.8 mm
Horn 2	Rotation	3.9 mm	3.3 mm	3.1 mm
Horn 3	Rotation	5.7 mm	6.8 mm	7.3 mm
Beam+Target	Upstream Tr.	0.79 mm	0.67 mm	0.93 mm
Beam+Target	Translation	1.15 mm	0.85 mm	1.20 mm
Beam+Target	Rotation	0.65 mm	0.61 mm	0.90 mm
Far Detector	Translation	71 m	-	-
Near Detector	Translation	-	0.11 m	-
Horn 123	Field	0.39 %	0.31 %	0.84 %
Horn 1	Field	0.96 %	0.82 %	1.47 %
Horn 2	Field	1.48 %	1.22 %	3.10 %
Horn 3	Field	1.19 %	1.01 %	2.30 %
Beam	Sigma	19 %	21 %	34 %

Parameters:

x	Shift upstream (US) and downstream (DS) ends in the same direction transverse to the neutrino beam axis
Angle	Shift US and DS ends in opposite directions
Upstr	Shift US end only
Field	Horn magnetic field (proportional to horn current)
Sigma	Primary proton beam width. For this study, $e^{(-0.5(r/\sigma)^2)}$ is the fraction of protons at radii $> r$

Table 3.7: The change from nominal of beamline element parameters which will cause a 2% flux change in the most affected one GeV neutrino energy interval between 1 and 80 GeV. These data are for one parameter shift at a time, i.e. it is assumed that all other beamline elements are at their nominal values. Calculated for the NEAR detector at $z=1300$ meters.

3.3.4 Hadron Production Model Uncertainty

As exemplified by Figure 3.14, the hadronic production as a function of p and p_t is not well measured at these energies. Further, this involved an extrapolation from the hydrogen target measurements to a thick carbon target and an extrapolation in beam energy. Figure 3.24 illustrates the effect through showing a comparison between the results of a Monte Carlo (NUADA) using a hadron production based on a fit by Malensek[17] to data taken by Atherton *et al.*[20] and a Monte Carlo (GNUMI) using the GEANT/FLUKA hadron production model.

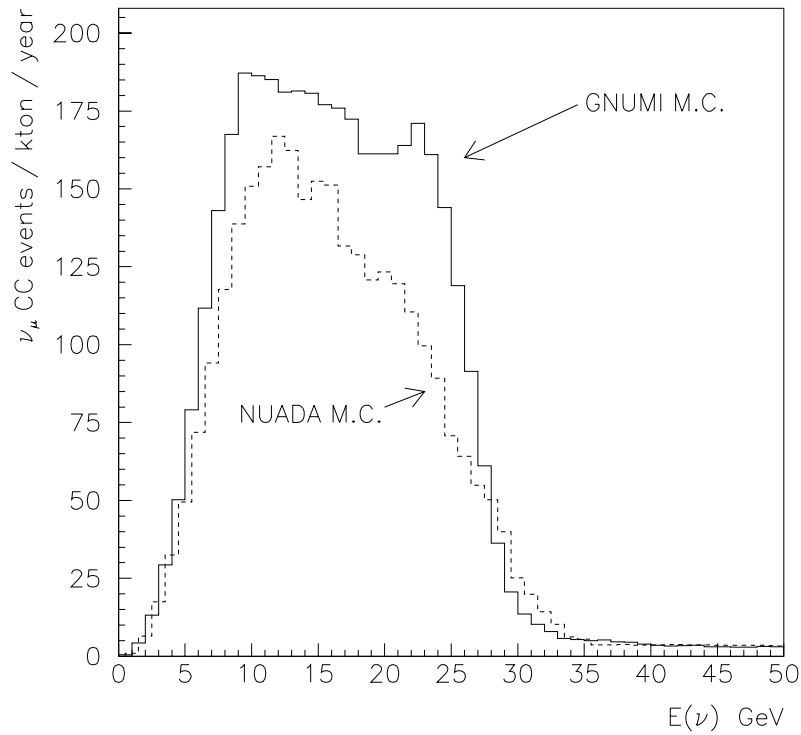


Figure 3.24: Comparison of the GNUMI and NUADA Monte Carlo programs' predictions of the ν_μ^{CC} event rate in the MINOS far detector.

To first order, variations in the longitudinal momentum spectrum of the hadrons will be mirrored in both the near and the far detectors, so that it can be factored out in the MINOS oscillation tests. An estimate of the systematic error in the Monte Carlo extrapolation from the near detector to the far detector can then be made by studying the result of variations of the p_t spectrum. Figure 3.25

shows a variation of the GEANT/FLUKA model which changes $\langle p_t \rangle$ from 0.37 GeV to 0.55 GeV. This is more than adequate to cover the $\langle p_t \rangle$ range found in other models of hadron production (e.g., WANG[18] has $\langle p_t \rangle = 0.42$ GeV, the CKP model[19] has $\langle p_t \rangle = 0.44$ GeV, and the Malensek model[17] has $\langle p_t \rangle = 0.50$ GeV). Figure 3.26 shows the relative changes in the near and far spectra as such a variation is made, as well as when the p_t is made (unphysically) narrower. By taking a $\langle p_t \rangle$ in the center of the range of models, and using the distributions in Figure 3.25 as limits, one obtains the systematic error estimates shown in Figure 3.27.

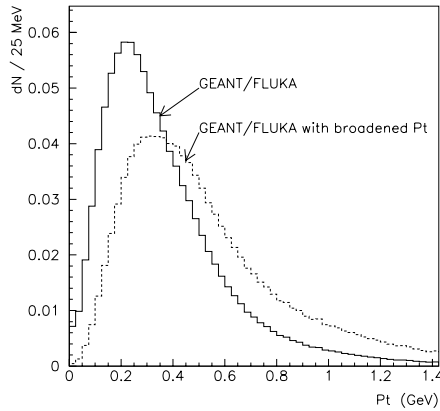


Figure 3.25: Pion p_t production distributions propagated through the GNUMI Monte Carlo to study hadronic production systematics.

This uncertainty from the hadronic production model would be the limiting systematic error for the ν_μ CC Total Energy oscillation test unless one or both of the following options are taken:

- Measure the hadronic production spectrum from a carbon target with 120 GeV protons. This involves a separate fixed target experiment. The production rates in p and p_t would need to be measured to a few percent.
- Implement continuous focusing in the decay pipe, as described in the next section.

3.3.5 Hadronic Hose Option

There are three basic effects that cause differences in the ν energy spectrum in the MINOS near and far detectors:

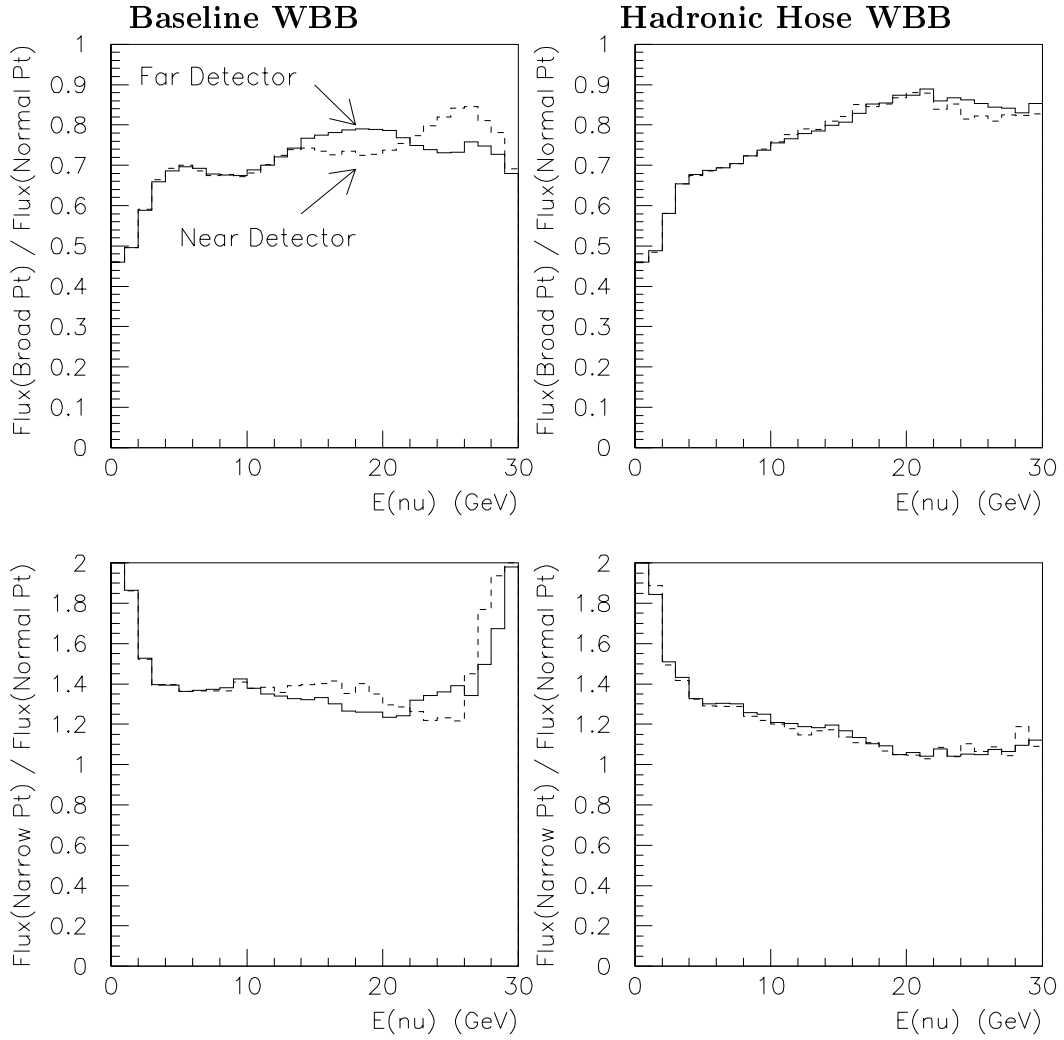


Figure 3.26: Comparison of Baseline WBB and Hadronic Hose WBB under variations of the P_t spectrum of the hadronic production model. The flux with the modified P_t spectrum relative to the flux with the normal P_t spectrum is plotted in each case for both the far detector (solid) and near detector (dashed).

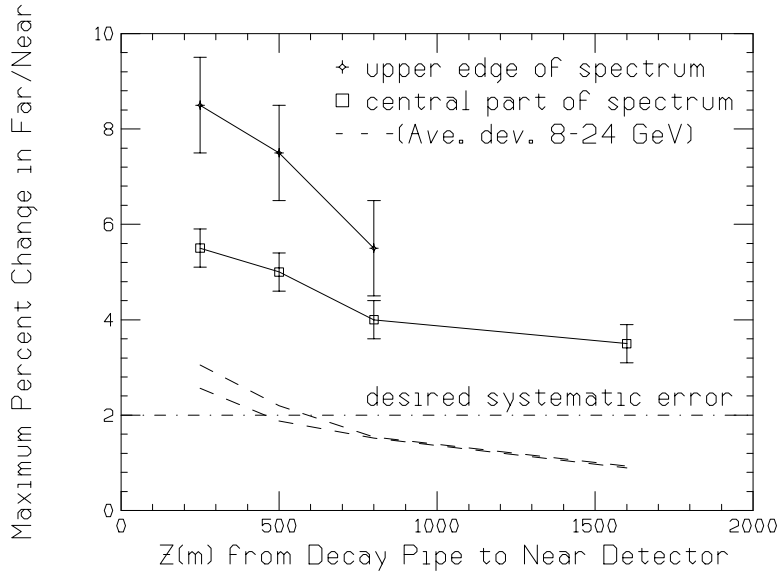


Figure 3.27: Estimate on the uncertainty in the relative neutrino spectra (Far/Near) due to uncertainty in the P_t distribution of the hadron production model, as a function of the location of the Near Detector.

- Since the mean distance a pion travels before decaying is given by $\gamma c\tau$, high energy pions live longer and the source of high energy decays is thus closer to the near detector on average than the source of low energy pions. This effect is exactly calculable.
- Pions which are better focused can travel farther down the decay pipe, and produce a source closer to the near detector, than poorly focused pions, which are absorbed in the decay pipe walls. This effect on the source distance depends on focusing misalignments and hadronic production p_t .
- For pions at larger radius in the decay pipe, the angle of decay to the center of the near detector is larger than the angle of decay to the far detector. Thus the energy of the neutrinos in the far detector tends to be higher than the energy in the near detector. This effect is sensitive to the radius in the decay pipe of the pions when they decay, and thus to the focusing and hadronic production p_t .

An idea to mitigate the last two of these effects is to use continuous central focusing in the decay pipe (after the horn focusing system) by trapping pions in oscillating trajectories (Figure 3.28). A current of order 1 kA in a wire down the center of the decay pipe produces sufficient magnetic field to trap most pions, keeping them away from the decay pipe walls. The oscillating trajectories even

out the decay angular distributions to the near and far detectors. The spectra produced in the near and far detectors are then much more similar (Figure 3.29). More importantly, systematic variations tend to have more similar effects in the near and far detectors, as seen in Figure 3.26. This cancellation of the systematic errors then allows the prediction of the spectrum in the far detector from the spectrum measured in the near detector to better than 2%.

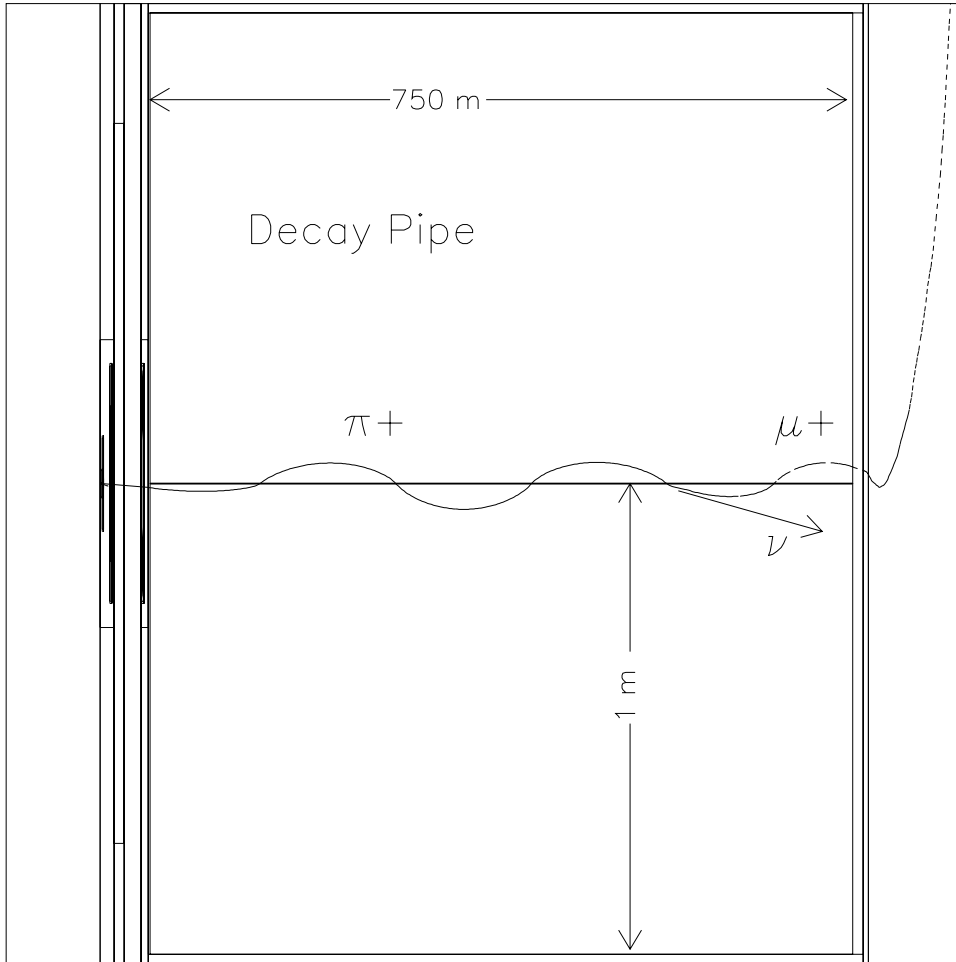


Figure 3.28: A **GNuMI** sample event display showing the trajectory of a π^+ which orbits the hadronic hose wire, and decays to $\mu^+\nu_\mu$.

The theory of this continuous central focusing (which we have named the “Hadronic Hose”) is described in Reference [21]. Note that trajectories are nearly flat, not helical, so that the direction of travel of the pions sweeps nearly through the center of the near detector. The wire carrying the current must then be rather small (of order 1 mm radius), so as not to absorb too many of

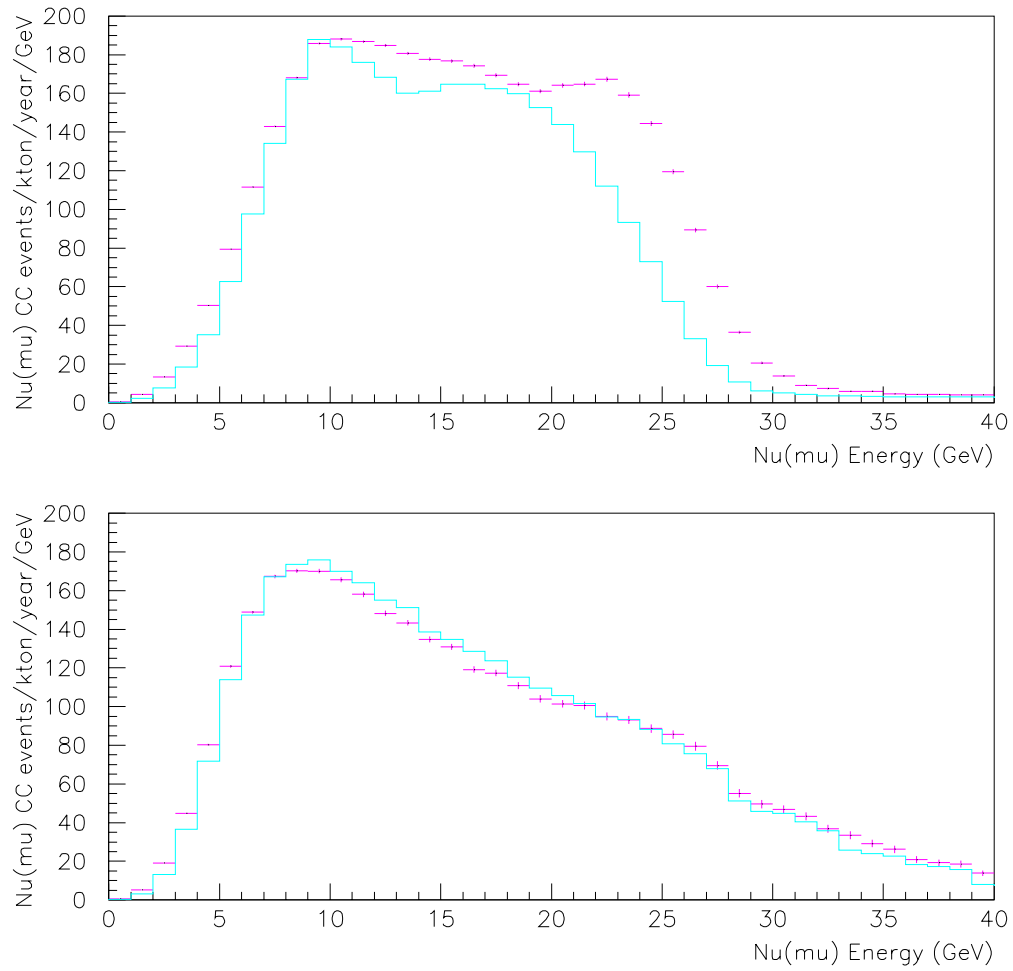


Figure 3.29: The far spectrum (points) and the near spectrum multiplied by 1.4×10^{-6} (histogram) for the three horn wide band beam design (top), and the same with the addition of the hadronic hose (bottom). For the hadronic hose spectra, the difference between far and near in the few GeV range is due to the effect of the pion lifetime.

the pions. The technical challenge is then to radiate enough heat from the wire, while still carrying sufficient current. This is accomplished by only pulsing the current during the beam spill, and anodizing the wire to improve heat loss by radiation. An R&D program is currently underway to study the problems of creep, vibration, and long term mechanical stability. If this R&D proves out on a timely scale, then the Hadronic Hose is a valuable addition to the beam.

3.3.6 Horn Mechanical Design

The information in this section is abstracted from Reference [22].

Aluminum alloys 7075 and 6061, which are candidates for the horn material, have the properties given in Table 3.8. For the structural analysis, a half-sine-

Alloy	7075	6061
Young's modulus E	72 GPa	69 GPa
density ρ	2700 kg/m ³	2619 kg/m ³
thermal conductivity k , 300K	200 w/m-°C	237 w/m-°C
heat capacity c	896 J/kg-°C	962 J/kg-°C
thermal expansion coefficient α	20.92 $\mu/^\circ\text{C}$	20.92 $\mu/^\circ\text{C}$
electric resistivity σ 68°F	52x10 ⁻⁹ $\Omega\text{-m}$	40x10 ⁻⁹ $\Omega\text{-m}$

Table 3.8: Properties of Aluminum Alloys 7075 and 6061

wave current pulse of $I_{max} = 200kA$ and length $\tau=5.2$ ms with a repetition time of 1.86 s was used. During 5.2 ms, the mechanical disturbance can propagate a distance of $l_m = \tau(E/\rho)^{1/2} = 27$ m, and the thermal disturbance can propagate a distance of $l_t = (\tau k/\rho c)^{1/2} = 0.66$ mm. The characteristic length, l , of the horns is 2 m. Thus $l_m \gg l \gg l_t$, so the current pulse is mechanically a very slow load and thermally a very rapid load for the horns. Therefore, we can treat the mechanical load as static, and thermal heat as instantaneous. The horns will be cooled by water spraying on the inner conductor.

Magnetic Load The magnetic force is calculated by $J \times B$. Assuming a uniform distribution of current density over the cross section,

$$p = \frac{\mu_0 I_0^2}{2(2\pi R)^2} \left(1 - \frac{t}{6R}\right) \approx \frac{2000}{\pi R^2}$$

where R is the radius in meters of the horn inner conductor, t the thickness, the current I_o is in Amps, and the result p is in Pa (i.e. N/m²). For our case $t/(6R) < 5\%$, so that that term has been neglected.

Thermal Load The heat energy per pulse per unit volume is

$$e = \frac{\sigma}{A^2} \int_0^{t=\pi/\omega} I^2 dt = \frac{\pi \sigma I_0^2}{2\omega A^2}$$

and the temperature rise in °C is

$$\Delta T = \frac{e}{\rho c} = \frac{\sigma I_0^2}{8\pi\omega\rho c R^2 t^2} = \frac{57 \times 10^{-9}}{t^2 R^2}$$

The units of R and t are meters. Putting in the time between pulses of $\tau'=1.86$ s and taking an effective film coefficient of convection heat transfer $h=3500$ w/m²-°C, the temperature rise averaged over time is

$$T - T_0 = \frac{\sigma I_0^2}{8\pi\omega\tau' R^2 t h} = \frac{21 \times 10^{-6}}{t R^2}$$

The maximum temperature occurs at the neck where R is minimum. Assuming $R = 0.01$ m and $t = 0.003$ m, we have $\Delta T_{max} = 63^\circ$ C, $(T - T_0)_{ave} = 70^\circ$ C. The maximum instantaneous temperature is $(T - T_0)_{peak} \approx 130^\circ$ C.

Preload The thermal load tends to extend the horn, and some pretension would reduce the thermal stress. The stretch δl for a preload of F is

$$\delta l = \int_0^{x=l} \frac{F}{EA} dx = \frac{F/E}{2\pi t(r_1 - r_2)} l \log\left(\frac{r_1}{r_2}\right)$$

If we let $F = 2000$ lbs = 8896 N then $\delta l_1 = 0.894$ mm, $\delta l_2 = 0.370$ mm, and $\delta l_3 = 0.226$ mm. The maximum stress is $F/2 \pi r_2 = 70.79$ MPa = 10.27 ksi when $r_2 = 1$ cm. In practice, the preload is determined by the stretch, and we set $\delta l_1 = 1.0$ mm, $\delta l_2 = 0.5$ mm, and $\delta l_3 = 0.3$ mm.

FEA Analysis Finite Element Analysis has been used to calculate horn stresses. Horns are modelled by axi-symmetric shell elements. The r_1 end is fixed, and the r_2 end has an axial displacement to apply the preload. The magnetic load is applied as pressure and the thermal load is applied as temperature. Three load cases are analyzed:

- at the beginning of the pulse, when magnetic load is zero and temperature is minimum;
- at the middle of the pulse, when the magnetic load is maximum and the temperature is at the middle;
- at the end of the pulse, when the magnetic load is zero and the temperature is at maximum.

The difference of the hoop stress before and after the pulse is very small, and indicates that the hoop stress is caused by the magnetic pressure. The maximum hoop stress occurs at $r_2 = 1$ cm for horn 1, and is 2440 N/cm^2 , or 3538 psi. Hence the stress cycle caused by magnetic load is from 0 to 3538 psi (compressive); not very large.

On the other hand, the meridional stress is caused by thermal expansion, which changes as temperature changes. Again for horn 1, the maximum stress changes from 4220 N/cm^2 (6119 psi) before the pulse to -2090 N/cm^2 (-3031 psi), the range of stress is 6310 N/cm^2 (9150 psi). For horns 2 and 3, the range is 2250 N/cm^2 (3263 psi) and 620 N/cm^2 (899 psi), respectively.

From the Aluminum Association's *Aluminum Design Manual*, the allowable fatigue stress range can be calculated as $S_{ra} = AN^{-1/m}$, with $A = 96.5$ ksi and $m = 6.85$. N is the number of loading cycles. The fatigue limit is 12.5 ksi. If we assume $N = 10^7$, we have $S_{ra} = 9.18$ ksi. The stress range for horn 1 is 6310 N/cm^2 (9150 psi), which is below the fatigue limit, but has no safety factor. The stress in the other two horns is far below the fatigue limit and therefore is not a problem.

Some factors such as the increased electrical resistance of the horn at higher temperatures have been neglected in the above calculation, but we believe we can draw the following conclusions:

- The stresses in horns 2 and 3 are quite small and therefore there is no problem in maintaining structural integrity. Furthermore, less preload than what is given here will be acceptable.
- Horn 1 is on the boundary of the allowable fatigue stress range. Some safety factor is provided by the use of a current pulse in this calculation which is 10% to 15% larger than desired. Nevertheless, the design needs to be carefully engineered, and a somewhat larger wall thickness may be required.
- We note that, although the cooling efficiency may influence the overall stress distribution of the horns, the stress range will remain the same since it depends only on the energy per current pulse.

In conclusion, the structural integrity requirement of the horns can be met by a suitable choice of wall thickness, preload, and an optimized current pulse.

3.3.7 Horn Electrical Design

The power supply proposed for powering the three series-connected focusing horns for NuMI is of the direct coupled design. Energy is stored in a capacitor bank and switched via a parallel array of SCR switches into the horn load. A parallel strip transmission line is used to connect the power supply to the focusing horns. The neutrino horns require a train of 170 kA ($\pm 5\%$) pulses with a duration of 1 ms and a repetition period of 1.9 s. As a safety margin the supply will be designed to operate up to 200 kA. This results in a system load current of 7400 A (rms).

Circuit requirements The circuit used is a damped LC discharge circuit as shown in Figure 3.30 which will achieve the peak current when the SCR switch releases stored energy from the capacitor bank to the horns via the stripline. The estimated circuit parameters are listed in Table 3.9

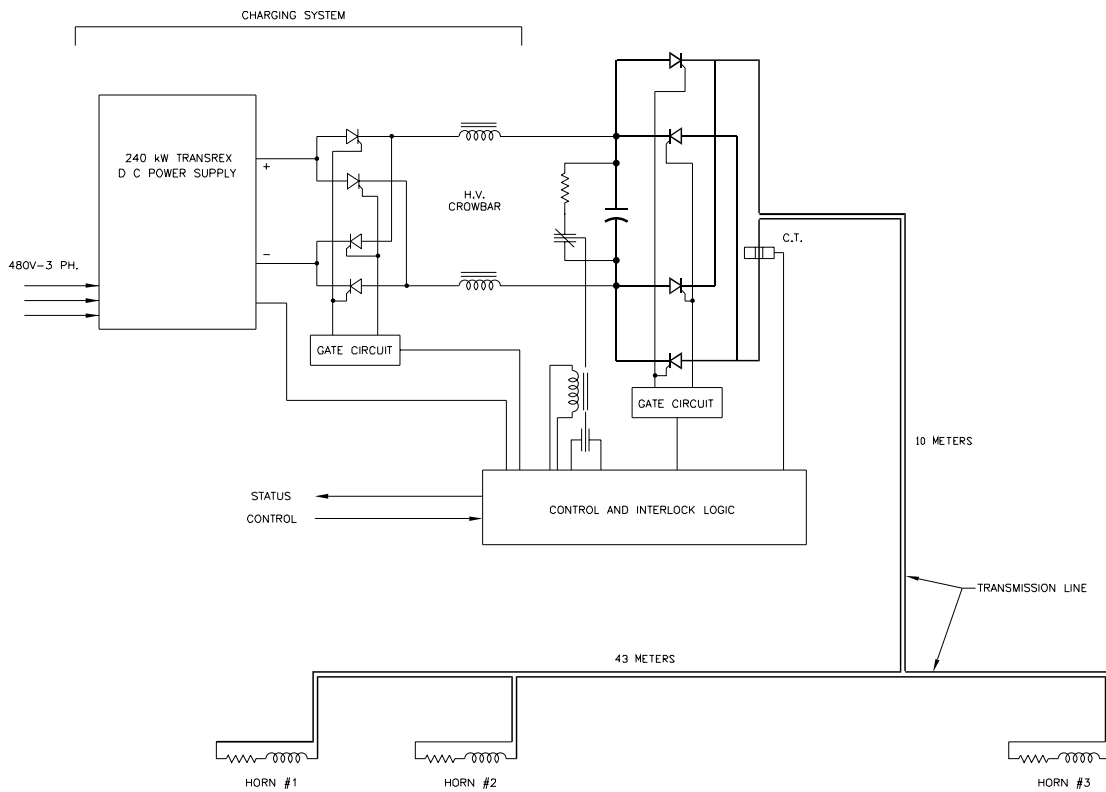


Figure 3.30: Basic horn power supply circuit with charge recovery.

Element	L (μH)	R ($\text{m}\Omega$)	P (kW)
Horn 1	0.516	0.456	25
Horn 2	0.575	0.488	10
Horn 3	0.351	0.115	6
Transmission line:			
• Supply to beamline (10 m)	0.197	0.104	6
• Between horns (43 m)	0.839	0.443	24
Power supply to capacitor bank plus connections*	1.000	0.030	2
TOTAL	3.478	1.336	73

Table 3.9: The neutrino horn circuit inductance L , resistance R , and power P . (* estimate)

Charging system The capacitor bank can be recharged by a standard Fermilab 240 kW power supply. The calculated power consumption during operation of the horn is 155 kW. The required voltage for operation is 765 volts.

To avoid creating transients on the power line, a 1 mH inductance will be inserted between the charging power supply and the capacitor bank. Four series connected 0.25 mH units rated at 200 A (dc) will be used.

The requirements for the SCR's performing this function are very modest and only a single device at each position will be needed. They need only be rated to conduct 200 A (dc) and have a voltage rating of 2 kV. Devices meeting these requirements are readily available. The polarity of the reversing switch will be set by the control electronics as determined by the polarity of charge on the capacitor bank.

Capacitor bank Based upon the inductance and resistance values provided for the three focusing horns, the capacitance required for the bank is 0.713 farads. This will be made up of an array of individual energy storage capacitors connected in parallel, but separated into a number of cells. The number of capacitors in each cell shall be chosen to limit the amount of stored energy for that cell to a value that can be safely contained within an individual capacitor case without rupture in the event of an internal fault.

Discharge resistors and safety system A safety system will monitor operating parameters of the power supply and safely shut it down if out-of-tolerance

conditions are detected. Parameters to be monitored include; over voltage and over current conditions of the charging supply, over voltage and over current conditions of the capacitor bank, ground fault currents, excessive temperatures, loss of cooling to the power supply or horns, personnel entry, etc. When fault conditions are detected, the charging supply will be turned off and the capacitor bank will be discharged via a redundant arrangement of dump resistors and shorting relays to remove the stored energy. The dump resistors shall be rated to absorb the maximum stored energy of the capacitor bank, 209 kJ.

Discharge switch The discharge of stored energy from the capacitor bank to the horns is performed by SCR's. Each switching element shall consist of a number of SCR's, one per capacitor bank cell, sharing the total load current. The number of SCR's required shall be determined by further investigation of available devices that can meet the requirements of this application.

Current transducers A passive current transformer is the device of choice for monitoring the output current from the supply. This can be done in two possible ways: a single monitor located on the stripline to read the total current, or a number of smaller monitors, one associated with each of the parallel SCR's, having their outputs summed together to read total current. The latter method has the advantage of allowing the monitoring of the performance of each capacitor bank cell/SCR combination.

Transmission line A transmission line consisting of two parallel plates will be necessary to connect the output of the power supply to the horns. Power losses in the transmission line are roughly equivalent to that of the three horns combined. It will have to be constructed to carry a current of 7400 A (rms) with due consideration given to dissipating the resultant heat. Limiting the temperature rise of the stripline to 10° C would require 11 gpm of water flow. In addition, it must have minimal inductance and resistance, allow for thermal expansion and contraction at the horn connections, have insulation tolerant of the high radiation flux, and permit rapid but reliable connection/disconnection at each horn terminal. Consideration needs to be given to the choice of material for the line, copper or aluminum, if induced radioactivity is a concern.

Water cooling The SCR's will require water cooling at a flow rate of 4 gpm. Water cooling of the safety dump resistor may be desirable. It is not known at this time if the capacitors will be of water cooled construction.

3.4 Decay Pipe

Length and Radius The ultimate choice of decay pipe length and radius will be set by neutrino economics, i.e., by optimizing the yield of neutrino events for a fixed total cost of the neutrino beam and the MINOS far and near detectors. One of the major cost drivers for the beamline is the shielding of the decay tunnel (see section 3.9.4 for details of the groundwater activation considerations) and so the question reduces to the relative cost savings of shrinking the decay pipe versus the consequent decrease in neutrino yield for a fixed detector mass.

It was found for the old two horn design that, not surprisingly, the event rate at Soudan increased with increasing decay pipe radius and increasing decay pipe length[1]. For a 300 m long decay pipe, the event rate plateaued for a decay pipe radius of around 75 cm whereas for a 1 km long decay pipe the event rate does not flatten out until the beam pipe radius reaches about 2 to 2.5 m. A maximum decay region length of 800 m (it is 50 m from the end of the target to the entrance of the decay pipe) is set by the diminishing event rate with increased decay pipe length and the required distance from neutrino creation to detection point in COSMOS.

The decay pipe length and radius studies have been updated for the three horn design as implemented in GNUMI. Part of the motivation for using the slower, GEANT based GNUMI program is that interactions of particles with the decay pipe walls are more fully simulated (see Appendix B for a discussion of the relative merits of the different simulation packages). The number of events in the far and near detectors due to the decays of particles which originated from interactions in the beam pipe walls (“particle scraping”) was found to be small, as illustrated in Figure 3.31. Only for neutrinos with energies below ~ 5 GeV was decay pipe “scraping” an appreciable (greater than 0.5%) source of events. The ν_μ charged current event rates as a function of energy for decay pipes of 1 m, 75 cm, and 50 cm radius are shown in Figure 3.32. The ratio of ν_μ charged current event rates for various decay pipe radii to that for a 1 m radius decay pipe are shown in Figure 3.33. The effects on the total event rates of varying the radius and length of the decay pipe are given in Tables 3.10 and 3.11. These numbers do not change if the event rates are considered for neutrinos only up to 35 GeV.

Vacuum and Stray Magnetic Fields The sheer length of the decay pipe introduces several considerations. The decay pipe needs to be marginally evacuated since air in the decay pipe would introduce about 1 interaction length of material and is thus unacceptable. Both absorption and multiple scattering are negligible for a vacuum of 1 Torr or less. Standard mechanical pumps with blowers will easily provide a vacuum of 10^{-2} Torr.

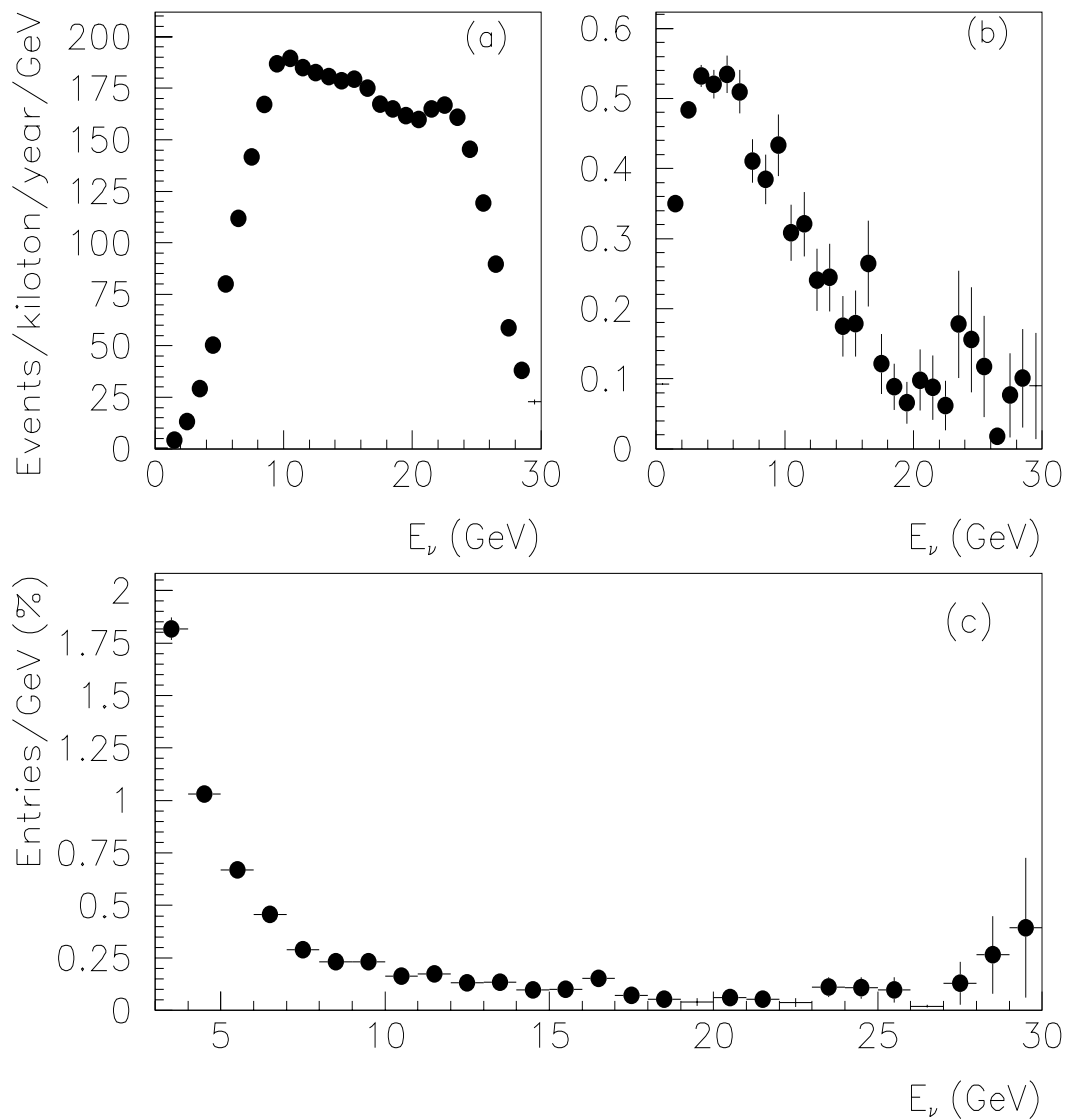


Figure 3.31: The ν_μ charged current event distribution at Soudan for a 750 m long, 1 m in radius decay pipe for (a) all sources, and (b) the decays of particles which originated from interactions (“scraping”) in the decay pipe walls. The fraction of events (in %) due to “scraping” i.e, the ratio of (b) to (a), is given in (c).

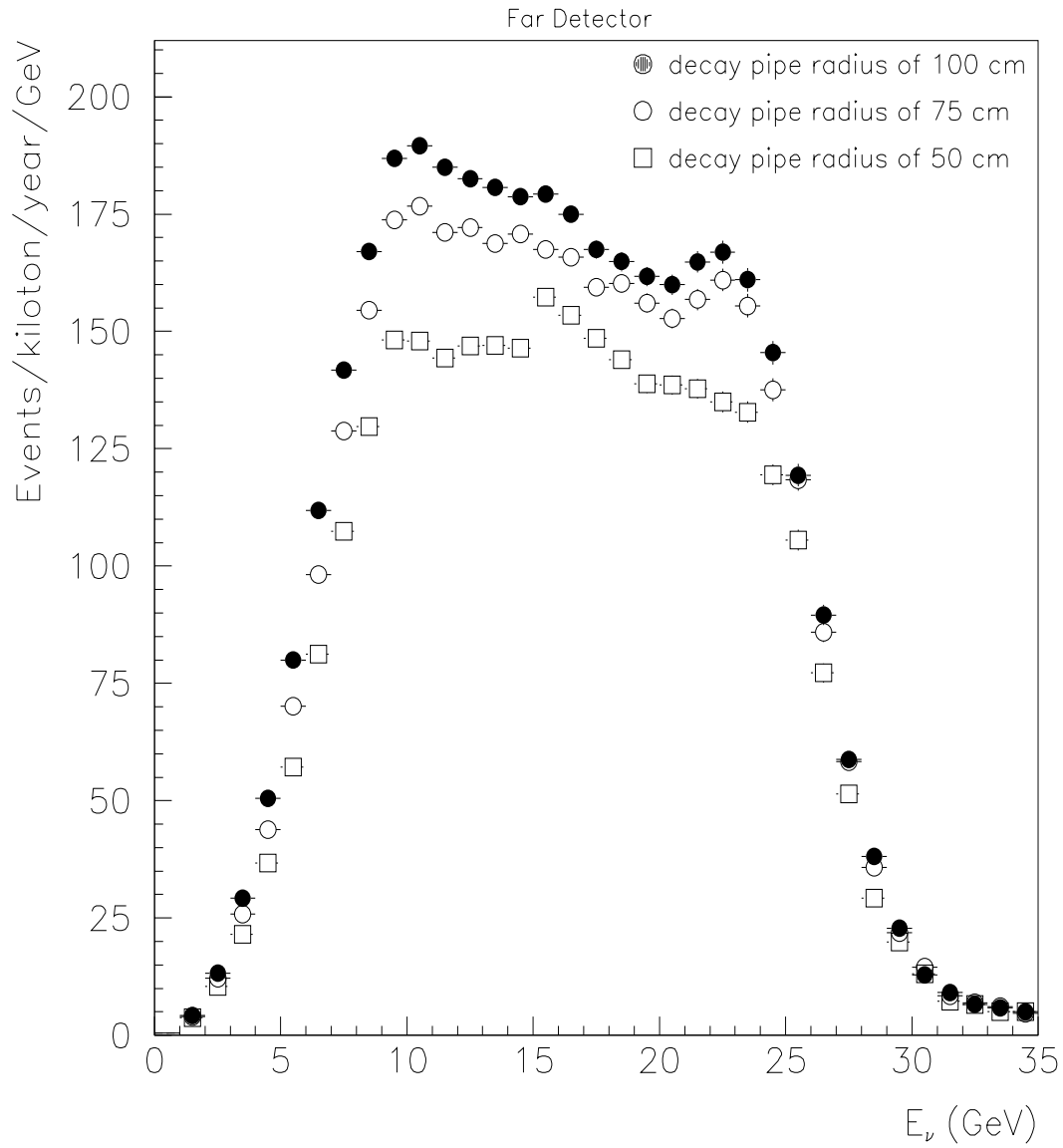


Figure 3.32: The ν_μ charged current event distributions at Soudan for three decay pipe radii. The decay pipe is 750 m long.

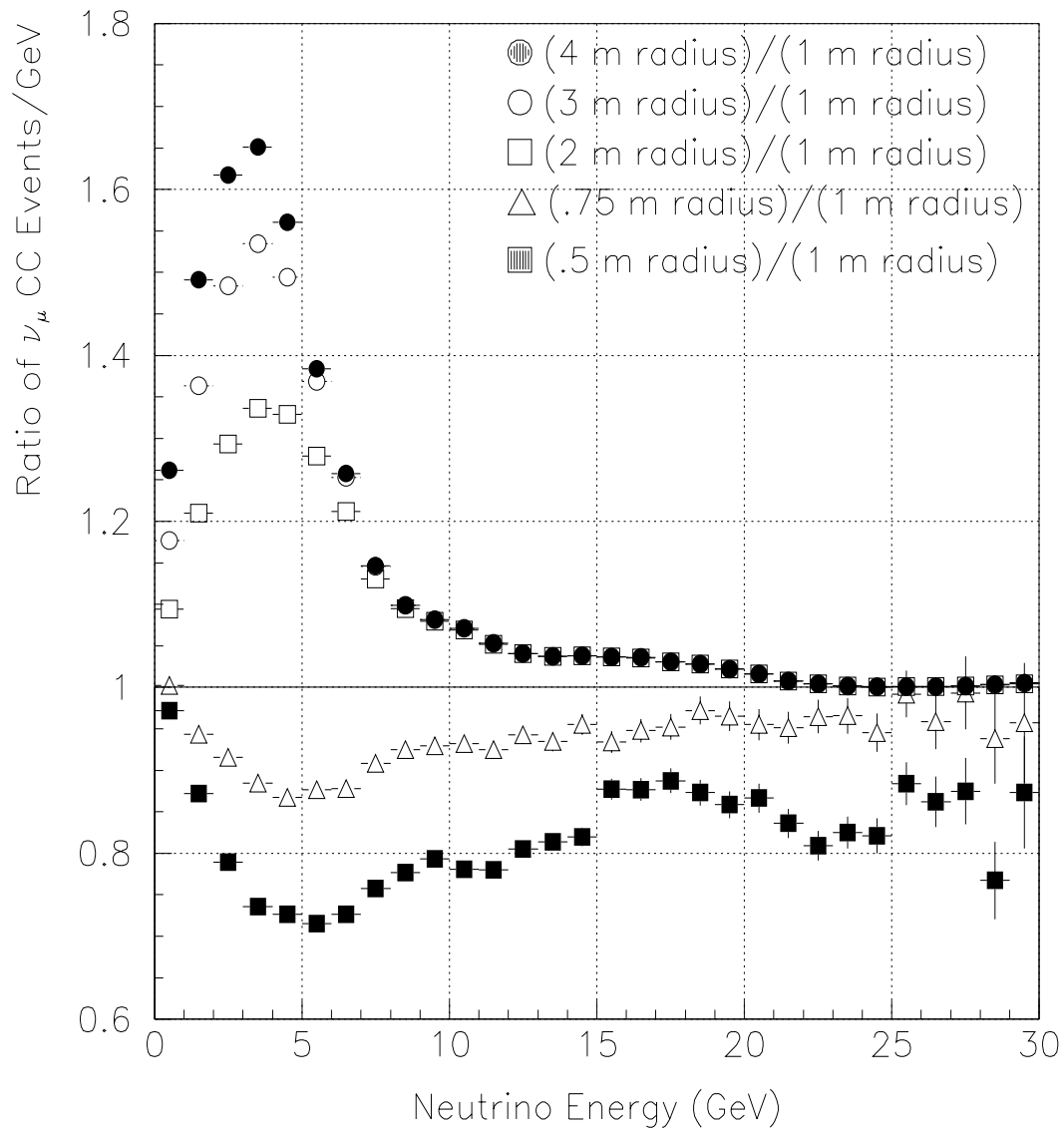


Figure 3.33: The ratio of ν_μ charged current event distributions at Soudan for decay pipe radii of 4 m, 3 m, 2 m, .75 m, and .5 m to the standard 1 m.

There is a potential defocusing of the neutrino beam due to bending of the trajectories of long lived charged hadrons in the long decay pipe by the Earth's magnetic field[25] and by stray magnetic fields from the decay pipe iron. The effect of the Earth's magnetic field was investigated using GNUMI and was found to be negligible on the order of present beam pointing uncertainties[26]. This effect also did not create significant distortions (i.e., on the order of 2%) in the beam spectrum at Soudan. Defocussing due to stray fields in the decay pipe iron have yet to be evaluated using GNUMI. These effects could be mitigated by instrumenting the entire decay pipe as a focussing element (see section 3.3.5) although this has yet to be investigated.

Decay Pipe Radius (m)	R - Near Detector	R - Soudan
4	1.052	1.07
3	1.050	1.06
2	1.043	1.05
.75	.952	.94
.5	.843	.82

Table 3.10: Effect on the ν_μ charged current event rates of varying the decay tunnel radius. R is the ratio of the number of CC events for a beam pipe of radius r to the number of CC events for a 1 m radius decay pipe. The decay pipe is 750 m long.

Decay Pipe Length (m)	R - Near Detector	R - Soudan
700	.965	.96
650	.920	.92
600	.873	.87
550	.823	.82
500	.770	.77
450	.713	.71
400	.654	.65

Table 3.11: Effect on the ν_μ charged current event rates of varying the decay tunnel length. R is the ratio of the number of CC events for a decay pipe of length L to the number of CC events for a 750 m long decay pipe. The decay pipe radius is 1 m.

3.5 Hadron Absorber

A massive structure is located at the end of the decay region to absorb the secondaries, non-interacting protons, and, during target-out studies, the primary proton beam. The hadron absorber is similar in construction to present Fermilab designs. A central water-cooled core is surrounded by steel. The outer dimensions of the steel are about 3 m x 3 m x 4.9 m long with an upstream inner core of aluminum 2.45 m long and a similar downstream core of copper. If the core size is 61 cm x 61 cm, the power in the materials for standard proton intensity is Al (220 kW), upstream steel (32 kW), Cu (65kW) and downstream steel (2 kW).

Existing RAW (RadioActive Water) System designs include capacities of 200 kW, 60 kW, and 11 kW. Therefore, either two existing 200 kW systems would need to be located, refurbished, and installed for the absorber or a single new 400 kW design would have to be built and installed. The latter option is likely to be more cost effective.

Motion control for the hadron absorber is believed to only require gross manual positioning to the ± 1 inch level. Remote or fine precision motion control is neither needed nor has it been costed.

It is assumed that the bulk shielding for the hadron absorber will consist of cast salvage steel slabs @ \sim \$200/ton. The radial extent of the shield has not been determined.

3.6 Beam Monitoring using Muons

The same decay chain which is the principal source of neutrinos, i.e., $\pi^+ \rightarrow \mu^+ \nu_\mu$, is therefore necessarily also a source of positive muons. Hence, the focusing systems employed to maximize the flux of neutrinos for MINOS and COSMOS will also enhance the flux of muons. The rock located between the hadron absorber and the experimental halls acts as a “muon shield” and a set of charged particle detectors placed inside the muon shield can directly measure this muon flux. The muon flux is sensitive to what happens to the muon decay parents as they pass through the focusing systems and measurements of the flux at different locations in the muon shield can provide information on the energy distribution of the muons.

The CERN neutrino program has used solid state detectors (SSDs) as muon counters in the muon shield for a number of years. The characteristics of the CERN SSDs are given in Table 3.12. The CERN experience with these muon counters, described in [27, 28], has guided our thoughts about what the NuMI muon detection system should entail.

Thickness (μm)	Area (mm^2)	Lower flux limit (muons/ cm^2)	Upper flux limit (muons/ cm^2)
100	30	15000	7×10^8
300	100	1500	7×10^7
500	200	400	2×10^7
1000	200	200	1×10^7

Table 3.12: Parameters for solid state detectors used at CERN

Monte Carlo Study

As shown in Section 3.3.3, the changes to the focusing system that most affect the neutrino flux distribution at the far and near MINOS detector positions are: (1) a transverse shift of the first horn; (2) a change in current in all three horns. A study was made using `GEANT` to see how helpful muon detectors would be in detecting these two changes[29]. A transverse shift of the first horn changes the spatial distribution of the muons in the plane perpendicular to the beam axis. The size of the effect on the observed distributions depends on the position of the muon detectors in the rock (dolomite) shield. Changing horn currents affects the momentum spectrum of the muons and, therefore, changes the flux of muons at different locations along the beam direction in the dolomite.

Placement of Slots The muon detectors will be placed in slots cut in the dolomite between the hadron absorber and the hall for the COSMOS detector. The number of muons reaching each slot decreases with distance from the hadron absorber because the muons range out in the dolomite. Hence, the muon energy distribution gets harder (i.e., the threshold energy increases) at each subsequent downstream slot.

Table 3.13 shows the characteristics of the slot positions that were studied. The minimum initial energy required for a muon to reach a slot is approximately given by the sum of the mean energy loss in the hadron absorber (estimated to be 8.1 GeV) and the kinetic energy (KE) corresponding to the range value for the relevant thickness of rock. It is this minimum initial energy which is given in column 4 of Table 3.13.

The choice of the number of slots and their placement is still under study.

Slot Label	Distance from end of Hadron Absorber (cm)	Kinetic Energy from Range Table (GeV)	Minimum Initial Energy (GeV)
1o	870	4	12
2o	1520	7	15
3o	2300	11	19
4o	3470	17	25
1	1700	8	16
2	4850	24	32
3	7100	36	44
4	9670	50	58
5	11800	62	70

Table 3.13: Slot Positions and Equivalent Energies

Sensitivity to Changing Horn Current Figure 3.34 and Table 3.14 show the effect on the muon flux caused by varying the current simultaneously in all three horns by $\pm 10\%$. A larger than anticipated current offset has been selected in order to obtain a clearly significant (on the scale of the limited statistics of a practical length GEANT Monte Carlo run) flux change.

Sensitivity to the Position of Horn 1 A Gaussian was fit to the muon transverse position distribution for each slot, both for Horn 1 in its nominal position, and offset by 4mm. The GEANT Monte Carlo data were binned in two ways: many small bins (“multi-bin”) and in seven 60×60 cm bins in order

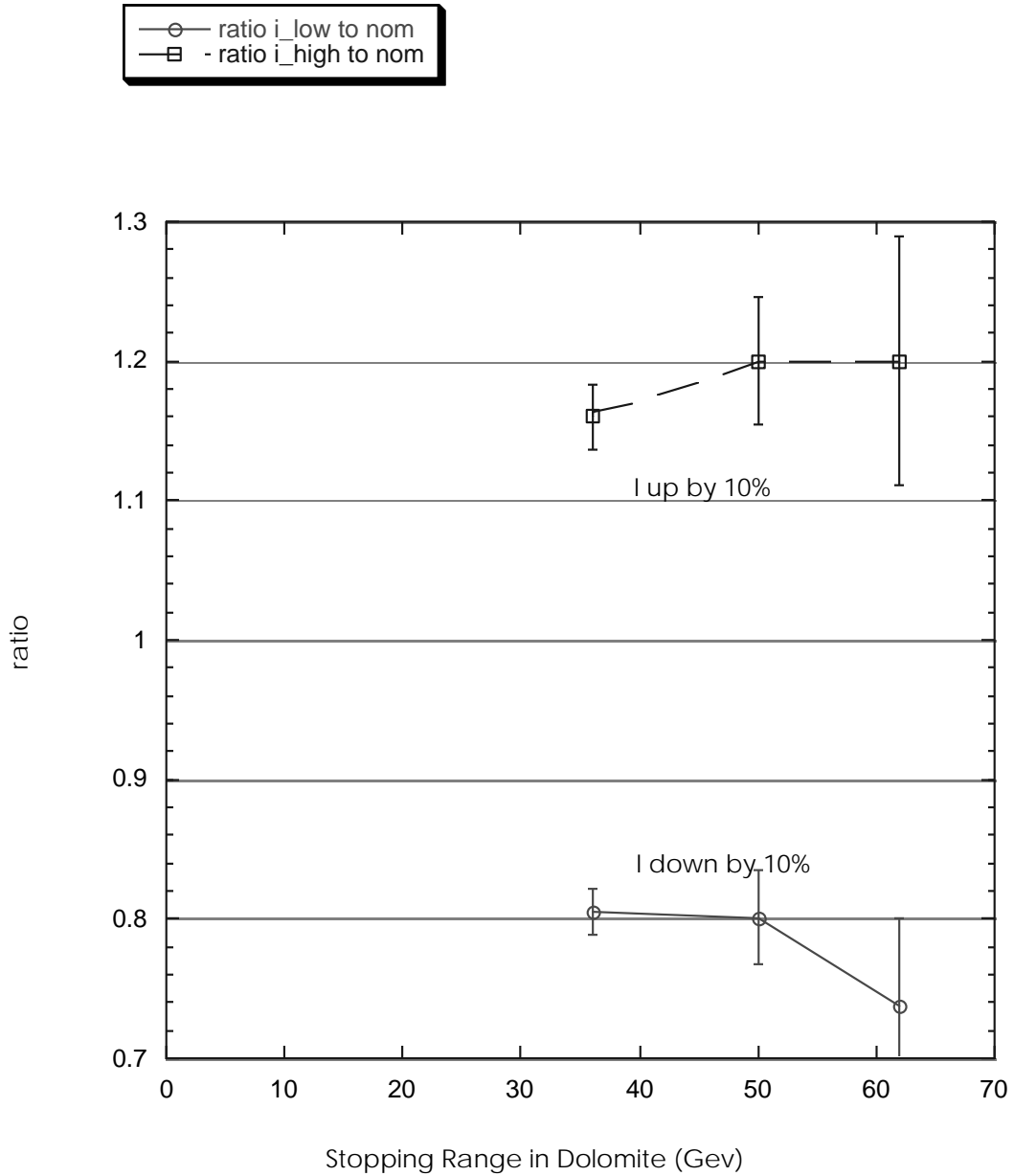


Figure 3.34: Muon Flux Change due to Horn Current Change

This figure shows the ratio of muon flux after lowering or raising the horn current by 10% to the flux at nominal horn current for three slot positions. The Stopping Range values correspond to slots located 7100 cm, 9670 cm, and 11800 cm downstream of the hadron absorber. The error bars are statistical only, corresponding to the number of events generated.

Kinetic Energy (GeV)	Effect of 10% Drop in Horn Current	Effect of 10% Rise in Horn Current
36	$(-19.4 \pm 1.7)\%$	$(15.7 \pm 2.3)\%$
50	$(-19.9 \pm 3.4)\%$	$(20.2 \pm 4.6)\%$
62	$(-26.2 \pm 6.2)\%$	$(19.9 \pm 8.9)\%$

Table 3.14: Effect of changing horn current. The errors given are statistical only, set by the number of generated Monte Carlo events.

to simply simulate a realistic number of counters. The center of each of these bins could be occupied by a ~ 100 mm² SSD. The shifts in the fitted means are shown in Figure 3.35. The errors shown are based on the number of events generated and represent a miniscule portion ($< 10^{-7}$) of the number of protons for one spill. The stability of the calibration coefficients for the CERN solid state detectors[27] was generally better than 2% over long periods of time. The error in the sensitivity parameters that they assign includes 2% for detector signal fluctuations[30]. Because accumulating statistics will not be a problem, these detector systematic uncertainties will set the errors on the mean to be on the order of 1-2%.

Conclusions of the Muon Study

Ultimate Sensitivity The number of muons penetrating 11800 cm into the dolomite shield (62 GeV stopping power) per spill of 4×10^{13} protons is sufficiently high that the statistical error on the signal from muon counters placed at that position (for one spill) is less than the systematic error expected for the solid state detectors, even assuming that the systematic uncertainty due to gain fluctuations, calibration errors, etc., could be as small as 1%.

Sensitivity to the Position of Horn 1 It was reported in Section 3.3.3 that to control knowledge of the neutrino spectrum to 2%, horn 1 should be kept to within 1 mm of its nominal position. The deviations in the neutrino energy spectrum were observed to be quadratic in the offset of horn 1. Scaling in this fashion, the shift in the mean of the muon transverse position distributions for the slot at 11800 cm from the hadron absorber (slot 5) due to a 1 mm horn translation would be $-25.9 \text{ cm} \times (1 \text{ mm}/4 \text{ mm})^2 = -1.62 \text{ cm}$. The level of the error that might be expected is 0.7 cm or less, set by systematic errors associated with the solid state detectors. As seen in Figure 3.35, in the dolomite about 5000 cm beyond the absorber (slot 2), the fitted mean is about +10 cm. When

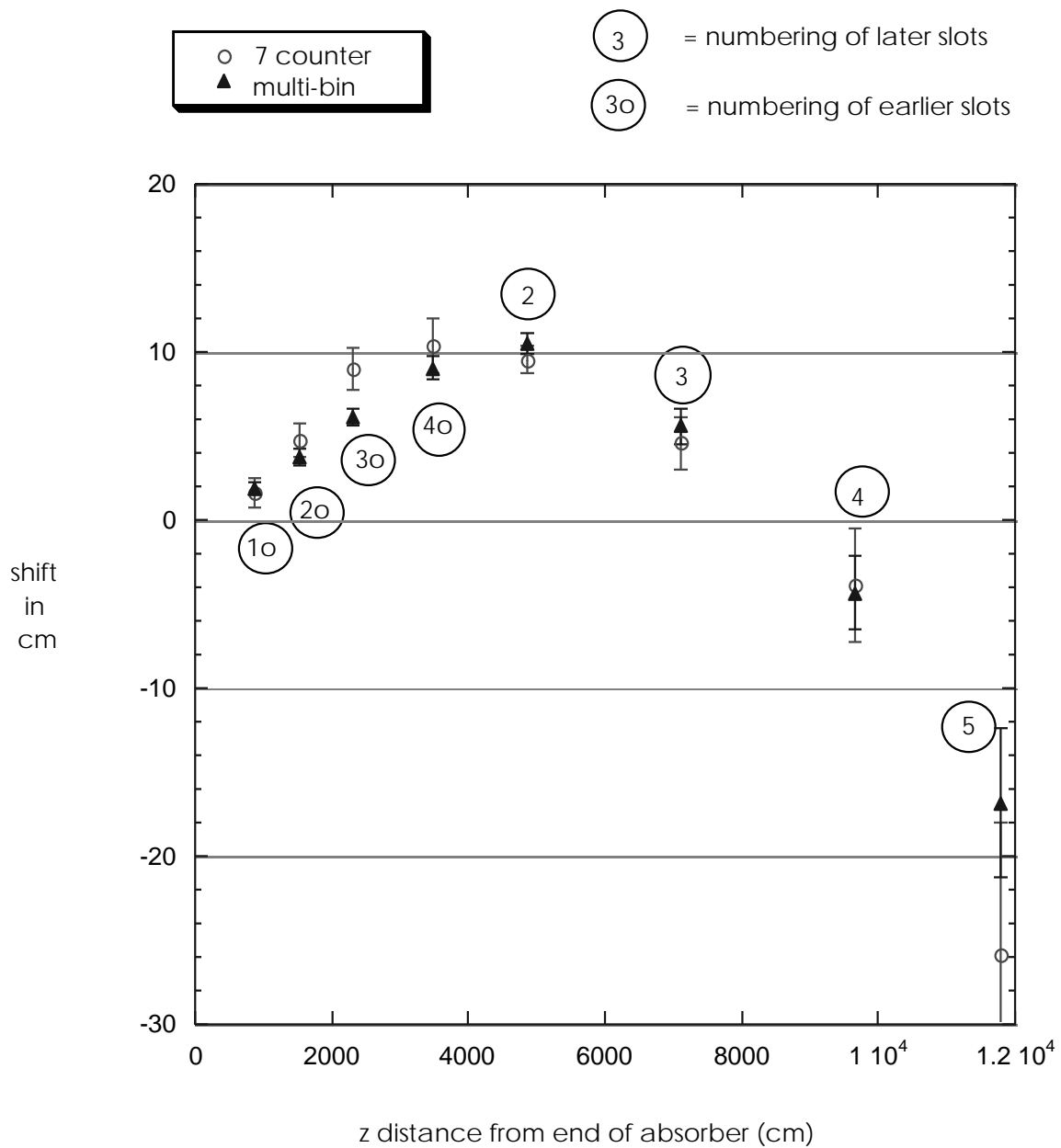


Figure 3.35: Shift in Mean due to Horn 1 shift

This figure shows shift in the mean of muon x distributions (derived from fitting to a Gaussian), for both “counter” histograms and “multi-bin” histograms (see text), due to a Horn 1 shift by 4 mm. The errors given are statistical only, set by the number of generated Monte Carlo events. The slot labels are defined in Table 3.13.

scaled to correspond to a 1 mm displacement of horn 1, this becomes 0.6 cm. Again, the error will be set by detector calibration uncertainties, etc., and a reasonable estimate is that it will be 0.3 cm or less. The conclusion is that this muon distribution will be sufficiently sensitive to detect a significant shift in horn 1 position.

Sensitivity to Changing Horn Current As shown in Section 3.3.3, the desired 2% knowledge in the normalization of the neutrino energy spectrum at Soudan means that horn current deviations from nominal need be less than 0.8%. It was noted that the spectrum deviations were observed to be linear in horn current deviation. Scaling in this fashion from the result in Table 3.14 for the slot at 11800 cm would give a change in the muon flux of $2\% \times (0.8\%/10\%) = 1.6\%$.

For a relative error of 2% on the stability of the signals from the SSDs, we could expect the worst-case error on the ratio of rates to be 0.028, i.e., $2\% \times \sqrt{2}$. This is the worst-case scenario because it is assumed that the two measurements are completely uncorrelated. Further, this error results if measurements from only one slot are used. If 1% stability in the SSD response could be achieved, then this worst-case error on the value of 1.016 would still be 0.014. The sensitivity is therefore marginal and we should strive for 1% stability on the SSDs as well as study in more detail how measurements from different slots can be combined.

Number and Locations of Slots The best guide to number and placement of slots may be Figure 3.35. Three seems to be a minimum number. At present, CERN is using 64 SSD's installed in 3 of the 6 existing slots[31]. One slot should be located about 1000 cm downstream of the hadron absorber. This one is chosen to be relatively insensitive to the changes in horn conditions that have been discussed. A second position should be at the point of maximum positive excursion shown on Figure 3.35. The third should be where slot 5 has already been placed, at 11800 cm.

Future Studies The topic of beam monitoring using muons should be revisited when the Hadronic Hose design is sufficiently mature.

3.7 Muon Absorber

The short baseline experiment, COSMOS, uses a photographic emulsion technique to detect the production and subsequent decay of tau neutrinos. This emulsion is sensitive to ionization effects from charged particles passing through it.

All strongly interacting particles produced at the production target are stopped by the hadron absorber at the end of the decay pipe and are not a problem for COSMOS. High energy muons, on the other hand, which are copiously produced both promptly at the production target and through the decay of secondaries, pass through the hadron absorber, and could pose a serious threat to the integrity of the COSMOS emulsion. These muons must be ranged out by the presence of further shielding material. There is ample shielding material naturally present between the hadron absorber and the COSMOS experimental hall in the form of dolomitic limestone to control this “punch-through” problem.

The COSMOS collaboration has calculated that the emulsion can withstand $10^5 \mu/\text{cm}^2$ over the four-year run of the experiment. There is an irreducible flux of muons coming from neutrino interactions occurring in the dolomite shield itself. With the standard 3-horn NuMI wide band beam and using the FLUKA hadron production model this equilibrium flux of muons is $3.2 \mu/\text{m}^2/10^{13}$ protons on target. This is approximately $50,000 \mu/\text{cm}^2$ over the four year run, within a factor of two of the COSMOS limit. Since other sources such as cosmic rays can also affect the emulsion, the dolomite shield should reduce the muons from punch-through to $1.3 \mu/\text{m}^2/10^{13}$ protons on target.

To determine the required length of dolomite to reduce the initial flux of muons to the quoted acceptable level, several independent analyses have been conducted[32, 33]. The major assumptions and conclusions of these analyses can be summarized as follows:

1. The density of dolomite used in these calculations is $2.588 \text{ gm}/\text{cm}^3$,
2. 120 GeV muons have a range of 205 m via mean energy loss in dolomite,
3. Straggling adds 16% to the required range.

The overall conclusion is that a shield length of 240 m will give a sufficient safety factor to account for both possible cracks in the dolomite and fluctuations in the dolomite density.

3.8 Radiation Concerns

Four different concerns related to radiation in NuMI have been identified and examined. Namely:

- Prompt beam-on radiation;
- Activation of beamline components and shielding materials;
- Air activation;
- Groundwater contamination, in particular with tritium.

Of these four, groundwater contamination is the most serious and has received the most attention. It is treated in detail here, following a summary of the status of the first three, which are discussed in detail in Reference [1].

3.8.1 Prompt radiation, neutrons and muons

The feature of the NuMI beam which distinguishes it from others at Fermilab is the depth beneath the surface at which the majority of its components lie. As is discussed below, this complicates the problem of groundwater irradiation. However it simplifies the matter of prompt radiation at the surface. This question has been studied using the simulation program CASIM[9] by assuming the entire beam is dumped accidentally into various components. The results indicate that for the pretarget hall and all downstream enclosures, the depth is sufficient to avoid any problem at the surface. Namely, the shielding provided by the overlying rock and soil is adequate to classify the surface as fit for unlimited occupancy, except in the regions of any vertical shafts. Since there will also be personnel access to the experimental halls beneath the surface, prompt radiation is also a concern at these locations.

The regions of the vertical shafts need to be studied in detail. In the case of the upstream one there is an added complication of the horn power supply area being situated essentially in the shaft between the surface and the target hall depth, and it is desired that this area be fit for beam-on occupancy. The present plan is to separate the bottom of the shaft from the rest of the target hall via a labyrinth, which is yet to be designed.

The construction plan calls for the underground tunnel to be continued from the decay pipe through to the experimental halls, bypassing the beam absorber and the muon shield of the COSMOS experiment. If left open, this would leave a path for radiation to reach the experiments from the hadron absorber, via this tunnel section. Thus, at a minimum, a labyrinth must be constructed

in this bypass. It has been suggested that this tunnel section be totally and permanently blocked off, once construction is completed.

3.8.2 Activation of Components

Targets, focusing horns, target hall instruments, and the inner parts of the target hall shielding will be exposed to very large amounts of radiation. The proton flux specification for this region is 4×10^{13} 120 GeV protons every 1.9 seconds. This is more than an order of magnitude more flux than is experienced in the AP0 antiproton target hall. Activities of several hundred rads per hour are expected from exposed components. The initial scenario for the shielding in this hall is that of the antiproton hall itself, but with cognizance of the larger components (specifically horns), the greater radiation levels, and the 58 mr slope of the beam.

There is an ongoing discussion as to whether components removed from the beamline will be reusable, or whether they will be too activated ever to be worked on in case of failure. In either case a region of the target hall should be reserved for these highly radioactive components that will not normally be accessible to personnel. Effecting maintenance on the “hadronic hose” (see section 3.3.5), which is in the decay pipe, may be difficult due to the residual radiation levels in the decay pipe.

3.8.3 Air Activation

The most troublesome isotope produced by the interaction of a particle beam in air is ^{11}C . Reference [1] discusses the fact that if no action were taken to minimize production of this isotope then a cool-down time of four hours would be required before personnel could enter the target hall, in the absence of ventilation. In Figure 3.36 is presented a version of this hall with helium replacing air over much of the affected volume. It should be noted that in the process of evolving from a two-horn to a three-horn focusing system, steel shielding has also replaced much of the air in the design presented in [1]. The combined result is that the effective cool-down time is reduced to approximately one hour for the no ventilation case. Tritium can be produced by stars in this helium, and studies of the expected tritium levels are underway.

3.8.4 Groundwater Activation

Particle beams beneath ground level have the potential for activating groundwater. The isotopes found to be of concern are tritium (^3H) and to a lesser extent

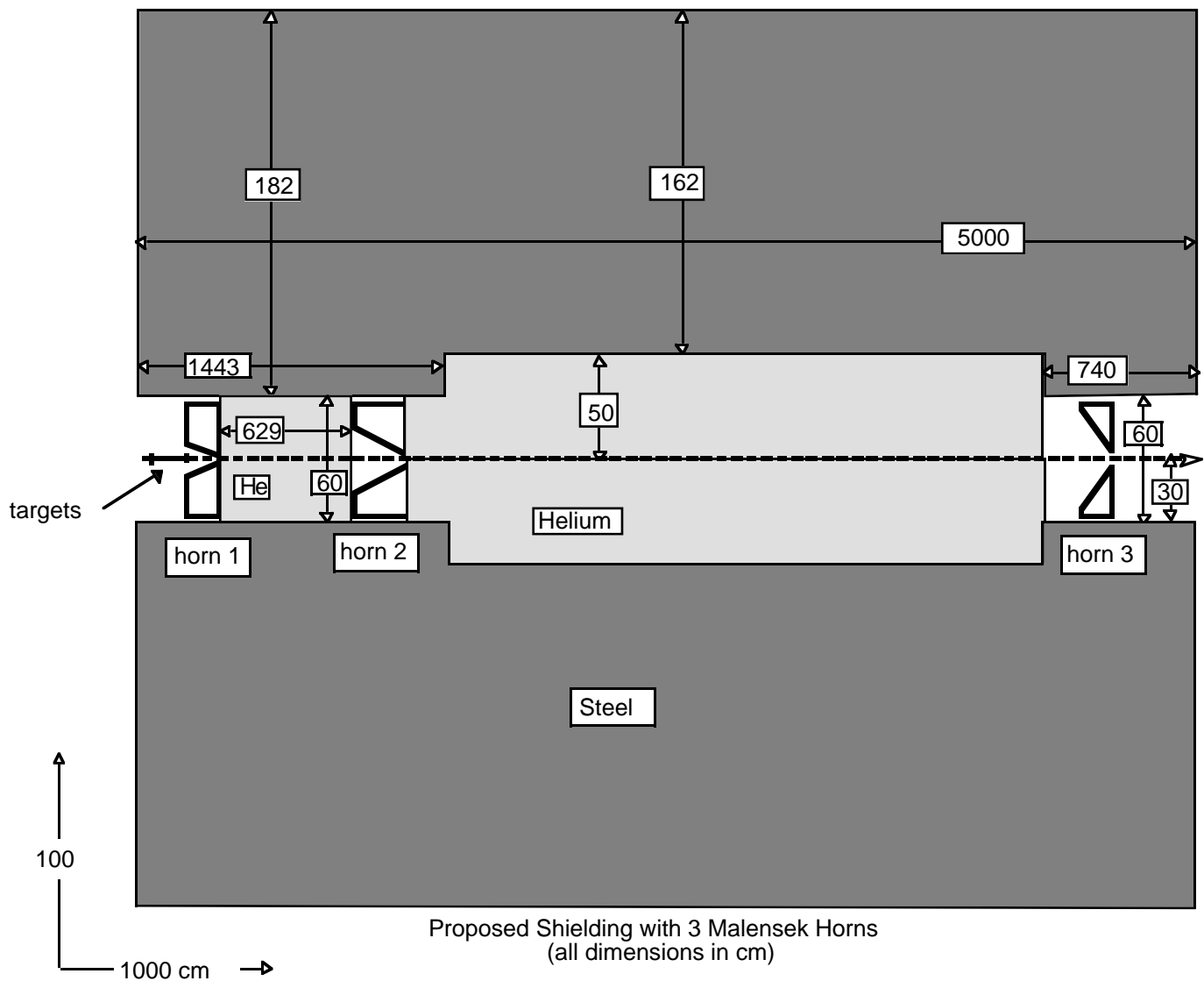


Figure 3.36: Configuration of the NuMI target hall.

^{22}Na . There is a particular concern in NuMI with groundwater due to the depths at which the various halls are located. For more typical constructions, at depths of order 10 meters, time is required for any activated water to migrate downward to the aquifer, and the activity, of course, decreases over this period. However, the NuMI target hall, decay pipe, and hadron absorber are planned to be located directly in the aquifer, thus requiring considerable shielding to keep activation levels acceptable. The shielding of the decay pipe is of particular concern due to the 750 m length which must be protected. Reference [34] discusses this matter in detail, with particular attention paid to the decay pipe region.

The Fermilab Concentration Model as Applied to NuMI A worst-case bound to the groundwater activation is calculated by assuming that the water is static. In this model, radiation levels will build up continually over the period the facility is operated. Any water movement, either inflow into the tunnel or seepage outward due to normal migration, will dilute the activation, but credit for this dilution is not taken. Actual flow rates will vary widely depending on the amount of fracturing of the rock, matrix conductivity, and also any grouting done on the tunnel walls.

The concentration of radioactivation C_i in water which might be extracted from the irradiated zone at the end of the run is given by

$$C_i = \frac{1}{0.037} \frac{K_i L_i}{\rho w_i} G S_{\max} N_p (1 - e^{-\lambda_i t}) \quad (pCi/cm^3)$$

where the parameters are given in Table 3.15. There are some uncertainties in the application of this model, depending on the presumed circumstances under which the water is later extracted. One such uncertainty is the fraction of radionuclides leached from the rock into the groundwater. Both 99% and 90% [35] values have been used at Fermilab. The table carries through the calculation for both, showing that the current shielding design is sufficient in either case. The product $S_{\max} G$ is intended to indicate the total number of stars per cm^3 in the surrounding dolomite rock. The volume of rock considered is that out to which the star density falls to 1% of S_{\max} . The geometrical factor G used in such averaging turns out to be about one order of magnitude larger for the NuMI decay pipe and target hall than for typical beam dumps found elsewhere in Fermilab. This difference is traced to the quite flat longitudinal distribution of star density.

The maximum star density, S_{\max} , comes from a CASIM Monte Carlo run which models the NuMI configuration. The rate of protons on target, N_p , is assumed to be 3.7×10^{20} protons per year, but with two years downtime for beamline reconfiguration, impact of other fixed target programs, etc., during

	^{22}Na	Tritium
G (geometry factor) $\Delta R=1.5\text{m}$	0.19	0.19
N_p (rate of protons on target)	$9.4 \times 10^{12} \text{ sec}^{-1}$	$9.4 \times 10^{12} \text{ sec}^{-1}$
K_i (atoms radionuclide per star)	0.02	0.03
L_i (leachability)	(99%)	(1.0)
	90%	0.9
ρ (dolomite density)	2.67 g/cm^3	2.67 g/cm^3
w_i (water leaching factor)	(99%)	(0.5)
	90%	0.27
λ_i (decay reciprocal meanlife)	$8.45 \times 10^{-9} \text{ sec}^{-1}$	$1.78 \times 10^{-9} \text{ sec}^{-1}$
t (run time of 10 years)	$3.15 \times 10^8 \text{ sec}$	$3.15 \times 10^8 \text{ sec}$
Target Hall Region		
S_{max} (star density) stars/cm ³ /proton	7×10^{-12}	7×10^{-12}
C_i (concentration) stagnant	(99%)	(2.9 pCi/ml)
	90%	5.4 pCi/ml
Decay Pipe Region		
S_{max} (star density) stars/cm ³ /proton	1.3×10^{-11}	1.3×10^{-11}
C_i (concentration) stagnant	(99%)	(5.4 pCi/ml)
	90%	10 pCi/ml
Regulatory limit on C_i	0.4 pCi/ml	20 pCi/ml

Table 3.15: Parameters for a “static water” model of NuMI.

the ten years of postulated operation. The values of K_i , L_i and ρ for dolomite are taken from Reference [36].

The requirement on activation is that the sum of the ratios of concentrations to their limits be less than unity. That is,

$$\frac{C_{Na}}{C_{Na}^{Limit}} + \frac{C_H}{C_H^{Limit}} < 1$$

Target Hall Shielding Requirement Figure 3.36 indicates the configuration of shielding steel as observed in longitudinal section, and Figure 3.37 shows the distribution of star densities at the outer steel surface. To interpret these results, it is useful to reduce the concentration model to its simplest terms. The factor in the formula which is provided by CASIM, or any other simulation program, is S_{max} , the maximum number of stars per cm³ per incident proton.

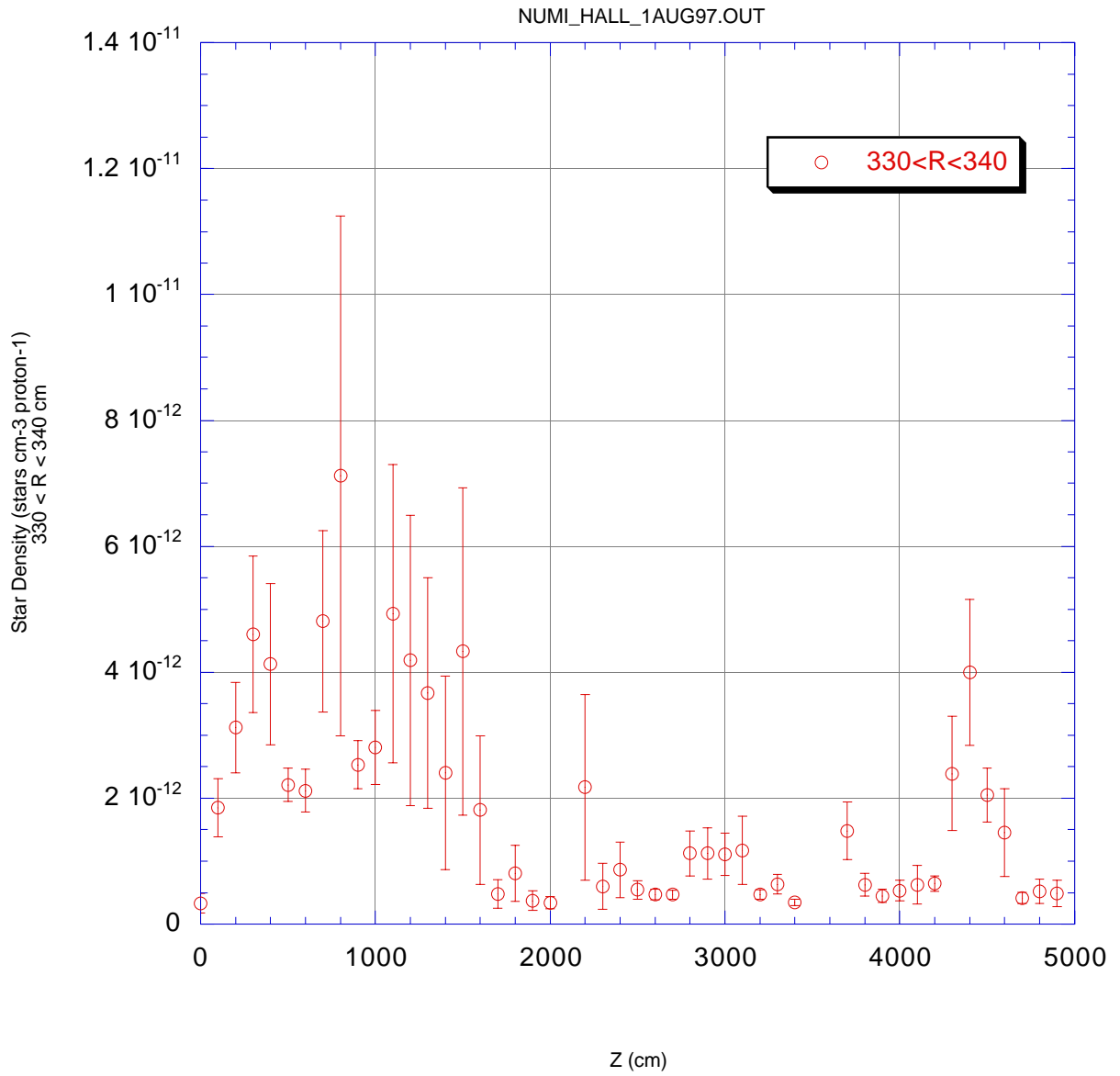


Figure 3.37: Star density in the vicinity of the NuMI target hall, calculated by the CASIM Monte Carlo program.

The entire model and regulatory requirements reduce, after inclusion of all geometrical and geological factors, to the statement that $S_{max} < 1.88 \times 10^{-11}$ stars/proton-cm³.

Although some statistical fluctuations are seen in the figure, most data lie comfortably (a factor of three) below the limit.

It should be pointed out that for running with a narrow band beam, a large fraction of the primary protons will have to be absorbed in the target hall. Thus the shielding requirements in this region will increase. Those requirements, assuming some generic narrow band design, are being studied. It is wise to develop the shielding scenario now, even though that beam is several years away, so that the hall configuration can comfortably contain the amount of shielding which will be required.

Decay Pipe Shielding Requirement Figure 3.38 is a transverse section of a decay region shielding concept, and Figure 3.39 shows the results of a CASIM calculation utilizing it. The highest star density observed in the CASIM results is at 70% of the limit determined above, and groundwater regulatory limits and guidelines are thus met.

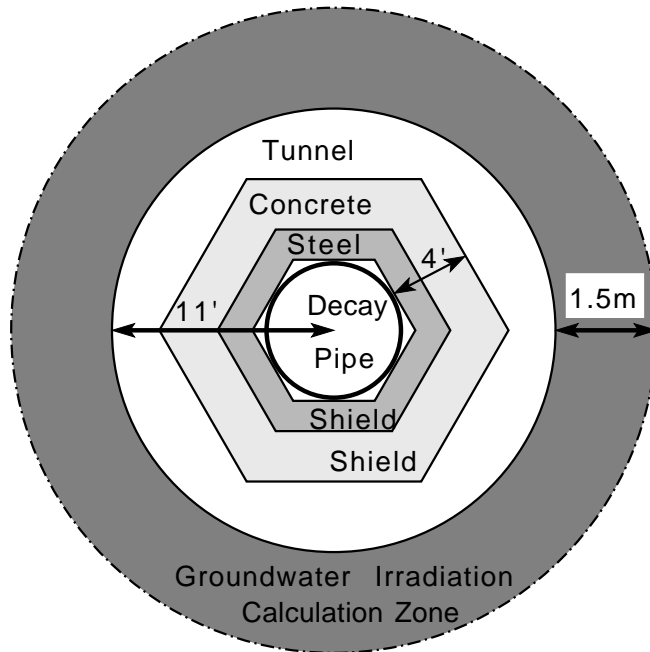


Figure 3.38: Configuration for calculation of groundwater irradiation in the region of the NuMI decay pipe.

**Star Density at 330-340 cm Radius in Dolomite
for Region Downstream of the Target Hall.
Assumes 100 cm Radius Pipe, 18" Thick Fe and
30" Thick Concrete Shielding Around Decay Pipe**

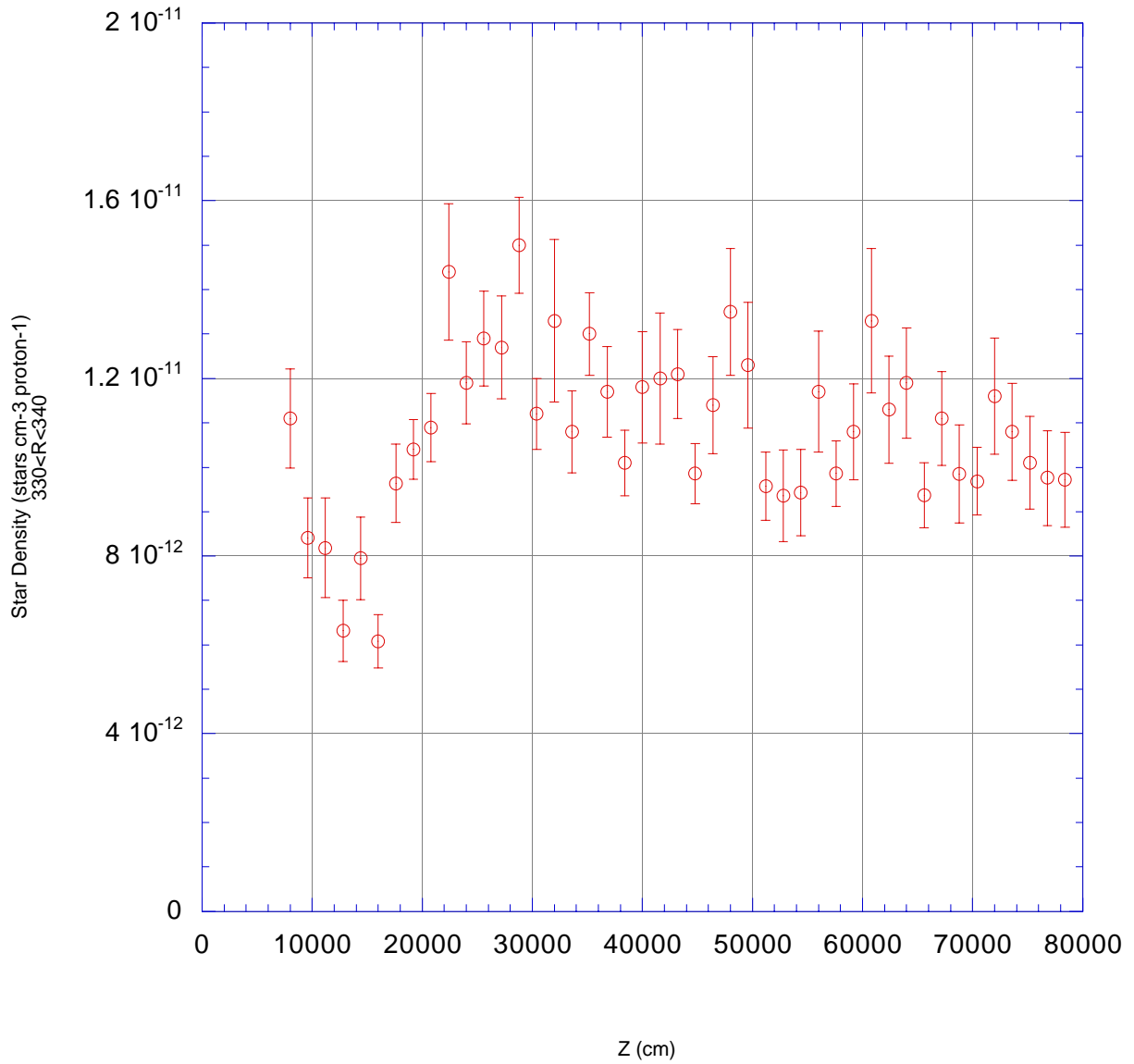


Figure 3.39: Star density along the decay pipe calculated by the CASIM Monte Carlo program.

For future narrow band beam running, the shielding requirements for the decay pipe are decreased compared with those for the wide band beam. Thus the shielding being designed now will also be adequate for the narrow band case.

As was noted above, the shielding of this region is one of the major challenges in the design of the entire NuMI beam. The 750 meter decay pipe and noticeable beamline slope relative to horizontal imply the need for a sophisticated installation procedure and a not inconsiderable monetary expense. Other shielding configurations are being considered to see if some cost savings can be achieved.

Hadron Absorber Shielding A design for the shield of the hadron absorber has not yet been developed in detail; however the general parameters and shape of the result can be intuited. The purpose of the absorber is to completely contain all of the uninteracted primary protons plus all of the interaction products. The shielding must extend the absorber both longitudinally and radially to an extent appropriate for groundwater considerations.

Radionuclide Concentration in Sump Water As is true for any underground excavation, the head of water in the aquifer above the NuMI tunnel will lead to an inflow of water into the tunnel. According to consulting engineering firms [37, 38] the inflow of water into the NuMI tunnel would be substantial if no attempt were made to stem it. Most of the inflow occurs in regions constituting a small fraction of the total length of the tunnel. The recommendation is to grout these regions during construction so as to keep the inflow to a rate of 100 to 300 gallons of water per minute per mile of tunnel. The purpose of this section is to estimate the concentrations in this water taken out through the tunnel to the surface.

The most conservative approach is to calculate the concentration in a steady state condition. That is, calculate the leachable activity in the rock produced by the NuMI beam and assume it is all removed by the water flowing into the tunnel. This will clearly give an upper limit on the concentration in this inflowing water.

We have from the concentration model that the number of radionuclide i produced per unit volume per unit time that is leachable is $GS_{\max}N_pK_iL_i$. The volume we use for calculating a concentration is an annulus of length $L=750$ m and with R_0 and R_{\max} of 330 cm and 480 cm, respectively. This volume, V , is then $V = \pi(R_{\max}^2 - R_0^2)L$ and for the inflow, Q , the concentration, C_i , is given by:

$$C_i = \frac{1}{0.037} \lambda_i GS_{\max} N_p K_i L_i V / Q$$

in pCi/cm³. Using $Q=100$ gallons/minute/mile (the conversion factor is 1 gallon = 3875 cm³) and the values of the various parameters for ²²Na and ³H given in Table 3.15 gives $C_{Na}=0.012$ pCi/cm³ and $C_H=0.4$ pCi/cm³. These are well below even the regulatory limit of $C_H=20$ pCi/cm³ and the DOE guideline of $C_{Na}=0.4$ pCi/cm³ applicable to Class I groundwater, and far below the DOE guidelines of $C_H=2000$ pCi/cm³ and $C_{Na}=10$ pCi/cm³ for surface discharge.

It should be added that the groundwater activity outside the tunnel will clearly be reduced due to water inflow. To estimate the effect, however, requires a much more sophisticated analysis than is presented here.

Groundwater Activation Monitoring A comprehensive monitoring program will form an integral part of the NuMI groundwater protection plan. While the shielding design is such as to keep all production of radionuclides in unprotected regions within regulatory limits for potable groundwater, verification that this indeed remains the case with extended operation is very important.

Monitoring of integral activation doses will enable empirical verification of shielding effectiveness. This will be accomplished by the positioning of activation tags in accessible locations outside of the radiation shield. Activity in these tags can then be counted to determine integral doses received at these locations. Results from these measurements enable comprehensive comparison with design calculations, including absolute normalization. Such information is especially important in regions where the shield geometry is more complex, such as for the shield surrounding the target and focusing horn system.

Regular sampling will be done for radionuclide levels in cooling water systems, including both the closed loop RAW system serving components experiencing higher activation levels, and the LCW cooling system serving conventional beam transport elements. RAW water spills are controlled by a combination of continuous water level sensing, along with secondary containment vessel collection and tightly controlled sump discharge.

Direct sampling for radionuclide presence in inflow water collected in sump pits serving the target hall, decay tunnel, and beam dump hall will be done on a regular basis. Additionally, several monitoring lines will be established in these same areas to draw sample quantities of water directly from the rock in the region outside of the protective shields.

As measurement sensitivities for critical radionuclides are sufficient to detect and monitor levels well below the applicable limits and guidelines in collected water samples, the planned regular monitoring program will provide continuous verification that NuMI operation is conducted with full protection of the groundwater resource.

Acknowledgements

The authors would like to acknowledge the contributions of the following individuals: R. Rameika, D. Pushka, C. T. Murphy, S. Childress, R. H. Milburn, the IHEP Protvino beam design group (in particular, V. Garkusha, V. Zarucheisky, and Y. Khodyrev), Z. Tang, S. O'Day, J. Walton, A. Para, D. Boehnlein, D. Cossairt, W. H. Freeman, and D. Wolff.

Appendix A

Coordinates of Beamline Elements for the Wide-Band Beam Primary Transport.

Program ces (A Construction Engineering Survey format) (11/26/91) Thu Aug 14 17:27:11 1997
Site coordinates for beamline: input_ces_v2
NOTES: Coordinates are given for the entrance of the device in DUSAF coordinate system.
Site +x-axis (EAST); site +y-axis (NORTH); Site z-axis (ELEVATION)
Positive bearing is ccw wrt site EAST.
Pitch is the vertical angle about the x-y plane.

line	location	typ_code	distance [ft]	x [ft]	y [ft]	z [ft]	brng [deg]	pitch [deg]	yaw [deg]
0000	S1_BML	marker	0.00000	101468.34139	97163.81440	715.72409	148.76849	0.00000	0.00000
0001	Q606	3Q84-2	0.00000	101468.34139	97163.81440	715.72409	148.76849	0.00000	0.00000
0002	Q607	3Q84-2	53.22115	101422.83308	97191.40942	715.72409	148.76849	0.00000	0.00000
0003	Q607	3Q84-2	56.72115	101419.84030	97193.22415	715.72409	148.76849	0.00000	0.00000
0004	C_608	MIHC	97.07773	101385.33224	97214.14894	715.72409	148.76849	0.00000	0.00000
0005	L6081	MILAM	99.45850	101383.29648	97215.38336	715.72409	148.76849	0.00000	-77.39514
0006	Q608	3Q84-2	109.94227	101374.33203	97220.81917	715.72409	148.76849	0.00000	0.00000
0007	Q608	3Q84-2	113.44226	101371.33925	97222.63390	715.72409	148.76849	0.00000	0.00000
0008	L6082	MILAM	118.80721	101366.75183	97225.41562	715.72409	148.76849	0.00000	-84.38522
0009	L6083	MILAM	130.00509	101357.17671	97231.22171	715.72409	148.76849	0.00000	-87.88027
0010	V100	CMG_1	141.58951	101347.27112	97237.22820	715.72409	148.76849	0.00000	85.87491
0011	HQ101	3Q120-2	156.84421	101334.26866	97245.20331	716.54092	148.69573	1.63178	0.00000
0012	HQ101	3Q120-2	161.84420	101329.99829	97247.80019	716.68328	148.69573	1.63178	0.00000
0013	HP101R	SYBPM_S	167.34419	101325.30093	97250.65675	716.83987	148.69573	1.63178	0.00000
0014	VP101R	SYBPM_S	168.38326	101324.41349	97251.19641	716.86947	148.69573	1.63178	0.00000
0015	HV1011	EPB	181.47398	101313.23307	97257.99541	717.24220	149.00426	1.63178	0.00000
0016	HV1012	EPB	192.64066	101303.66163	97263.73821	717.56015	149.62163	1.63150	0.00000
0017	HV1013	EPB-R	203.80734	101294.02884	97269.37754	717.87803	150.23841	1.60801	-4.24390
0018	HV1014	EPB-R	214.97405	101284.33582	97274.91296	718.19095	150.85434	1.56188	-4.24390
0019	HV1015	EPB-R	226.14072	101274.58364	97280.34399	718.49486	151.33391	1.28257	-56.11606
0020	HV1016	EPB-R	237.30743	101264.78638	97285.69634	718.73951	151.67740	0.76948	-56.11606
0021	HV1017	EPB-R	248.47411	101254.95566	97290.99065	718.88426	152.02089	0.25640	-56.11606
0022	HQ102	3Q120-2	266.82069	101238.74191	97299.57581	718.92901	152.19249	0.00000	0.00000
0023	HQ102	3Q120-2	271.82068	101234.31932	97301.90832	718.92901	152.19249	0.00000	0.00000
0024	HQ103	3Q120-2	282.82066	101224.58964	97307.03983	718.92901	152.19249	0.00000	0.00000
0025	HQ103	3Q120-2	287.82065	101220.16705	97309.37234	718.92901	152.19249	0.00000	0.00000
0026	HP103R	SYBPM_S	293.32064	101215.30219	97311.93809	718.92901	152.19249	0.00000	0.00000
0027	VP103R	SYBPM_S	294.35968	101214.38314	97312.42283	718.92901	152.19249	0.00000	0.00000
0028	PM103	SYSWIC	295.70085	101213.19685	97313.04848	718.92901	152.19249	0.00000	0.00000
0029	HC103	MIHC	297.67788	101211.44813	97313.97076	718.92901	152.19249	0.00000	0.00000
0030	VC103	MIVC	299.16912	101210.12911	97314.66643	718.92901	152.19249	0.00000	0.00000
0031	HP104R	SYBPM_S	455.51845	101071.83506	97387.60385	718.92901	152.19249	0.00000	0.00000
0032	VP104R	SYBPM_S	456.55749	101070.91597	97388.08856	718.92901	152.19249	0.00000	0.00000
0033	PM104	SYSWIC	457.89862	101069.72972	97388.71421	718.92901	152.19249	0.00000	0.00000
0034	HQ104	3Q120-2	460.01817	101067.85495	97389.70299	718.92901	152.19249	0.00000	0.00000
0035	HQ104	3Q120-2	465.01816	101063.43235	97392.03550	718.92901	152.19249	0.00000	0.00000
0036	HQ105	3Q120-2	483.36065	101047.20808	97400.59230	718.92901	152.19249	0.00000	0.00000
0037	HQ105	3Q120-2	488.36064	101042.78548	97402.92481	718.92901	152.19249	0.00000	0.00000
0038	V1051	B2-R	494.27729	101037.55209	97405.68495	718.92901	152.19134	-0.74914	-90.00021

0039	V1052	B2-R	515.36114	101018.90554	97415.51977	718.63813	152.18905	-2.24714	-90.00021
0040	V1053	B2-R	536.44499	101000.27251	97425.34836	717.79624	152.18704	-3.74514	-90.00021
0041	V1054	B2-R	557.52887	100981.66565	97435.16405	716.40385	152.18504	-5.24342	-90.00021
0042	HQ106	3Q120-2	594.63907	100949.00069	97452.39775	712.78886	152.18389	-5.99257	0.00000
0043	HQ106	3Q120-2	599.63906	100944.60284	97454.71818	712.26688	152.18389	-5.99257	0.00000
0044	HC106	MIHC	605.49653	100939.45029	97457.43655	711.65540	152.18389	-5.99257	0.00000
0045	VC106	MIVC	606.98780	100938.13858	97458.12864	711.49973	152.18389	-5.99257	0.00000
0046	HQ107	3Q120-2	610.56443	100934.99249	97459.78851	711.12633	152.18389	-5.99257	0.00000
0047	HQ107	3Q120-2	615.56442	100930.59440	97462.10895	710.60435	152.18389	-5.99257	0.00000
0048	HP107R	SYBPM_S	621.06441	100925.75655	97464.66144	710.03017	152.18389	-5.99257	0.00000
0049	VP107R	SYBPM_S	622.10348	100924.84257	97465.14365	709.92168	152.18389	-5.99257	0.00000
0050	PM107	SYSWIC	623.44462	100923.66288	97465.76606	709.78168	152.18389	-5.99257	0.00000
0051	STUB_E	MIHC	637.59128	100911.21924	97472.33133	708.30482	152.18389	-5.99257	0.00000
0052	PRE_E	MIHC	1003.92191	100588.98901	97642.34087	670.06129	152.18389	-5.99257	0.00000
0053	HP108R	SYBPM_S	1016.32608	100578.07811	97648.09749	668.76635	152.18389	-5.99257	0.00000
0054	VP108R	SYBPM_S	1017.36512	100577.16413	97648.57970	668.65788	152.18389	-5.99257	0.00000
0055	PM108	SYSWIC	1018.70626	100575.98444	97649.20211	668.51789	152.18389	-5.99257	0.00000
0056	HQ108	3Q120-2	1020.82581	100574.12008	97650.18574	668.29660	152.18389	-5.99257	0.00000
0057	HQ108	3Q120-2	1025.82580	100569.72199	97652.50617	667.77462	152.18389	-5.99257	0.00000
0058	HC108	MIHC	1031.68327	100564.56967	97655.22457	667.16313	152.18389	-5.99257	0.00000
0059	VC108	MIVC	1033.17454	100563.25793	97655.91663	667.00746	152.18389	-5.99257	0.00000
0060	HQ109	3Q120-2	1040.79533	100556.55456	97659.45337	666.21186	152.18389	-5.99257	0.00000
0061	HQ109	3Q120-2	1045.79532	100552.15647	97661.77380	665.68988	152.18389	-5.99257	0.00000
0062	V1091	EPB-R	1074.85497	100526.59517	97675.26003	662.65616	152.18418	-5.77169	-90.00021
0063	V1092	EPB-R	1086.02165	100516.76849	97680.44453	661.53769	152.18475	-5.33023	-90.00021
0064	V1093	EPB-R	1097.18832	100506.93442	97685.63278	660.50481	152.18533	-4.88876	-90.00021
0065	V1094	EPB-R	1108.35497	100497.09353	97690.82450	659.55767	152.18590	-4.44730	-90.00021
0066	V1095	EPB-R	1119.52165	100487.24643	97696.01934	658.69625	152.18647	-4.00583	-90.00021
0067	V1096	EPB-R	1130.68832	100477.39370	97701.21703	657.92067	152.18733	-3.56437	-90.00021
0068	HQ110	3Q120-2	1148.50000	100461.66856	97709.51236	656.84337	152.18790	-3.34378	0.00000
0069	HQ110	3Q120-2	1153.49999	100457.25368	97711.84129	656.55174	152.18790	-3.34378	0.00000
0070	HC110	MIHC	1159.55037	100451.91133	97714.65946	656.19885	152.18790	-3.34378	0.00000
0071	VC110	MIVC	1161.04164	100450.59460	97715.35404	656.11188	152.18790	-3.34378	0.00000
0072	HP110R	SYBPM_S	1162.39912	100449.39598	97715.98636	656.03271	152.18790	-3.34378	0.00000
0073	VP110R	SYBPM_S	1163.43819	100448.47850	97716.47035	655.97211	152.18790	-3.34378	0.00000
0074	PM110	SYSWIC	1164.77933	100447.29431	97717.09502	655.89387	152.18790	-3.34378	0.00000
0075	HPTAR	SYBPM_S	1222.17301	100396.61715	97743.82807	652.54643	152.18790	-3.34378	0.00000
0076	VPTAR	SYBPM_S	1223.21209	100395.69967	97744.31202	652.48583	152.18790	-3.34378	0.00000
0077	PMTAR	SYSWIC	1224.55323	100394.51548	97744.93673	652.40759	152.18790	-3.34378	0.00000
0078	TAR	TAR	1226.17278	100393.08547	97745.69106	652.31313	152.18790	-3.34378	0.00000
0079	TAR	TAR	1226.79614	100392.53507	97745.98141	652.27678	152.18790	-3.34378	0.00000
0080	TAR	TAR	1227.41949	100391.98465	97746.27176	652.24043	152.18790	-3.34378	0.00000
0081	TAR	TAR	1228.04285	100391.43426	97746.56212	652.20408	152.18790	-3.34378	0.00000
0082	TAR	TAR	1228.66621	100390.88383	97746.85247	652.16772	152.18790	-3.34378	0.00000
0083	TAR	TAR	1229.28957	100390.33344	97747.14283	652.13134	152.18790	-3.34378	0.00000
0084	TAR	TAR	1229.91293	100389.78301	97747.43318	652.09499	152.18790	-3.34378	0.00000
0085	TAR	TAR	1230.53629	100389.23262	97747.72353	652.05864	152.18790	-3.34378	0.00000
0086	TAR	TAR	1231.15964	100388.68219	97748.01385	652.02229	152.18790	-3.34378	0.00000
0087	TAR	TAR	1231.78300	100388.13180	97748.30421	651.98593	152.18790	-3.34378	0.00000
0088	TAR	TAR	1232.40636	100387.58138	97748.59456	651.94958	152.18790	-3.34378	0.00000
0089	AMHRN1	HORN1	1233.39061	100386.71232	97749.05303	651.89217	152.18790	-3.34378	0.00000
0090	AMHRN2	HORN2	1259.30919	100363.82686	97761.12547	650.38049	152.18790	-3.34378	0.00000
0091	AMHRN3	HORN3	1371.51369	100264.75314	97813.38846	643.83621	152.18790	-3.34378	0.00000
0092	DECAY	DECAY	1396.21837	100242.93957	97824.89549	642.39534	152.18790	-3.34378	0.00000
0093	DUMP	DUMP	3856.84337	98070.27043	98971.01410	498.88066	152.18790	-3.34378	0.00000
0094	SHIELD	SHIELD	3879.80920	98049.99219	98981.71119	497.54120	152.18790	-3.34378	0.00000
0095	EXP	EXP	4404.74254	97586.48944	99226.21651	466.92472	152.18790	-3.34378	0.00000

Appendix B

Neutrino Beam Design Monte Carlo Programs

Five particle physics Monte Carlo's were used in studies reported in this document. **GNuMI**, **NUADA**, and **PBEAM** were used to predict neutrino fluxes. **CASIM** and **MARS** were used to predict energy deposits for heating and radioactivation calculations.

The three ν beam simulation packages trade off speed versus range of effects that are included, as shown in Table B.1. Being essentially independently developed, they also serve as cross-checks of the calculations.

NUADA, originally written by Wilber Venus at CERN and modified and extended by David C. Carey at Fermilab, generates a matrix of production angles and momenta for π^\pm and K^\pm at the target, and tracks this “mesh” through the focusing system. At each step along each track, it integrates a neutrino flux at the detector which combines the production probability for that angle and momentum, the decay probability for that track, and the acceptance of the detector. Thus it is actually a calculation rather than a Monte Carlo. Continuing care is required to ensure that the granularity of the mesh is fine enough.

PBEAM, written by Noel Stanton at Kansas State University and with weighting methods incorporated by Wesley Smart at Fermilab, generates π^\pm , K^\pm , and K^0 in a Monte Carlo fashion, and tracks them through the focusing system. Absorption of hadrons in the horns is taken into account, but secondaries are not generated. Each hadron is then decayed at one position. **PBEAM** contains the option of generating neutrino fluxes two ways, either selecting random decay angles (i.e. unweighted Monte Carlo), or calculating the weight for that decay to produce a neutrino in the detector acceptance, a method developed by Rick Milburn of Tufts University.

GNuMI, written by James Hylan and Adam Para at Fermilab, generates

neutrino fluxes in a manner similar to PBEAM. It differs from PBEAM in being GEANT based, and in the larger number of effects that it includes. GNuMI was developed specifically for NuMI beam design. It includes code to properly handle the effect of polarization in the $\pi \rightarrow \mu \rightarrow \nu$ decay chain, including the angle and energy correlations, which is not part of GEANT.

	NUADA	PBEAM	GNuMI
Typical run time	0.2 hr	2 hr	200 hr
$\pi^\pm, K^\pm \rightarrow \nu_\mu, \bar{\nu}_\mu$	yes	yes	yes
$K_L^0 \rightarrow \nu_\mu, \bar{\nu}_\mu, \nu_e, \bar{\nu}_e$	no	yes	yes
$\mu^\pm \rightarrow \nu_\mu, \bar{\nu}_\mu, \nu_e, \bar{\nu}_e$	no	yes (ignores polarization)	yes
3 body decay model	none	phase space	V-A
Hadron absorption by horns etc.	yes	yes	yes
Secondary interactions from horns etc.	no	no	yes
μ (for monitor chambers)	no	yes	yes
Baryons (monitor chambers, radiation)	no	no	yes
Unweighted decays	no	yes	yes
Weighted decay to detector	K, π	K, π	K, π, μ

Table B.1: Comparison of programs used for neutrino beam simulation.

The speed of NUADA is useful when a large number of variations of parameters are to be looked at, but care must be used when interpreting the results. The wide band beam horn shapes were optimized with NUADA. The alignment studies used PBEAM's more realistic Monte Carlo tracking, at some cost in speed. GNuMI's larger range of physics effects were necessary for background studies, for calculating effects of secondary production from the horns and decay pipe walls, and, e.g., for realistic calculation of the level of the low energy tail for the narrow band beam.

Table B.2 shows the list of decays which contribute significantly to neutrino production in NuMI, and how they are modeled in GNuMI. See Figure 3.20 for their relative contributions to neutrino event rates.

Parent	$c\tau$	Daughter	Branching Ratio	Type
π^+	7.80 m	$\mu^+\nu_\mu$	100 %	Isotropic
π^-	7.80 m	$\mu^-\nu_{\bar{\mu}}$	100 %	Isotropic
K^+	3.71 m	$\mu^+\nu_\mu$	63.51 %	Isotropic
		$e^+\nu_e\pi^0$	4.82 %	Isotropic V-A
		$\mu^+\nu_\mu\pi^0$	3.18 %	Isotropic V-A
K^-	3.71 m	$\mu^-\nu_{\bar{\mu}}$	63.51 %	Isotropic
		$e^-\nu_{\bar{e}}\pi^0$	4.82 %	Isotropic V-A
		$\mu^-\nu_{\bar{\mu}}\pi^0$	3.18 %	Isotropic V-A
K_l^0	15.49 m	$\pi^-e^+\nu_e$	19.35 %	Isotropic V-A
		$\pi^+e^-\nu_{\bar{e}}$	19.35 %	Isotropic V-A
		$\pi^-\mu^+\nu_\mu$	13.50 %	Isotropic V-A
		$\pi^+\mu^-\nu_{\bar{\mu}}$	13.50 %	Isotropic V-A
μ^+	658.65	$e^+\nu_e\nu_{\bar{\mu}}$	100%	Polarized V-A
μ^-	658.65	$e^-\nu_{\bar{e}}\nu_\mu$	100%	Polarized V-A

Table B.2: Decays which produce neutrinos in **GNuMI**.

Bibliography

- [1] D. Crane *et al.*, “Status Report: Technical Design of Neutrino Beams for the Main Injector (NuMI)”, NuMI-B-92, FERMILAB-TM-1946, July 21, 1995.
- [2] D. Johnson, “MI-60 Extraction for NuMI”, NuMI-B-65, October, 1995.
- [3] Virgil Bocean, Survey and Alignment Group, internal memo dated Nov. 3, 1994.
- [4] The Fermilab Main Injector Technical Design Handbook, Chapter 2, August 1994.
- [5] John Johnstone, private communication.
- [6] The simulation program was written by individuals in the Main Injector group. The analytical and numerical treatments of extraction from MI52 are described in two MI notes by J. A. Johnstone: “A Simplified Analysis of Resonant Extraction at the Main Injector”, MI Note 091, September, 1993; “A Numerical Simulation of Resonant Extraction”, MI Note 095, October, 1993.
- [7] H. Grote and F. C. Iselin, “The Methodical Accelerator Design (MAD) Program”, CERN/SL/90-13(AP) , Rev.4.
- [8] Cliff Lee, private communication.
- [9] A. Van Ginnekin, “CASIM - Program to Simulate Transport of Hadronic Cascades in Bulk Matter”, Internal Fermilab Report FN-272, 1975.
- [10] I. Azhgirey *et al.*, Proceedings of the XV Conference on Charged Particle Accelerators, p. 74, Protvino, Russia, 1996.
- [11] A. Abramov *et al.*, “Conceptual Design Work and Neutrino Beam Calculations for the NuMI Project”, Protvino, 1997.

- [12] A.E. Brenner *et al.*, Phys. Rev. D26 (1982) 1497.
- [13] A.J. Malensek, “Neutrino Beams Using the Main Injector”, FERMILAB-TM-1951, November 1995.
- [14] WBB Postion Paper, NuMI-B-154, January 31, 1996.
- [15] PBEAM by Noel Stanton, see “P-875: A Long-baseline Neutrino Oscillation Experiment at Fermilab”, (1995) for a description.
- [16] W. M. Smart, “NuMI Wide Band Neutrino Beam Alignment Requirements, Calculated using a Modified Version of the PBEAM Monte Carlo Program”, NuMI Note L-221 (1996).
- [17] A.J. Malensek, “Empirical Formula for Thick Target Particle Production”, Fermilab FN-341, October 12, 1981.
- [18] C.L. Wang, Phys. Rev. **D10**, 3876 (1974).
- [19] G. Cocconi *et al.*, LBL Report No. UCRL 10022, (1961).
- [20] H.W. Atherton *et al.*, CERN 80:07, (1980).
- [21] R. H. Milburn, “Theory of the Hylen Hadronic Hose”, NuMI-B-271, May 28, 1997.
- [22] Zhijing Tang, “Structural Analysis of NUMI Horn”, May 14, 1997.
- [23] R. Bernstein, *et al.*, “Conceptual Design Report: Main Injector Neutrino Program”, FNAL, (1991); “Project Definition Report: NuMI Project”, FNAL F.E.S.S., (1993); “Project Definition Report: NuMI Project (LBL MI-60)”, FNAL F.E.S.S., (1994).
- [24] A. Visser, “Preliminary Design Note for a Direct Coupled 200,000 Amp Neutrino Horn Power Supply with Energy Recovery”, Fermilab TM-1924 (1994).
- [25] R. H. Milburn, “The Geomagnetic Distortion of the NuMI Neutrino Beam”, NuMI-B-226, November 1996.
- [26] S. Menary, “A GNuMI Study of the Effect of the Geomagnetic Distortion of the NuMI Neutrino Beam”, forthcoming NuMI note.
- [27] E.H.M. Heijne, “Muon Flux Measurement with Silicon Detectors in the CERN Neutrino Beams”, CERN 83-06, July 1983 (doctoral thesis - University of Amsterdam).

- [28] G. Cavallari *et al.*, “Solid State Detectors Used for the CERN Neutrino Flux Monitoring (NFM)“, IEEE Trans. Nucl. Sci, NS-25, p. 600, Feb. 1978; G. Acquistapace *et al.*, “The West Area Neutrino Facility for CHORUS and NOMAD experiments (94 - 97 operation)”, CERN-ECP/95-14, 31 July 95; L. Casagrande *et al.*, “The Alignment of the CERN West Area Neutrino Facility“, CERN 96-06, 9 August 1996.
- [29] A. Wehmann, “Study of Muons Downstream of Hadron Absorber”, forthcoming NuMI note.
- [30] In a private communication dated 4/8/97, V. Falaleev from CERN said that in their current setup they have a few solid state detectors with a RMS distribution $\leq 1\%$, for a response normalized to a beam current transformer over a year’s time. The average for all detectors is $\sim 2\%$. If they use the stable detectors as a reference for relative calibration of the others, the average RMS is about 1.2 – 1.5%.
- [31] Private communication with Jean-Marie Maugain of CERN, April, 1997.
- [32] D. Crane *et al.*, “The Length of the NuMI shield”, NuMI-B-121, November 1995.
- [33] D. Crane *et al.*, “Position Paper on the Length of the NuMI shield”, NuMI-B-132, December 1995.
- [34] A. Wehmann, W. Smart, S. Menary, J. Hylen, and S. Childress, “Groundwater Protection for the NuMI Project”, FERMILAB-TM-2009, NuMI-B-279, August 1997.
- [35] D. Cossairt, “Environmental Protection Note 8”, Fermilab, Dec. 1, 1994.
- [36] J. Malensek, A.A. Wehmann, A.J. Elwyn, K.J. Moss, and P.M. Kesich, “Groundwater Migration of Radionuclides at Fermilab”, Fermilab Report TM-1851, August 1993
- [37] STS Consultants, Ltd., “Hydrogeological Evaluation Report Neutrino Main Injector (NuMI) 12050-DL, April 1997
- [38] Harza Engineering Company, draft letter review of (ST97), May 8, 1997